Title

Modeling Water Management in Polymer-Electrolyte Fuel Cells

Permalink

https://escholarship.org/uc/item/9b90b5vn

Authors

Weber, Adam
Department of Chemical Engineering, University of California, Berkeley

Publication Date

2008-06-10

Modeling Water Management in Polymer-Electrolyte Fuel Cells

Adam Z. Weber*[,1], Ryan Balliet[2], Haluna P. Gunterman[2], John Newman[1,2]

[1]Environmental Energy Technologies Division,
Lawrence Berkeley National Laboratory
and
[2]Department of Chemical Engineering,
University of California, Berkeley, California 94720-1462, USA

*Corresponding author: azweber@lbl.gov; phone: 510-486-6308

Contents

1 Introduction

Fuel cells may become the energy-delivery devices of the 21st century with realization of a carbon-neutral energy economy. Although there are many types of fuel cells, polymer-electrolyte fuel cells (PEFCs) are receiving the most attention for automotive and small stationary applications. In a PEFC, hydrogen and oxygen are combined electrochemically to produce water, electricity, and waste heat.

During the operation of a PEFC, many interrelated and complex phenomena occur. These processes include mass and heat transfer, electrochemical reactions, and ionic and electronic transport. Most of these processes occur in the through-plane direction in what we term the PEFC sandwich as shown in Figure 1. This sandwich comprises multiple layers including diffusion media that can be composite structures containing a macroporous gas-diffusion layer (GDL) and microporous layer (MPL), catalyst layers (CLs), flow fields or bipolar plates, and a membrane. During operation fuel is fed into the anode flow field, moves through the diffusion medium, and reacts electrochemically at the anode CL to form hydrogen ions and electrons. The oxidant, usually oxygen in air, is fed into the cathode flow field, moves through the diffusion medium, and is electrochemically reduced at the cathode CL by combination with the generated protons and electrons. The water, either liquid or vapor, produced by the reduction of oxygen at the cathode exits the PEFC through either the cathode or anode flow field. The electrons generated at the anode pass through an external circuit and may be used to perform work before they are consumed at the cathode.

The performance of a PEFC is most often reported in the form of a polarization curve, as shown in Figure 2. Roughly speaking, the polarization curve can be broken down into various regions. First, it should be noted that the equilibrium potential differs from the open-circuit voltage due mainly to hydrogen crossover through the membrane (*i.e.*, a mixed potential on the cathode) and the resulting effects of the kinetic reactions. Next, at low currents, the behavior of a PEFC is dominated by kinetic losses. These losses mainly stem from the high overpotential of the oxygen-reduction reaction (ORR). As the current is increased, ohmic losses become a factor in lowering the overall cell potential. These ohmic losses are mainly from ionic losses in the electrodes and separator. At high currents, mass-transport limitations become increasingly important. These losses are due to reactants not being able to reach the electrocatalytic sites.

Key among the issues facing PEFCs today is water management. Due to their low operating temperature (< 100°C), water exists in both liquid and vapor phases. Furthermore, state-of-the-art membranes require the use of water to provide high conductivity and fast proton transport. Thus, there is a tradeoff between having enough water for proton conduction (ohmic losses), but not too much or else the buildup of liquid water will cause a situation in which the reactant-gas-transport pathways are flooded (mass-transfer limitations). Figure 3 displays experimental evidence of the effects of water management on performance. In Figure 3(a), a neutron image of water content displays flooding near the outlet of the cell due to accumulation of liquid water and a decrease in the gas flowrates. The serpentine flow field is clearly visible with the water mainly underneath the ribs. Figure 3(b) shows polarization performance at 0.4 and 0.8 V and high-frequency resistance at 0.8 V as a function of cathode humidification temperature.[1] At low current densities, as the inlet air becomes more humid, the membrane resistance decreases, and the performance increases. At higher current densities, the same effect occurs; however, the higher temperatures and more humid air also results in a lower inlet oxygen partial pressure.

This later effect is also one of water management and is why the performance shows a maximum as a function of humidifier temperature.

Due to the complex and coupled nature of the underlying physical phenomena and the lack of definitive experimental evidence, fundamental modeling provides one of the only avenues to understand PEFCs fully and thoroughly. Modeling allows one to parse and explain the different regions in the polarization curve, elucidate optimal designs and operating conditions, and explore the governing physics and water-management aspects. A good PEFC model should have a physical basis, be predictive and agree with experimental data and trends, have a minimum of fitting parameters, and adequately model the dominant transport phenomena. Macroscopic modeling of PEFCs has been recently reviewed.[2-9] The most noteworthy of those reviews are those by Weber and Newman[2] and Wang,[3] who examined models of transport phenomena up to the end of 2003. This chapter serves to update (through June, 2007) and append those reviews by focusing on more recent modeling trends and developments with a theme of water management. This article is also a stand-alone entity that is perhaps more pedagogic than previous reviews, and seeks to explain the current state of understanding of water management and its modeling.

The focus of this chapter is on the macroscopic modeling of PEFC water management. The structure is based on water-management phenomena, with emphasis on what the models have taught and shown, and not an encyclopedic list of the recently published models. Section 2 contains the major modeling approaches and governing equations and is the basis for the majority of models. Section 3 deals with GDL-related simulation studies including more microscopic investigations. Section 4 is on design strategies for water management and focuses primarily on flow-field designs and their interaction with the PEFC sandwich. Section 5 examines transient analysis, especially that during load changes. Section 6 and 7 detail some special applications and models regarding subzero operation and freeze phenomena and higher-temperature phenomena, respectively. Before proceeding to the governing equations, it is worthwhile to discuss what experiments tell about water management.

1.1 *In-situ* Visualization of Water

Water management has been a ripe opportunity for study through mathematical modeling because of its complex nature in PEFCs, as well as the fact that there is only limited direct experimental validation of it. While one can easily obtain a polarization curve or even a segmented-cell current density, relating these more global results to specific phenomena requires mathematical models. The corollary of course is that validation of the models can be done only through these averaged or tangential results; thus, various models can fit the data with the same accuracy, but come up with different limiting factors depending on how the model is biased. Luckily, the realm of experimental imaging is starting to allow for direct comparisons of predicted water contents and water management in an operating PEFC.

The field of view captured by imaging techniques spans areas ranging from that of a full- or subscale-size cell—via magnetic resonance imaging (MRI), nuclear magnetic resonance (NMR), or neutron radiography—to the midrange scale that can be thought of as focusing more on a single channel—via study of transparent cells or fluorescent microscopy—down to the micrometer scale—via X-ray tomography. Although the visualization methods with regards to

PEFC imaging are still in the development phase, their strengths and weaknesses may be leveraged to create a more complete picture of relevant and limiting processes.

MRI, NMR, and neutron-imaging techniques are often employed to image test cells and have resolutions between 10 and 100 μm. MRI and NMR both exploit the signal generated by disturbing a magnetic field with an electromagnetic force; the main difference between the two methods being that MRI also tracks the geometric source of resonance. Because the two methods utilize similar phenomena, they both exhibit a strong resolution-to-run-time tradeoff. As a point of reference, a minute long scan can give roughly 50 μm in resolution.[10] These resonance techniques are nonoptimal for imaging conductive material, such as the GDL and CL, because the signal from most paramagnetic materials decays too quickly for analysis. Alternatively, this quick decay means that the water content of the membrane may be studied in near isolation. Several groups have used resonance techniques to study the water distribution in the membrane of operating fuel cells.[11-13] Findings include confirmation of the link between proper membrane hydration and performance and validation of the model predictions of using counterflow, rather than coflow, to promote a more uniform liquid-water distribution in the cell.[11] The main strength of resonance imaging is its accessibility and state of development as a field in which the physics is well understood. It is a convenient imaging technique for studying water content in nonconductive media provided that the information sought does not require speed nor layer-by-layer resolution. Furthermore, unlike some of the other imaging techniques, it can simultaneously provide both chemical and geometric information.

Neutron-imaging experiments (see Figure 3(a)) also treat large areas of a PEFC at a time, more so than MRI and NMR.[14] They also are gaining popularity because of neutron imaging's short temporal resolution, on the order of seconds.[15] Neutron imaging is similar to X-ray imaging, but instead of bombarding a sample with X-rays, a neutron source is utilized. Image masking may be used in conjunction with neutron radiography results to differentiate the PEFC components into CL and membrane, GDLs, and flow fields. Image masking involves keeping only image data from a specific depth and for a PEFC system has a resolution of 100 μm, although that should be decreasing with more advanced detectors.[16] Transient results indicate the importance of incorporating temperature effects in order to understand how the water distribution reaches steady state. For example, Hickner *et al.*[15] found that the cell achieved steady state about 100 to 200 seconds after the current load underwent a step increase from 0 to 1000 mA for their particular set-up. They also confirmed the competition between water production and heat generation, where increasing current density generates water, but eventually the water content declines as local heating effects become important. Other neutron-radiography studies treat the effect of changing pressure on systems operating under varying humidification conditions, and provide further checks on what constitute physically accurate modeling results.[17,18] Neutron imaging is a highly powerful tool, especially for transient analysis of PEFC systems, but lack of neutron sources severely limits accessibility. A commonality between all three methods discussed thus far is their use in studying in-plane movement and distribution of water.

Midrange imaging techniques treat mm^2 sized areas and provide insight into and validation of through-plane flow patterns. Imaging results elucidate possible material-structure changes and also present ideas on the correct boundary condition at the GDL / gas-channel interface. Transparent-PEFC imaging entails the replacement of the bipolar plate with a transparent material and then direct observation of the system. This method is useful for seeing water-droplet formation at the GDL / gas-channel interface and movement down the channel (see Figure 19).[19-22] Water droplets have been seen to grow until they become large enough to be wicked to the side walls, along which water then moves (of course, the transparent material undoubtedly has thermal and wetting characteristics different from actual bipolar plates). Litster *et al.*[23] used another midrange imaging technique, fluorescent microscopy, to propose a fingering-and-channeling transport method from *ex-situ* imaging of GDLs. From their observations, they derived a movement mechanism where the water within the GDL is pulled by capillary action along paths that begin to merge into each other. Then, once a dominant pathway forms, water from nearby channels is siphoned into the dominant conduit, and a droplet forms at the GDL surface.

Determining with absolute certainty the dominant water-movement mechanism, requires finer resolution of the internal PEFC environment. Synchrotron X-ray radiography employs a particle accelerator to generate a high-energy electron beam, which is impacted with a target to form X-rays that are subsequently focused onto an object of interest. Resolution is on the order of 10 μm when applied to a PEFC system, although with more sophisticated treatments a better resolution is obtainable.[24] By taking a series of images from different angles and reconstructing them, synchrotron radiography can be used to generate a 3-D tomographic image of a GDL. The rendered image distinguishes the GDL structure—carbon and PTFE appear the same because of their similar electron density—from the water found within.[24] Initial results show that many pockets of water can remain in the GDL even after two minutes of purging.[24] Manke *et al.*[25] also show that there is a periodicity in which water droplets form, grow, and move away from the initial break-through point at the GDL / gas-channel interface. The temporal and spatial regularity of the cycle led to the suggestion that liquid water within the GDL is pulled by capillary action along paths that begin to merge into each other and form one larger water conduit to the surface of the GDL. A drawback of synchrotron tomography is that a full 3-D image can take up to thirty minutes or an hour depending on the number of pictures taken; therefore, this technique has limited usefulness for the study of transient phenomena like the initial liquid-water percolation with the GDL. Improvements in resolution and sensitivity may someday uncover the GDL microstructure (*e.g.*, pores of Teflon and carbon) in enough detail to provide the underlying structure for Lattice-Boltzmann or pore-network models.

2 Basic Phenomena, Methodology, and Governing Equations

To model water management inside a PEFC, one must be cognizant of the underlying physical phenomena which are occurring. These phenomena require knowledge not only of water transport but also of transport of the other species, governing thermodynamic and kinetic relations, *etc*. Furthermore, there are different global modeling methodologies for modeling PEFCs, and in particular, the PEFC sandwich or through-plane direction. The easiest division to make is between macroscopic and microscopic models. The microscopic models seek to model transport on an individual pore level, whereas the macroscopic ones are continuum and average over this level. Although the microscopic models may provide more realistic conditions and factors, they require a lot more knowledge of the microstructure and are much more expensive in terms of computation time. Macroscopic models are more common for PEFCs, although it is the current trend to try to incorporate more microscopic details into them.

Most of the current macroscopic models utilize a macrohomogeneous approach, wherein the exact geometric details of the modeling domain are neglected. Instead, the domain is treated as a randomly arranged porous structure that can be described by a small number of variables such as porosity and surface area per unit volume. Furthermore, transport properties within the domain are averaged over the volume of it. Thus, all variables are defined at all positions within the domain. Averaging is performed over a region that is small compared to the size of the domain, but large compared to its microstructure.

A model can be classified based on its geometric dimensionality as shown in Figure 4. Zero-dimensional (0-D) models are mainly empirical and model a PEFC with a simple equation; these are typically used to fit data and get a general idea of the relative magnitude of the various phenomena. 1-D models treat the PEFC sandwich in varying degrees of complexity, ranging from simple equations to complex expressions derived from physical models. Furthermore, they can incorporate other (nongeometric) dimensional effects in terms of size, *i.e.*, microscopic and macroscopic effects (*e.g.*, consumption of reactant in a pore of a particle which is within a porous electrode). 2-D models deal with effects in the PEFC which occur in the sandwich as well as in another direction, either across or along the gas channel. Finally, 3-D models include the 1-D sandwich and consider effects in both directions in the flow field.

Pseudo-dimensional models can also be used where one or more directions are treated rigorously and another direction is treated simplistically. A classic example is a pseudo 2-D or 1+1-D model where multiple 1-D sandwich models are run and tied together through their external boundary conditions to account for flow along the channel. Based on scale-separation arguments and the additional computational cost and complexity of running higher-dimensional models, we believe that a pseudo 3-D model (2-D sandwich with rib (land) and channel effects, and a separate along-the-channel model) provides the best compromise in terms of reality and complexity; however, 1-D models are very good starting points for investigating specific phenomena (*e.g.*, carbon corrosion during startup).

Although the number of PEFC models is large, the number of modeling groups and approaches is significantly smaller. The obvious reason is that as a group becomes more familiar with a model, they continually upgrade it in terms of complexity to make it more physically realistic. For an approach, if it is general, then the community adopts and alters it. Furthermore, the models can generally be categorized based on what they attempt to model. For example, there are those that account for two-phase flow and flooding versus those that focus instead on membrane dehydration and low-relative-humidity operation. With the advancement of computational efficiency and speed and the physical understanding of PEFC operation, models currently in use are multidimensional, account for most water-management aspects such as flooding and dehydration, and are nonisothermal. The use of transients models is also coming on-line as discussed later. While it is interesting to examine the historical route for the modeling of some phenomena and to examine each modeling group's contribution to the field, such a review is outside the purview of this article, and can be found in our review article of macroscopic PEFC transport modeling.[2]

In this section, the general governing equations are presented and discussed. The discussion is loosely arranged by the various PEFC layers as shown in Figure 1. This section is to serve as a primer for the following sections wherein more detailed analyses are made concerning the movement of water in GDLs, flow fields, and specific applications. Therefore, it is more of a how-to section than demonstrating modeling results. The treatment of the CLs and membrane are also contained within this section, as is a general discussion of two-phase flow in the GDLs, but first, the fundamental governing equations are presented.

2.1 Fundamental Governing Equations

A PEFC is governed by thermodynamics, kinetics, and transport phenomena as described by conservation equations. In this subsection, the relevant equations are presented. These basic equations form the basis of all macroscopic PEFC models. The differences, as discussed in this chapter, are due to how one defines fluxes (*i.e.*, transport equations) and the relevant source and sink terms.

2.1.1 Thermodynamics

As shown in Figure 2, the theoretical potential represents the highest voltage obtainable for a single cell as derived from thermodynamics. The overall fuel-cell reaction can be broken down into the two overall electrode reactions. If hydrogen is the primary fuel, it oxidizes at the anode according to the reaction

$$\mathrm{H_2 \rightarrow 2H^+ + 2e^-} \tag{1}$$

At the cathode, oxygen is reduced

$$\mathrm{4H^+ + 4e^- + O_2 \rightarrow 2H_2O} \tag{2}$$

Adding equations 1 and 2 yields the overall reaction

$$\mathrm{2H_2 + O_2 \rightarrow 2H_2O} \tag{3}$$

The potential of the overall cell is given by a Nernst equation[26,27]

$$U = U^{\theta} + \frac{RT}{2F} \ln\left(\frac{p_{\mathrm{H}_2} \sqrt{p_{\mathrm{O}_2}}}{p_w} \right) \tag{4}$$

where subscript w stands for water, R is the ideal-gas constant, T is the absolute temperature, F is Faraday's constant, and U^{θ} is the standard cell potential, a combination of appropriately chosen reference states that is a function of temperature and can be unit dependent. U^{θ} can be related to the Gibbs free energy of the reaction

$$\Delta G = -2FU^{\theta} \tag{5}$$

Similarly, an enthalpy potential can be defined as

$$U_H = \frac{\Delta H}{2F} = U^{\theta} - T \frac{\partial U^{\theta}}{\partial T} \tag{6}$$

This potential is also known as the thermoneutral potential, or the potential at which there is no net heat generation.

Using the first law of thermodynamics yields an expression for the heat generation of the PEFC[28,29]

$$Q = i\left(U_H - V\right) \tag{7}$$

where Q is the total heat generated per superficial area, i is the superficial current density, and V is the (observed) cell potential. The above heat generation can also be broken down into reversible and irreversible parts, which are given by

$$Q_{\mathrm{rev}} = i\left(U_H - U^{\theta}\right) \tag{8}$$

and

$$Q_{\mathrm{irrev}} = i\left(U^{\theta} - V\right) \tag{9}$$

respectively. It is worth mentioning that the PEFC community typically defines efficiency using the deviation of the operating potential from the Gibbs free energy or reversible potential. This definition does not account for the intrinsic reversible losses. The correct definition should be from the enthalpy and not the reversible potential; such a definition allows for a fair comparison of PEFCs with other energy-conversion devices using the higher heating value of the fuel.

2.1.2 Kinetics

The initial drop in the polarization curve (Figure 2) is due to the sluggish kinetics of the ORR at the temperatures normally used for current PEFC operation (< 100°C). A typical electrochemical reaction can be expressed as

$$\sum_{k}\sum_{i} s_{i,k,h} M_i^{z_i} \rightarrow n_h \mathrm{e}^- \tag{10}$$

where $s_{i,k,h}$ is the stoichiometric coefficient of species i residing in phase k and participating in electron-transfer reaction h, n_h is the number of electrons transferred in reaction h, and $M_i^{z_i}$ represents the chemical formula of i having valence z_i.

The rate of an electrochemical reaction depends upon the concentrations of the various species and the potential drop across the reaction interface between phases k and p, which are normally the electrode and electrolyte, respectively. In general, a Butler-Volmer expression can be used to describe the kinetics

$$i_h = i_{0_h}\left[\exp\left(\frac{\alpha_a F}{RT}\left(\Phi_k - \Phi_p - U_h^{\mathrm{ref}}\right)\right)\prod_i^{a}\left(\frac{p_i}{p_i^{\mathrm{ref}}}\right)^{s_{i,k,h}} - \exp\left(\frac{-\alpha_c F}{RT}\left(\Phi_k - \Phi_p - U_h^{\mathrm{ref}}\right)\right)\prod_i^{c}\left(\frac{p_i}{p_i^{\mathrm{ref}}}\right)^{-s_{i,k,h}}\right] \tag{11}$$

where i_h is the transfer current between phases k and p due to electron-transfer reaction h, the products are over the anodic and cathodic reaction species, respectively, α_a and α_c are the anodic and cathodic transfer coefficients, respectively, p_i and p_i^{ref} are the partial pressure and reference partial pressure for species i, respectively, and i_{0_h} and U_h^{ref} are the exchange current density per unit catalyst area and the potential of reaction h evaluated at the reference conditions and the operating temperature, respectively. In the above expression, the composition-dependent part of the exchange current density is explicitly written, with the multiplication over those species in participating in the anodic or cathodic direction. The reference potential can be determined using a Nernst equation (*e.g.*, see equation 4); if the reference conditions are the same as the standard conditions (*i.e.*, 100 kPa pressure for the different gas species), then U^{ref} has the same numerical value as U^{θ}.

The term in parentheses in equation 11 can be written in terms as an electrode overpotential

$$\eta_h = \Phi_k - \Phi_p - U_h^{\text{ref}} \tag{12}$$

In this chapter, the reference electrode used is defined as a platinum metal electrode exposed to hydrogen at the same temperature and electrolyte (*e.g.*, Nafion®) as the solution of interest. With this reference electrode, the electrode overpotential defined in equation 12 is the same as having the reference electrode located next to the reaction site but exposed to the reference conditions (*i.e.*, it carries its own extraneous phases with it). Typical values for the reference conditions are those in the gas channels. If the reference electrode is exposed to the conditions at the reaction site, then a surface or kinetic overpotential can be defined

$$\eta_{s_h} = \Phi_k - \Phi_p - U_h \tag{13}$$

where U_h is the reversible potential of reaction *h*. The surface overpotential is the overpotential that directly influences the reaction rate across the interface. Comparing equations 13 and 12, one can see that the electrode overpotential contains both a concentration and a surface overpotential for the reaction; the reader is referred to Neyerlin *et al.*[30] for a very good discussion of the different overpotentials and related kinetic expressions for the ORR.

For the hydrogen-oxidation reaction (HOR) at the anode, equation 11 becomes, in the absence of poisons,

$$i_{\mathrm{HOR}} = i_{0_{\mathrm{HOR}}}\left[\frac{p_{\mathrm{H_2}}}{p_{\mathrm{H_2}}^{\mathrm{ref}}}\exp\left(\frac{\alpha_a F}{RT}\left(\eta_{\mathrm{HOR}}\right)\right)-\exp\left(\frac{-\alpha_c F}{RT}\left(\eta_{\mathrm{HOR}}\right)\right)\right] \tag{14}$$

where 1 and 2 denote the electron- and proton-conducting phases, respectively. Because the electrolyte is a polymer of defined acid concentration, the proton concentration does not enter directly into equation 14. However, if one deals with contaminant ions, then the activity of protons should explicitly enter into equation 14 either through the equilibrium potential or the kinetic equation, depending on the reference state used. Also, it has recently been shown that the HOR may proceed with a different mechanism at low hydrogen concentrations; in this case, the kinetic equation is altered through the use of a surface adsorption term.[31] Due to the choice of reference electrode, the reference potential and reversible potential are both equal to zero.

Unlike the facile HOR, the oxygen-reduction reaction (ORR) is slow and represents the principal inefficiency in many fuel cells. Due to its sluggishness, the ORR is modeled reasonably well with Tafel kinetics with a dependence on oxygen partial pressure, m_0, of between 0.8 and 1[30,32-34]

$$i_{\mathrm{ORR}} = -i_{0_{\mathrm{ORR}}} \left(\frac{p_{\mathrm{O_2}}}{p_{\mathrm{O_2}}^{\mathrm{ref}}} \right)^{m_0} \exp\left(\frac{-\alpha_c F}{RT} (\eta_{\mathrm{ORR}}) \right) \tag{15}$$

For the kinetic region, the values of the theoretical and experimental Tafel slopes have been shown to agree with α_c equal to 1.[30,32,34-41] As with the case of the HOR, the dependence of the reaction rate on the hydrogen ion activity is not shown explicitly. While this is typically reasonable, as discussed in section 7.2, under low humidity conditions, the change in the proton concentration and especially its activity coefficient necessitate accounted explicitly for the proton activity.[42]

While the ORR and HOR are the principal reactions occurring in PEFCs, it is worth noting the possibility of side reactions that can occur in the CLs. These stem from durability and degradation analyses and, although mentioned below, are not covered in this chapter on water management. One of these other reactions include the two-electron reduction of oxygen crossing over to the anode to hydrogen peroxide.[43] In addition, hydrogen peroxide also forms at the cathode as part of the ORR.[44] Also, hydrogen in the membrane that is crossing over can reduce platinum ions to metal, forming a platinum band in the membrane.[45] Platinum itself undergoes oxide formation and stripping, which includes possible dissolution and movement as ions.[46,47] Finally, oxygen evolution (the anodic term to the ORR equation) and carbon oxidation at the cathode can also occur due to fuel starvation at the anode.[48,49]

2.1.3 Conservation equations

The conservation equations stem from the underlying fundamental physics. There are three principal equation types that are of interest: mass, energy, charge. These are presented in turn below.

For conservation of mass, it is necessary to write a material balance for each independent component in each phase. For PEFCs, the differential form of the material balance for species *i* in phase *k* is[2]

$$\frac{\partial \varepsilon_k c_{i,k}}{\partial t} = -\nabla \cdot \mathbf{N}_{i,k} - \sum_h a_{1,k} s_{i,k,h} \frac{i_{h,1-k}}{n_h F} + \sum_l s_{i,k,l} \sum_{p \neq k} a_{k,p} r_{l,k-p} \tag{16}$$

The term on the left side of the equation is the accumulation term, which accounts for the change in the total amount of species *i* held in phase *k* within a differential control volume. The first term on the right side of the equation keeps track of the material that enters or leaves the control volume by mass transport. The remaining two terms account for material that is gained or lost due to chemical reactions. The first summation includes all interfacial electron-transfer reactions, the second summation accounts for non-electrochemical interfacial reactions (*e.g.*, evaporation/condensation.

In the above expression, $c_{i,k}$ is the concentration of species *i* in phase *k*, and $s_{i,k,l}$ is the stoichiometric coefficient of species *i* in phase *k* participating in heterogeneous reaction *l* (see eq 10). a_h is the specific surface area (surface area per unit total volume) of the interface for the electrochemical reactions. In the above expression, Faraday's law

$$N_{i,k} = \sum_h s_{i,k,h} \frac{i_h}{n_h F} \tag{17}$$

was used to change the interfacial current density into an interfacial flux quantity. $r_{l,k-p}$ is the rate of the heterogeneous reaction *l* per unit of interfacial area between phases *k* and *p.*

For the conservation of charge, the equation is similar to the mass balance above. Because a large electrical force is required to separate charge over an appreciable distance, a volume element in the electrode will, to a good approximation, be electrically neutral; thus one can assume electroneutrality for each phase

$$\sum_i z_i c_{i,k} = 0 \tag{18}$$

where z_i is the charge number of species *i*. The assumption of electroneutrality implies that the diffuse double layer, where there is significant charge separation, is small compared to the volume of the domain, which is normally the case. The general charge balance, assuming electroneutrality becomes

$$\frac{\partial \rho_{\mathrm{e}}}{\partial t} = \sum_k \nabla \cdot \mathbf{i}_k \tag{19}$$

where ρ_{e} is the charge density that can be substituted with the double-layer capacity and the potential as is done for transient or impedance analyses. For steady-state cases, there is no accumulation of charge, and the conservation of charge becomes the divergence of the total current density is zero.

For conservation of energy, if one desires to account only for the total heat generation, equation 7 can be used. However, if the specific heat-generation locations and the thermal gradients are desired, a conservation equation can be used. For PEFCs, the governing thermal-energy conservation equation becomes[2,26,50]

$$\sum_k \rho_k \hat{C}_{p_k} \frac{\partial T}{\partial t} = -\sum_k \rho_k \hat{C}_{p_k} \mathbf{v}_k \cdot \nabla T + \nabla \cdot \left(k_T^{\text{eff}} \nabla T\right) + \sum_k \frac{\mathbf{i}_k \cdot \mathbf{i}_k}{\kappa_k^{\text{eff}}} + \sum_h i_h \left(\eta_h + \Pi_h\right) - \Delta H_{\text{evap}} r_{\text{evap}} \quad (20)$$

where it has been assumed that the temperatures in the various phases (*i.e*, membrane, gas, liquid, and solid) are in equilibrium with each other. If such an assumption is undesirable, which could be the case, then similar energy equations can be used for each phase (for example, see Hwang *et al.*[51]). The first term on the left side of equation 20 is the accumulation of energy, where $\hat{C}_{p_k}$ and ρ_k are the (average) heat capacity and density of phase *k*, respectively. The first term of the right side represent convection of energy, where $\mathbf{v}_k$ is the mass-averaged velocity of phase *k*, respectively. The second term on the left side represents heat transfer due to conduction, where k_T^{eff} is the effective thermal conductivity of the system. The third term is due to ohmic heating where κ_k^{eff} is the effective electronic or ionic conductivity of phase *k*. The fourth term is the heat generation due to the electrochemical reactions, where the irreversible generation is given by the overpotential, η, and the reversible part is given by the Peltier coefficient, Π.[52] The last term is due to evaporation/condensation of water, where ΔH_{evap} is the heat of vaporization and r_{evap} is the rate of evaporation. Finally, unlike the other conservation equations, that of energy expands the energy flux explicitly into its convective and conductive parts.

2.2 Membrane Modeling

One of the most important parts of the PEFC is the electrolyte or membrane, especially in terms on water management since drier feeds cause the membrane to lose water and thus become more resistive and ohmically limit the cell performance. The PEFC membrane is a proton conductor where the anions (typically sulfonic acid moieties) are tethered to the polymer backbone. There are numerous studies of the various membranes' properties, structure, *etc*., many of which are contradictory. A main problem is that the current state-of-the-art membranes are random copolymers and are thin, thereby making characterization difficult. Furthermore, pretreatment of the membrane can have a profound effect on its morphology and hence its properties. In fact, depending on how one pretreats the membrane, there can be large differences in the water uptake or water content (known as λ, moles of water per mole of sulfonic acid site) depending on the reservoir phase in contact with the membrane.[53] This discrepancy, known as Schröder's paradox, can be as large as a difference between $\lambda = 14$ for a vapor-equilibrated membrane and $\lambda = 22$ for a liquid-equilibrated one. With the corresponding differences in water content, the membrane microstructure and hence its transport parameters and maybe even transport phenomena may change.[54] For more detailed discussions please see the relevant literature including very good reviews on Nafion® (the current polymer of choice)[55] and alternative hydrocarbon membranes.[56]

Due to its importance and complexity, the membrane's behavior has been simulated with a whole range of models, from the atomistic and molecular through to the macroscopic. The microscopic models try to predict the membrane microstructure and phase separation due to water uptake, as well as examine transport through it at a fundamental level. The macroscopic models are often more empirical and focus on describing the transport and relevant parameters of the membrane in a macrohomogeneous fashion. As per the overall approach of this chapter, discussion is made on the macroscopic models; for microscopic analyses, see the review in this volume as well as that of Kreuer *et al.*[57] The discussion below is focused mainly on the governing transport equations using a concentrated-solution-theory approach, and developments in the last few years. For more detailed historical and other modeling approaches, the reader is referred to recent reviews on this subject.[2,58,59]

2.2.1 Concentrated solution theory

Concentrated solution theory takes into account all binary interactions between all of the species, and it uses a more general driving force, namely, that of chemical potential. In this fashion, it is similar to the Stefan-Maxwell multicomponent diffusion equations (see equation 30). In fact, there is a direct analog of those equations and the dusty-gas model that is used for PEFC membrane modeling, which is termed the binary friction model[59,60]

$$\nabla \mu_i = \nabla\left(RT \ln x_i - z_i F \Phi\right) = \sum_{j \neq i} \frac{RT x_j}{D_{i,j}^{\text{eff}}}\left(\frac{\mathbf{N}_j}{c_j} - \frac{\mathbf{N}_i}{c_i}\right) - \frac{RT}{D_{i,\text{m}}^{\text{eff}}}\left(\frac{\mathbf{N}_i}{c_i}\right) \tag{21}$$

where the m denotes the interaction with the membrane and eff denotes an effective property of the membrane. As discussed by Fimrite *et al.* [59,61] and Carnes and Djilali,[60] this treatment is similar to that of the dusty fluid model applied to the membrane,[62,63] but accounts for the bulk movement of water in a more consistent manner using a different reference frame. The binary friction model assumes that hydronium ions and water act as separate species within the membrane microstructure. Furthermore, the electrochemical potential is used instead of the chemical potential as a driving force. The mole fractions and diffusion coefficients in the above equation can be related to the water content of the membrane.[60,64]

A very similar treatment to that above can be reached by starting with the original equation of multicomponent transport[65]

$$\mathbf{d}_i = c_i \nabla \mu_i = \sum_{j \neq i} K_{i,j} \left(\mathbf{v}_j - \mathbf{v}_i \right) \tag{22}$$

where $\mathbf{d}_i$ is the driving force per unit volume acting on species i and can be replaced by a chemical potential gradient of species i, and $K_{i,j}$ are the frictional interaction parameters between species i and j. Instead of introducing the concentration scale, one can invert the above set of equations and relate the inverted $K_{i,j}$'s to experimentally measured transport properties using a set of three orthogonal experiments.[65,66] Doing this results in the proton and water governing transport equations,

$$\mathbf{i}_2 = -\frac{\kappa \xi}{F} \nabla \mu_\mathrm{w} - \kappa \nabla \Phi_2 \tag{23}$$

and

$$\mathbf{N}_\mathrm{w} = \xi \frac{\mathbf{i}_2}{F} - \alpha_\mathrm{w} \nabla \mu_\mathrm{w} \tag{24}$$

respectively, where α_w is the transport coefficient of water[64,66] and ξ is the electroosmotic (drag) coefficient.[67] The chemical-potential driving force can either be used as is or substituted by a mole-fraction or water-content expression, depending on how one wants to express the transport properties. The concentrated-solution-approach governing equations remain valid for all water contents assuming that the correct interaction parameters are known as a function of water content, and there is a methodology to calculate the water content as mentioned below.

It is worth mentioning some special simplifications that have been and continue to be used for membrane modeling. All of these other approaches use Ohm's law for proton movement,

$$\mathbf{i}_2 = -\kappa\nabla\Phi_2 \tag{25}$$

where κ is the ionic conductivity of the membrane. Thus, they do not account for the streaming current term in equation 23. For water movement, these other approaches differ as follows. The first is for membranes at lower water contents where one can use a dilute-solution analog to the above equations (*i.e.*, the Nernst-Planck equation)[26]. This approach results in equation 24 for water where a concentration driving force is used for the chemical-potential one. For liquid-equilibrated membranes, a more empirical approach is to use Schlögl's equation for water movement[68,69]

$$\mathbf{v}_{\mathrm{w}} = -\left(\frac{k}{\mu}\right)\nabla p_{\mathrm{L}} - \left(\frac{k_{\Phi}}{\mu}\right) z_f c_f F \nabla\Phi \tag{26}$$

where k and k_{Φ} are the effective hydraulic and electrokinetic permeability, respectively, p_{L} is the hydraulic or liquid pressure, μ is the water viscosity, and z_f and c_f refer to the charge and concentration of fixed ionic sites, respectively. Finally, a straightforward, albeit not rigorous, approach is to combine linearly the expected driving forces for water movement

$$\mathbf{N}_{\mathrm{w}} = \xi\frac{\mathbf{i}}{F} - D_{\mathrm{w}}\nabla c_{\mathrm{w}} - c_{\mathrm{w}}\frac{k}{\mu}\nabla p_k \tag{27}$$

where p_k can be the gas- or liquid-phase pressure. While this equation can describe water movement, it is on a tenuous basis in terms of the underlying physics and the separability of the driving forces.

2.2.2 Water content and properties

Essentially, all of the models center around the same or very similar governing equations as those described above. The difference is in how one relates the various gradients and model parameters to the water content of the membrane. The chemical-potential driving force has been used directly, changed into λ or the concentration or mole fraction of water, or separated into pressure and concentration terms; different approaches that are all not equivalent, as discussed in the previous subsection.

The simplest analysis for water content is to fix the anode and cathode boundary values of the water content using a water-uptake isotherm (*i.e.*, λ versus water activity in contact with the membrane), and assume a linear gradient between the values. While this is insufficient in many circumstances, it does allow for analytic solutions to be generated (see, for examples, Okada and cowrokers,[70,71] Carnes and Djilali,[60] and St-Pierre[14]), which may be utilized in system and stack models.

More complicated analyses try and predict the water content using a submodel that describes the believed physics with a minimum number of fitting parameters. While there are various models for predicting the water-uptake isotherm,[58] the comments below focus on those models which encompass the entire experimentally observed water content range from dry to liquid-equilibrated. The most prominent types of these models are those of Eikerling *et al.*,[72,73] Weber and Newman,[64] and Choi and Datta,[74,75] which have been modified by various authors. All of these models try to account for the water uptake and water content using macroscopic approaches based on flow-through-porous-media theory, where there are defined water pathways through the membrane. In terms of driving forces, Eikerling *et al.* uses both a concentration and a pressure, although the focus is more on the convective, pressure-related movement, Weber and Newman use the chemical potential directly, and Choi and Datta use essentially the binary friction model (equation 21).

Both Eikerling *et al.* and Weber and Newman assume that there are pores within the membrane that are either liquid-equilibrated or vapor-equilibrated. Eikerling *et al.* assumes a random network of pores that are either filled with bulk-like water or bound water, and impregnation by liquid water is easier than condensation. They use effective-medium theory to predict conductivity results from impedance data. Their model is more of a microscopic one in which λ is calculated by changing the number of pores that are filled and examining the types of liquid-film bonds between pores. Weber and Newman also assume a pore-size distribution, but use an "interaction" coefficient to relate whether the pore is liquid-equilibrated or vapor-equilibrated. The "interaction" coefficient is said to be physically related to the microstructure and surface and elastic energies within the polymer, although it is a fitting parameter in practice. Furthermore, Weber and Newman assume equilibrium between protons and water within the membrane to predict λ for the vapor-equilibrated part of the membrane.

Unlike the two models above, Choi and Datta is more of an interface model. While it is also more rigorous physically than the above ones, it is not clear how one can predict the water content changes within the membrane and how well the model can be used in a full-cell simulation. For example, it is unclear how important the interfaces are since in a full cell the CLs contain membrane tendrils and those will provide the protons into the membrane. The Choi and Datta model calculates the extra energy stored in the vapor-liquid interface at the membrane surface, resulting in a lower water content for a vapor-equilibrated membrane than a liquid-equilibrated one. They also utilize a chemical-equilibrium model to predict proton concentrations and water uptake in the vapor-equilibrated state.

Basically, all of the above models are using a construct of capillary condensation and phenomena to predict water contents. While this is not truly the physical representation of the membrane, it does serve as a way of organizing and visualizing the experimental data. It may be that such approaches are limited in their ability to predict water content since they average over the microstructure, which is key in determining the water content. However, more sophisticated molecular-dynamic-type models, which predict the water content and microphase separation of these membranes better, cannot be used in a full-cell simulations. The current belief seems to be that the mechanical properties and microstructure of the membrane are the important relations that must be considered to come up with an accurate membrane model; the challenge is to find a way to do this in a macroscopic fashion.

As a related aside, it is worth examining the impact of membrane constraint on water content. Inside of an operating PEFC, the membrane is constrained due to the clamping pressure applied on the stack. The impact of this constraint is mainly unknown, especially on the transport properties since none of them have been really measured under constraint conditions. Furthermore, constraint can lead to membrane thinning and perhaps physiochemical degradation. There have been two macroscopic models that examine this issue in terms of water content and PEFC performance. The first, by Weber and Newman,[76] shows that the water content will decrease due to the constraint, although a stress balance shows that the membrane does not feel much constraint since its swelling pressure will compress the GDLs. A more detailed and rigorous treatment of constraint, especially in terms of mechanical-property analysis was done recently by Nazarov and Promislow.[77] They also show that the membrane will be only slightly constrained, but this is enough to affect the water transport through it, as can be seen in Figure 5. In the figure, the net water flux through the membrane increases (more flow from anode to cathode) around 20 % due to the more uniform and lower water content in the membrane. The curves naturally increase with current density due to the larger impact of electroosmotic flow compared to the back diffusion. Both of the constraint studies show that water management can be affected by membrane constraint and there is a need to study this issue in more detail both theoretically and experimentally, especially in how it pertains to chemical-mechanical degradation and PEFC durability.

The overall guiding issue for the membrane models is to predict transport of the various species. Regardless of what set of governing equations is used, one must utilize the experimentally measured parameters. While the conductivity and electroosmotic coefficient have been well characterized with regard to their temperature and water-content dependences, the transport coefficient is slightly more complicated. Due to the intricacies of Schröder's paradox, some models will utilize a permeability, some a diffusion coefficient, some a binary interaction parameter, and some a transport coefficient. The value of those coefficients should be more-or-less interchangeable under the same conditions (*i.e.*, temperature and water content), and thus many models can get by with using nonphysical values for the diffusion coefficient (*e.g.*, step changes and values at supersaturated conditions) for example. While this might yield satisfactory trends and data predictions, it is probably best to use diffusion coefficients for vapor-equilibrated membranes and permeabilities for liquid-equilibrated ones as done by Weber and Newman[64] for their transport coefficient for example. It is worth noting that for all of the transport parameters, their values increase with both temperature and humidity (*i.e.*, a liquid-equilibrated value is higher than the corresponding vapor-equilibrated one).

2.2.3 Other transport through the membrane

In terms of membrane modeling and understanding full-cell behavior including water management, one must recognize that other species may be transported through the membrane. Of largest interest is the transport of hydrogen and oxygen. The crossover of these gases results in a mixed potential at the electrode—thus explaining the difference between the observed open-circuit potential and the equilibrium potential (see Figure 2)—and a chemical short of the cell. Although the crossover is normally only a small efficiency loss, it does limit the thickness of the membrane,[78] and can become important if pinholes or membrane thinning occur. Furthermore, crossover is attributed to carbon corrosion during fuel starvation,[49] platinum band formation,[45] and peroxide generation.[43] In addition, recent studies have also shown that the dilution effect by crossover of nitrogen can be important.[79]

For the above reasons, membrane modeling should account for gas crossover. The easiest method to do this is to use experimentally measured permeation coefficients (which increase with water content and temperature)

$$\mathbf{N}_i = -\psi_i \nabla p_i \tag{28}$$

where ψ_i and p_i are the permeation coefficient and partial pressure of species i, respectively. A dilute solution approach can be used since the gases are minor components inside the membrane. Also, permeation coefficients are used instead of separate diffusion and solubility coefficients since it simplifies the analysis and the need for experimental data.

Besides gases, the other species' transport not addressed above is that of ions besides protons. Positive valence contaminant ions can occur in the membrane due to such issues as platinum and cobalt dissolution from the cathode,[46] ruthenium dissolution from the anode,[80] air impurities,[81,82] and contamination from the other PEFC components (*e.g.*, bipolar plates).[81,83] All of these cations will ion-exchange with the protons to a certain degree and thus decrease the conductivity of the membrane. While modeling these effects is out of the purview of this chapter, a brief modeling approach is as follows. While one can use dilute-solution approaches due to their low concentrations, it is suggested that more concentrated-solution-theory equations be used since the ions interact strongly with the proton and possibly water movement. Thus equations in the form of equations 21 or 22 should be added for each ion, and rate and/or equilibrium affinities between the ions and membrane included. In addition, since the membrane no longer holds only a single type of positive charge, electroneutrality (equation 18) must also be included. Finally, the resulting binary interaction parameters will result in the need to measure such transport properties as transference numbers for each ion.[26] It should be noted that the above approach is also required in any case where there are multiple ions (either anion or cation) that are mobile, such as ionic-liquid electrolytes, impregnated membranes (*e.g.*, PBI), *etc*.

2.3 Two-Phase Flow

It is well known that water and specifically liquid-water management is crucial in performance optimization and perhaps durability mitigation. Fuel cells that operate below 100°C have the problem that water exist both in vapor and liquid forms. This two-phase-flow problem is a critical aspect for PEFC modeling. In fact, recent trends in PEFC modeling show a focus on understanding two-phase flow more than any other phenomena. One problem is that the necessary parameters related to two-phase flow in PEFCs are still mainly unknown due to inadequate experimental methods that can probe the complex materials used. Although progress on this front is being made, such as advanced imaging techniques, there is still a long way to go.

Simultaneous flow of both liquid and gas occurs within the GDLs and CLs, although most modeling studies focus on the former due to the fact that the CLs are much thinner than the GDLs and also contain a membrane phase and electrochemical reaction that complicate the transport picture. Furthermore, most GDLs are composite structures with a relative thick macroporous layer combined with one or more microporous layers of tailored properties such as wettability. In this section, the general, macroscopic treatments and governing equations of two-phase flow are presented. Specifically, the transport equations for the two fluids and their interaction with each other is discussed since the mass balances of the gas-phase species and liquid water can be deduced from equation **Error! Reference source not found.**. In later sections, more detailed analyses of water movement in GDLs in terms of parameter expressions, specific phenomena, simulation results, and microstructure are given.

Before proceeding to the introduction of the governing equations, some general comments should be made. Although GDLs and two-phase flow have been getting more interest in terms of their ability to tune water management, the macroscopic modeling methodology is essentially at the same state-of-the-art as when it was last reviewed.[2,3] A lone exception is the model of Promislow *et al.*[84] that provides a mathematically less intensive methodology to account for vapor-liquid interfaces, and the so-called dry to liquid transition either along the channel or within the GDL itself. Since those reviews, several aspects dealing with water management have been explored, but the methodologies have remained essentially the same. The most noteworthy aspects are the examination of composite and even graded structures (*i.e.*, GDL and MPLs), the coupling between thermal and water management (*e.g.*, heat-pipe effect), examination of anisotropic and in-plane properties, inclusion of more microstructural details through microscopic models, the examination of interactions between the GDL and the flow channel, and the inclusion of a wettability distribution within the porous matrix. All of these aspects are discussed in other sections of this chapter with the exception of the last. The idea of having separate hydrophilic and hydrophobic pores was popularized for PEFCs by Weber *et al.*[85] and Nam and Kaviany.[86] Since then, it has become much more common to measure both types of distributions and use them in modeling analyses (see Gostick *et al.*[87] for example). However, although one can measure hydrophilic distributions, it is noted that typical GDLs act more hydrophobic than hydrophilic on average (*e.g.*, one must initially apply a pressure to wet the material[88]).

2.3.1 Liquid-phase transport

There are various methodologies to treat the liquid water. The first and simplest is to treat it as a mist or fog flow in that it has a defined volume fraction but moves with the same superficial velocity of the gas. While this could be satisfactory for flow fields, it does not make physical sense within a porous medium. The more common method is to use a separate transport equation for the liquid phase. Typically, this is done using the empirically based Darcy's law

$$\mathbf{N}_{w,L} = -\frac{k}{\overline{V}_w \mu} \nabla p_L \tag{29}$$

where $\overline{V}_w$ is the molar volume of water, k is the effective permeability, μ is the viscosity, and all of the properties are valid for pure water. Some models also account for water movement using the Navier-Stokes equations, although Darcy's law is typically added as a source term that dominates the transport. Finally, some of the extensions of Darcy's law, such as the Brinkman equation, which allow for the no-slip condition to be met at the particle surfaces (*i.e.*, a second derivative of pressure is used) have been used in simulations,[89] although for the most part Darcy's law is used. While Darcy's law is a simple equation to implement, the challenge comes in how one calculates the effective permeability. This issue, along with saturation, is at the core of two-phase-flow models, and is discussed briefly below after introducing the gas-phase transport equations.

2.3.2 Gas-phase transport

To treat the gas-phase transport, the generalized multicomponent Stefan-Maxwell equations are used,

$$\nabla x_i = -\frac{x_i}{RT}\left(\overline{V}_i - \frac{M_i}{\rho_G}\right)\nabla p_G + \sum_{j \neq i} \frac{x_i \mathbf{N}_j - x_j \mathbf{N}_i}{\varepsilon_G c_T D_{i,j}^{\mathrm{eff}}} \tag{30}$$

where one of the equations is dependent on the others since the sum of the mole fractions is unity. In the above equation, ρ_G is the density of the gas phase, x_i and M_i are the mole fraction and molar mass of species i, respectively, and the first term accounts for pressure diffusion. This term is often neglected, although it could be important on the anode side of the cell due to the vast differences in molar mass between hydrogen and water.[90] In the second term, c_T is the total concentration or molar density of all of the gas species, ε_G is the volume fraction of the gas phase, and $D_{i,j}^{\text{eff}}$ is the effective binary interaction parameter between *i* and *j*; by the Onsager reciprocal relationships, $D_{i,j}^{\text{eff}} = D_{j,i}^{\text{eff}}$ for ideal gases. The effective diffusion coefficient is defined as

$$D_{i,j}^{\text{eff}} = \frac{1}{\tau_G} D_{i,j} \tag{31}$$

where τ_G is the tortuosity of the gas phase. Both the gas-phase volume fraction and tortuousity depend on the saturation, *S*, or pore volume fraction of liquid. While this is straightforward for the gas-phase volume fraction

$$\varepsilon_G = \varepsilon_o (1 - S) \tag{32}$$

where ε_o is the porosity of the medium, the tortuosity is another story. Typically, a Bruggeman expression is used for the tortuosity[91-94]

$$\tau_G = \varepsilon_G^{-0.5} \tag{33}$$

However, it is believed that the above expression underpredicts the tortuosity and more complicated expressions or analyses are required or as is often the case, the tortuosity is used as a fitting parameter.

The Stefan-Maxwell equations stem from looking at the velocity of the individual species relative to a reference state. This reference state is typically assumed to be the laboratory reference frame *(i.e.*, stationary), which allows for the Stefan-Maxwell equations to account for not only diffusive fluxes but also convection. For example, for a two component system, the Stefan-Maxwell equations will result in the equation of convective diffusion,

$$D_i \nabla^2 c_i = \mathbf{v}_G \nabla c_i \tag{34}$$

which is sometimes used in the simulation of PEFCs. In the above expression, **v** is the mass-averaged velocity of the gas phase

$$\mathbf{v}_G = \frac{\sum_{i \neq s} M_i \mathbf{N}_i}{\rho_G} \tag{35}$$

As the pore size decreases, molecules collide more often with the pore walls than with each other. This movement, intermediated by these molecule-pore-wall interactions, is known as Knudsen diffusion.[95] In this type of diffusion, the diffusion coefficient is a direct function of the pore radius.[50] In the models, Knudsen diffusion and Stefan-Maxwell diffusion are treated as mass-transport resistances in series,[50,96] and combined to yield

$$\nabla x_i = -\frac{\mathbf{N}_i}{c_T D_{K_i}^{\mathrm{eff}}} + \sum_{j \neq i} \frac{x_i \mathbf{N}_j - x_j \mathbf{N}_i}{c_T D_{i,j}^{\mathrm{eff}}} \tag{36}$$

where the $D_{K_i}^{\mathrm{eff}}$ is the effective Knudsen diffusion coefficient. In effect, the pore wall, with zero velocity, constitutes another species with which the diffusing species interact, and it determines the reference velocity used for diffusion.[97] The above equation also can be derived from a dusty-gas analysis.[98]

From an order-of-magnitude analysis, when the mean-free path of a molecule is less than 0.01 times the pore radius, bulk diffusion dominates, and when it is greater than 10 times the pore radius, Knudsen diffusion dominates. This means that Knudsen diffusion is significant when the pore radius is less than about 0.5 μm, which occurs in MPLs, CLs, and macroporous

GDLs where there is a high saturation thereby resulting in only the small hydrophobic pores being open for gas flow.

Although the Stefan-Maxwell equations account for convection, another relation is necessary to determine the pressure drop within the porous media. This is typically accomplished in the same fashion as liquid-water flow above, *i.e.*, Darcy's law for the gas phase

$$\mathbf{v}_G = -\frac{k_G}{\mu_G}\nabla p_G \tag{37}$$

where k_G is the effective gas permeability.

Equation 37 can be either used as a separate momentum equation to determine the pressure, or it can be thought of as an additive term to the Stefan-Maxwell equations a la the dusty-gas model[98]

$$\nabla x_i = -\frac{x_i k_G}{D_{K_i}^{\text{eff}}\mu_G}\nabla p_G + \sum_{j\neq i}\frac{(x_i\mathbf{N}_j - x_j\mathbf{N}_i)}{c_T D_{i,j}^{\text{eff}}} - \frac{\mathbf{N}_i}{c_T D_{K_i}^{\text{eff}}} \tag{38}$$

However, this treatment is not rigorously correct since there is no strong justification for being able to combine the bulk-fluid velocity with the transport equations linearly in general.

2.3.3 Coupling between liquid and gas phases

It is well known that gas and liquid interact to a certain extent in a porous medium.[99-101] This interaction is embedded in terms of the transport parameters and how they depend on the saturation of the medium (*e.g.*, see equation 32). For variables such as permeability, everything from empirically determined dependences from soil studies to cut-and-random-rejoin bundle-of-capillary models have been used; typically, a more-or-less cubic dependence is utilized. It is worth noting that to date no one has been able to measure successfully the permeability functionality for PEFC materials, due in part to their thinness and very complicated, chemically heterogeneous microstructure. Saturation and the saturation dependences of the various transport parameters are the main way in which flooding is accounted.

While saturation is a key concept, it is actually a dependent and not an independent variable. To determine the saturation, one uses the independent variables of gas and liquid pressures, which are characterized by a capillary pressure[100-103]

$$p_C = p_L - p_G = -\frac{2\gamma\cos\theta}{r} \tag{39}$$

where γ is the surface tension of water, r is the pore radius, and θ is the internal contact angle that a drop of water forms with a solid. Equation 39 is based on how liquid water wets the material; hence, for a hydrophilic pore, the contact angle is $0° \leq \theta < 90°$, and for a hydrophobic one, it is $90° < \theta \leq 180°$. To calculate the saturation from the capillary pressure, there are various methodologies: one can use it as a fitting parameter; one can use empirically determined functions (*e.g.*, Leverett *J*-function[86,103]), although these usually stem from hydrophilic soil analyses; one can develop detailed microscopic and/or pore-network models; or one can use macroscopic idealizations such as a bundle of capillaries.

Before proceeding, it is of interest to examine the issue of whether a high capillary pressure and hence flooding is a result of an increasing liquid pressure relative to the gas one or a decreasing gas pressure relative to the liquid one. Doing a back-of-the-envelope calculation yields the results shown in Figure 6. For the calculation, a current density of 1 A/cm^2 is used to determine the fluxes by Faraday's law and typical water crossover values, saturated air at 65°C is fed, and a cubic dependence of the permeability on saturation is assumed. The figure displays the expected pressure at the cathode GDL/CL interface as a function of the average saturation (assumed uniform) of the GDL and the absolute permeability, which is a function of the GDL microstructure alone. First, it should be pointed out that this simple calculation shows that the gas velocity is three-orders of magnitude higher than the liquid one due to the low gas density. However, as discussed in section 3.2.3, when nonisothermal effects are accounted for, the water-vapor flux will switch direction for fully humidified conditions and the gas-phase velocity can decrease substantially due to this heat-pipe effect. Due to the velocity differences, flooding due to a relative decrease in the gas pressure results in a wider saturation window than flooding due to a relative increase in the liquid pressure. Therefore, gas-phase pressure drops should be accounted for. The figure also gives rough design guidelines for the GDL. For example, for a given permeability, it is apparent that the GDL should operate at a low but not too low (*e.g.*, 20%) saturation to enable good gas and liquid transport; of course, the simple analysis that yields Figure 6 does not account for the feedback between the capillary pressure and the saturation. Finally, the increase in liquid pressure with lower absolute permeability displays the fact that small-pore layers (*e.g.*, MPLs) can be used to pressurize the liquid, as long as they remain at relatively low saturations (*i.e.*, very hydrophobic) to avoid the decrease in gas pressure; this is discussed in more detail in section 3.2.2.

While the above two-phase flow equations are sufficient for modeling purposes, their implementation can result in convergence and stability issues. For this reason, various simplifications and alternative methodologies have been used. The first such methodology is to use the saturation as the driving force, resulting in a governing equation of

$$\mathbf{N}_{w,L} = -D_S \nabla S \tag{40}$$

where D_S is a so-called capillary diffusivity

$$D_S = \frac{k}{\mu \bar{V}_w} \frac{dp_C}{dS} \tag{41}$$

Although the above equation is valid, it gives the false impression that the saturation is the driving force for fluid flow, and that a saturation condition should be used as a boundary condition. Furthermore, care must be taken in the interpretation of the capillary diffusivity.

Another simplification is to assume that the liquid and water vapor are in equilibrium, which is not a bad assumption since they have a large interfacial contact area within the porous medium. This assumption allows one to combine the two material balances so that there is only one for water, and the evaporation/condensation rate does not have to be explicitly calculated. One of the material-balance equations is then replaced by the equilibrium expression given by the Kelvin equation[100]

$$p_0^{\text{vap}} = p_{0,\text{o}}^{\text{vap}} \exp\left(\frac{p_C \bar{V}_w}{RT}\right) \qquad [42]$$

where $p_{0,\text{o}}^{\text{vap}}$ is the uncorrected (planar) vapor pressure of water and is a function of temperature. The treatment of water in this manner greatly enhances the convergence and stability of the numerical simulation.

Related to the above equilibrium methodology is the multiphase mixture model[104,105] typically used in computational-fluid-dynamics models. This model uses algebraic manipulations to convert the two-phase flow equations to a pseudo single phase. Thus, although the two-phase mixture moves at a calculated mass-average velocity, interfacial drag between the phases and other conditions allow each separate phase velocity to be determined. The liquid-phase velocity is found by [104,106]

$$\mathbf{v}_L = \lambda_L \frac{\rho_m}{\rho_L} \mathbf{v}_m + \frac{k\lambda_L(1-\lambda_L)}{\varepsilon_o \rho_L \nu_m} \left[\nabla p_C + (\rho_L - \rho_G)\mathbf{g} \right] \tag{43}$$

where the subscripts m stands for the mixture, ρ_k and ν_k are the density and kinematic viscosity of phase k, respectively, and λ_L is the relative mobility of the liquid phase

$$\lambda_L = \frac{k_{r,L} / \nu_L}{k_{r,L} / \nu_L + k_{r,G} / \nu_G} \tag{44}$$

In equation 43, the first term represents a convection term, and the second comes from a mass flux of water that can be broken down as flow due to capillary phenomena and flow due to interfacial drag between the phases. The velocity of the mixture is basically determined from Darcy’s law using the properties of the mixture. The appearance of the mixture velocity is a big difference between this approach and other pseudo-one-phase models. While the use of the multiphase mixture model does speed computational time and decreases computational cost, problems can arise if the equations are not averaged correctly. Also, this approach does not necessarily agree with literature data and the physical picture. For example, it is unclear whether the pseudo one-phase treatment can allow for variable pore-size distribution and mixed wettability effects to be considered.

2.4 Electron Transport

Although not directly tied to water management, for completeness of the governing equations, electron transport needs to be modeled. For all of the electronically conducting materials, electron transport is modeled with Ohm's law and an effective conductivity that accounts for the volume fraction of the electronically conducting phase and its tortuosity.

$$\mathbf{i}_1 = -\sigma_o \varepsilon_1^{1.5} \nabla \Phi_1 \tag{45}$$

where ε_1 and σ_o are the volume fraction and electrical conductivity of the electronically conducting phase, respectively. The above equation has been adjusted for porosity and tortuosity using a Bruggeman correction. For most PEFC components, carbon is the conducting phase, with water, air, membrane, and Teflon® being insulating. Although most of the relevant PEFC layers are conductive enough not to warrant too much concern with ohmic drops, full-size cells or thin GDLs with low in-plane conductivity may cause situations wherein there are nonuniformities that are caused by the electron transport.[107-109]

2.5 Catalyst-Layer Modeling

The CLs are the thinnest layer, but the most complex in a PEFC. Inside the CLs, the electrochemical reactions take place in an environment where all of the various phases exist. Thus, the membrane and two-phase-flow models must be used in the CL along with additional expressions related to the electrochemical kinetics on the supported electrocatalyst particles. A schematic of a typical PEFC CL is shown in Figure 7, where the electrochemical reactions occur at the two-phase interface between the electrocatalyst (in the electronically conducting phase) and the electrolyte (*i.e.*, membrane). Although a three-phase interface between gas, electrolyte, and electrocatalyst has been proposed as the reaction site, it is now not believed to be as plausible as the two-phase interface, with the gas species dissolved in the electrolyte. This idea is backed up by various experimental evidence, such as microscopy, and a detailed description is beyond the scope of this chapter. Experimental evidence also supports the picture in Figure 7 of an agglomerate-type structure where the electrocatalyst is supported on a carbon clump and is covered by a thin layer of membrane, which may then be covered by a thin film of liquid water.[110-114] Figure 7 is an idealized picture, and the actual structure is probably more of a "spaghetti and meatball" structure, where the carbon agglomerates are connected to each other and covered by thin tendrils of membrane.

As discussed in our recent review,[2] various modeling approaches have been used for the CLs. In this chapter, we focus only on the most relevant ones. In accordance with the experimental picture, the modeling consensus is that an embedded agglomerate model is required for the CLs (see, for example, references [2] and [58]). In fact, recent studies have clearly shown that treating the cathode CL as an interface with uniform properties leads to several erroneous conclusions, especially due to the impact of channel-rib effects that distribute the electrons, water, heat, and oxygen unevenly at the CL boundary.[115-118] While an embedded agglomerate model is now utilized in most models, there is still an effort towards including more microstructural details. Without such inclusions, optimization studies and analysis become too far removed from reality. While most models do this inclusion using a more macrohomogeneous approach as detailed below, there are two notable exceptions. The first, by Wang *et al.*,[119,120] assumes a random microstructure and solves the macroscopic equations through such a network. These results provide a nice link between the macroscopic and the microscopic analyses; however, the models are still too computationally costly to be used in complete full-cell simulations without requiring simplifications of the other layers. That being said, the model allows one to get a handle on such effects as tortuosity and inactive regions (whether that is catalyst, ionomer, or gas pores) in the layer. For tortuosity, they predict a Bruggeman coefficient (see equation 33) for each phase equal to 3.5, which does change with phase volume fraction. However, the deviations can be minimized if the effective or active phase volume fraction is used instead of the overall value.

The idea of active phase volume fraction was also examined by Farhat,[121] who did a statistical analysis to determine what percentage of the three phases (ionomer, platinum, and gas) are in contact with each other and thus where reaction can proceed. Such an analysis is interesting, but the low platinum site utilization number it provides (22 %) assumes that an exact three-phase contact needs to exist for reaction. This is not necessarily the case since if the ionomer film over the catalyst is thin, it may be that it is a two-phase contact, and the gas-phase just needs to be near the covered reaction site. Also, it is possible that the ionomer also only needs to be near the platinum for protons to react. The truth is that the exact microstructure and especially the dynamic, operating one is currently unknown. What is established is that 100 % utilization of the platinum does not occur even with no gas-transport limitations since the platinum may be isolated and no longer in electrical contact with the carbon, or it could be far inside the primary pores of the carbon and thus inaccessible to protons and gas.[122]

Similar to the approach of Wang *et al.*, Durand and coworkers[123-127] use spherical agglomerate structures in a regular (not random) 3-D hexagonal arrays. In between the agglomerates, there are either gas pores or the region is flooded with electrolyte. The equations solved are mainly Ohm's law and Fick's law with kinetic expressions, which is a simpler analysis than that of Wang and coworkers. The results of the models show the concentration contours around a particle and agree with experimental current densities and trends. Such a model also allows for the detailed placement of the electrocatalyst particles to be studied and the various performance gains realized, even though it may not yet be possible to make such an arrangement experimentally.

2.5.1 Modeling equations

The kinetic equations for the main HOR and ORR reactions were introduced in section 2.2.2, including some mention about possible side reactions. As noted above, in addition to the electrode and kinetic interactions, two-phase flow and membrane models must be used. This is typically done by utilizing the models discussed in sections 2.2 and 2.3 above, but accounting for the fact that their volume fractions are not unity. For the two-phase flow equations, this does not really change their expressions, except that the material balances must be altered to account for the reaction rates as discussed below. One change may be in the concept of electrode flooding, which is also discussed below. For the membrane equations, one must now account for the fact that its volume fraction is not unity. Thus, the transport properties must be altered to account for the dispersed phase by something like a Bruggeman relation. In addition, the correct superficial fluxes must be used through the use of membrane volume fractions. Finally, it is still unknown whether the ionomer in the CLs behaves in the exact same fashion as that in the separator. For example, do the ionomer tendrils in the CL swell in the same manner as in the membrane, or is the CL ionomer dominated by interfacial and surface effects? Research both through first-principle modeling and detailed experimentation is still ongoing to answer these and similar questions. From the macroscopic modeling perspective, with few exceptions, the same membrane equations and properties are used in both the separator and the CLs, and swelling is ignored in the CLs.

The kinetic expressions result in transfer currents that relate the potentials and currents in the electrode (platinum on carbon) and membrane phases as well as govern the consumption and production of reactants and products,

$$\nabla \cdot \mathbf{i}_2 = -\nabla \cdot \mathbf{i}_1 = a_{1,2} i_h \tag{46}$$

where $-\nabla \cdot \mathbf{i}_1$ represents the total anodic rate of electrochemical reactions per unit volume of electrode and i_h is the transfer current for reaction *h* between the membrane and electronically conducting solid (*i.e.*, equations 14 and 15 for the HOR and ORR, respectively). The above charge balance assumes that faradaic reactions are the only electrode processes (i.e., it neglects crossover and other side reactions); double-layer charging is neglected (as is appropriate under steady-state conditions). This equation can be used in the conservation-of-mass equation (**Error! Reference source not found.**) to simplify it. For example, if the ORR is the only reaction that occurs at the cathode, the following mass balance results

$$\nabla \cdot \mathbf{N}_{\mathrm{O}_2,G} = -\frac{1}{4F} a_{1,2} i_{0_{\mathrm{ORR}}} \left(\frac{p_{\mathrm{O}_2}}{p_{\mathrm{O}_2}^{\mathrm{ref}}} \right) \exp\left(-\frac{\alpha_c F}{RT} (\eta_{\mathrm{ORR}}) \right) = \frac{1}{4F} \nabla \cdot \mathbf{i}_1 \tag{47}$$

Before discussing the models in more depth, a note should be made concerning catalyst loading. Many models use platinum loading in their equations, especially for optimizing designs and in normalizing the current produced (equivalent to a turnover frequency in catalysis). In this respect, the catalyst loading, m_{Pt}, is the amount of catalyst in grams per PEFC geometric area. If a turnover frequency is desired, the reactive surface area of platinum, A_{Pt}, can be used (usually given in m^2/g). This area can be related to the radius of a platinum particle assuming perhaps a certain roughness factor, but more often is experimentally inferred using cyclic voltammetry measuring the hydrogen adsorption. These variables can usually be determined and then used to calculate the specific interfacial area between the electrocatalyst and electrolyte,

$$a_{1,2} = \frac{m_{\mathrm{Pt}} A_{\mathrm{Pt}}}{L} \tag{48}$$

where L is the thickness of the catalyst layer. This assumes a homogeneous distribution of electrocatalyst in the CL.

A factor closely related to the catalyst loading is the efficiency or utilization of the electrode. This tells how much of the electrode is actually being used for electrochemical reaction and can also be seen as a kind of penetration depth. In order to examine ohmic and mass-transfer effects, sometimes an effectiveness factor, E, is used. This is defined as the actual rate of reaction divided by the rate of reaction without any transport (ionic or reactant) losses. As noted above, a value of 100% efficiency ($E = 1$) does not necessarily correspond to the loading of catalyst but instead to the electrochemically active catalyst area.

In the CLs, there are two main length scales and both are important. The two scales are the whole layer and the agglomerate (see Figure 7). To account for both the local agglomerate level as well as effects across the porous electrode, an embedded agglomerate model is used. In this type of model, the traditional porous electrode equations are used to calculate the gas composition and the overpotential change across the CL due to ohmic, mass-transfer, and reaction effects, and the agglomerate model is used for the reaction site to determine the correct transfer current density. In this fashion, the embedded agglomerate model is essentially a pseudo 2-D model where one dimension is the electrode and the other is into the agglomerate (obviously if one is doing a multiple dimensional model, then the agglomerate is an additional pseudo dimension which is a microscopic-scale dimension).

In terms of the porous electrode equations, no new relations are required. As noted above, the membrane equations and two-phase flow equations are used with appropriate scaling factors, and the reaction rates are determined from the agglomerate model presented below. From a historical and reference perspective, Euler and Nonnenmacher[128] and Newman and Tobias[129] were some of the first to describe porous-electrode theory. Newman and Tiedemann[130] review porous-electrode theory for battery applications, wherein they had only solid and solution phases. The equations for when a gas phase also exists have been reviewed by Bockris and Srinivasan[131] and DeVidts and White,[132] and porous-electrode theory is also discussed by Newman and Thomas-Alyea[26] in more detail.

The main function of the agglomerate model is to obtain the correct transfer or reaction current density. One of the most detailed applications of this model is that of Shah *et al.*[133] In their model, they account for such impacts as membrane swelling, inactive catalyst in the agglomerate pores, surface films of both ionomer and water if the vapor phase is saturated, and the number and dispersion of agglomerates. Furthermore, they do everything in a geometrically and material-balance consistent manner. Such an in-depth model allows for detailed analysis to be done in terms of impacts of flooding and other CL resistances and structural parameters on performance.

For the agglomerate model, the characteristic length scale is the radius of the agglomerate, R_{agg}, and all of the agglomerates are assumed to be the same shape and size. This assumption does not necessarily agree with reality, and it would be better to have a distribution or even a discrete few agglomerates with different radii. In the agglomerate model, the reactant or product diffuses through the electrolyte film surrounding the particle and into the agglomerate, where it diffuses and reacts. Hence, there is a concentration and possibly a potential and temperature distribution within the agglomerate. The equations for modeling the agglomerate are similar to those presented above (*i.e.*, mass balances, kinetics, energy balance, *etc.*) in spherical coordinates. As mentioned above, the role of the agglomerate model is to determine how the transfer current density should be altered, and this is typically done using an effectiveness factor, resulting in

$$\nabla \cdot \mathbf{i}_2 = a_{1,2} i_h E \tag{49}$$

As an example, if one takes the ORR to be a first-order reaction following Tafel kinetics, the solution of the mass-conservation equation in a spherical agglomerate yields an analytic expression for the effectiveness factor of[50,134]

$$E = \frac{1}{3\phi^2}\left(3\phi \coth(3\phi) - 1\right) \tag{50}$$

where ϕ is the Thiele modulus for the system[135]

$$\phi = \frac{R_{\mathrm{agg}}}{3}\sqrt{\frac{k'}{D^{\mathrm{eff}}_{\mathrm{O_2,agg}}}} \tag{51}$$

where k' is a rate constant given by

$$k' = \frac{a_{1,2}\, i_{0_{\mathrm{ORR}}}}{4F c^{\mathrm{ref}}_{\mathrm{O_2}}} \exp\left(-\frac{\alpha_c F}{RT}(\eta_{\mathrm{ORR}})\right) \tag{52}$$

where the reference concentration is that concentration in the agglomerate that is in equilibrium with the reference pressure

$$c^{\mathrm{ref}}_{\mathrm{O_2}} = p^{\mathrm{ref}}_{\mathrm{O_2}} H_{\mathrm{O_2,agg}} \tag{53}$$

where $H_{\mathrm{O_2,agg}}$ is Henry's constant for oxygen in the agglomerate. While the above analytic solution is nice, if the reaction is not first order or if one wants to account for varying potential and/or temperature within the agglomerate, the relevant governing equations must be solved numerically with the correct surface boundary conditions to determine *E*.

If external mass-transfer limitations can be neglected, then the surface concentration in equation 61 can be set equal to the bulk concentration, which is taken from solving the porous electrode equations. Otherwise, the surface concentration is unknown and must be calculated. To do this, an expression for the diffusion of oxygen to the surface of the agglomerate is written

$$W_{\mathrm{O_2}}^{\mathrm{diff}} = A_{\mathrm{agg}} D_{\mathrm{O_2,film}} \frac{c_{\mathrm{O_2}}^{\mathrm{bulk}} - c_{\mathrm{O_2}}^{\mathrm{surf}}}{\delta_{\mathrm{film}}} \tag{54}$$

where $W_{\mathrm{O_2}}^{\mathrm{diff}}$ is the molar flow rate of oxygen to the agglomerate, A_{agg} is the specific external surface area of the agglomerate, and the film can be either membrane or water (if two or more films are desired, similar expressions can be written for each film). The above expression uses Fick's law and a linear gradient, which should be valid due to the low solubility of oxygen and thinness of the film. At steady state, the above flux is equal to the flux due to reaction and diffusion in the agglomerate (as well as the flux through any other films), and thus the unknown surface concentration(s) can be replaced. Doing this and using the resultant expression in the conservation equation 47 yields

$$\nabla \cdot \mathbf{i}_1 = 4Fc_{\mathrm{O_2}}^{\mathrm{bulk}} \left(\frac{1}{\dfrac{\delta_{\mathrm{film}}}{A_{\mathrm{agg}} D_{\mathrm{O_2,film}}} + \dfrac{1}{k'E}} \right) \tag{55}$$

This equation is the governing equation for the agglomerate models for the cathode under the assumptions of first-order reaction, isothermal and isopotential agglomerate. One also can write the above factor as an overall effectiveness factor. If desired, this factor could be used as a fitting parameter, thereby avoiding the necessity of detailed calculations and perhaps multiple fitting parameters on the agglomerate scale. A final analysis would be to assume that $E = 1$ and just calculate the effect of the covering films on the reaction rate. Physically, such an analysis assumes that only the platinum on the agglomerate surface is active, or in other words, the buried platinum is inactive perhaps due to inadequate contact with the ionomer.

Before examining some of the modeling results in terms of impacts on water management and optimization, it is worthwhile to mention CL flooding. The way in which CL flooding is accounted for is by two different approaches. The first, as noted above, is to assume a liquid film that forms and provides an extra mass-transfer resistance to the reactant gas. The second is more of a macrohomogeneous approach wherein the two-phase-flow equations are used to alter the value of the transfer current using the saturation

$$a_{1,2} = a_{1,2}^{\mathrm{o}}(1 - S) \tag{56}$$

where $a_{1,2}^{\mathrm{o}}$ is the maximum or dry specific interfacial area. In comparing the two approaches, it seems that the saturation approach allows for greater reaction rates (higher current densities). The reason is that the CLs have small pores which are at least partially hydrophobic, and thus it takes a high liquid pressure to flood them (depending on the assumed contact angle), whereas even a thin film can effectively shut down the reaction. Of course, the film is spread over a much larger surface area and depends on the agglomerate radius. It is tough to say which approach is better as they both have their advantages and disadvantages, with the agglomerate-film perhaps more physically realistic assuming that the agglomerate parameters are well known. Finally, one should be cognizant that it is hard to say whether flooding in the GDLs or the CLs is more dominant, and one can tailor the relative influence of each by changing the underlying model used; more experimental evidence is required on this front before a definitive conclusion can be reached.

2.5.2 Optimization analyses

A good embedded agglomerate model can help to predict optimal microstructural parameters for improved performance. However, since even some of the more complicated models still make several assumptions such as uniform agglomerate shape and size, the resulting optimizations provide only future experimental research directions. That being said, the results of such models do help to guide intuition, design experiments and structures, and examine how CLs operate.[136] Recent models mainly examine distributions of platinum, Nafion®, operational changes, and material properties such as agglomerate wettability and CL thickness.[133,137-140] While most of the models deal with experimentally-based values, some look at possible structures that are more ordered and perhaps experimentally unobtainable currently.[141]

A mentionable model is that of Eikerling,[140] who does a comprehensive macrohomogeneous approach using structural properties of the CL. His model is similar to that of Weber *et al.*,[85] but goes beyond it in terms of analyzing the effect of water content on both the primary and secondary pores within the agglomerate. Specifically, Eikerling calculates the critical saturation and conditions for optimal performance (*i.e.*, primary pores flooded and secondary ones empty). Although the model does have some drawbacks based on its simplifications (such as a single contact angle and no membrane or GDL models), it does do a good job in demonstrating the intricate balance needed in water and thermal management.

The model of Shah *et al.*[133] does a detailed analysis of CL flooding showing how relative humidity, temperature, and water exit towards the channel cause nonuniform and suboptimal performance. They also investigate the effect of CL and GDL capillary properties, showing that changing the GDL properties has a larger impact than those of the CL on overall saturation and performance. The model of Wang *et al.*[138] demonstrates that functionally gradient materials can have a significant impact on performance. While they state that 35% Nafion is the optimal loading due to a competition between ionic and gas transports, they show that having more ionomer nearer to the membrane improves performance by about 10% while having the opposite gradient results in substantially lower performance due to a much lower overall oxygen concentration within the layer. Thus, oxygen transport has a significantly larger impact on performance than proton conduction.

While the above examples and many others optimize the CL properties individually, there are two noteworthy examples that do a multivariable optimization. The results of such studies indicate that one should not optimize a single variable without considering the others since the optimum can change. For example, Song *et al.*[139] demonstrate that while both ionomer and platinum loadings exhibit optimum values that increase from the membrane to the GDL interface (in agreement with Wang *et al.*), when one considers both loadings, the optimum ionomer loading still remains linear, but the platinum loading adopts a convex shape. A more detailed optimization routine was conducted by Djilali and coworkers,[137] who examined multiple variables such as ionomer volume fraction, platinum-to-carbon ratio, platinum loading, volume fraction of ionomer in an agglomerate, and GDL porosity. Their analyses also examined the impact of operating variables on performance. They show that at high current densities, the optimum structure actually has lower platinum loading than at low current densities so that the CL has a higher porosity and hence enhanced gas flow. Therefore, one must be aware of the expected operating conditions when one does an optimization, and multivariable optimization should be done to realize the true ideal structure. While doing a multivariable optimization can be laborious, there is perhaps opportunity to use such methods as Monte-Carlo algorithms to reach design space previously ignored.

2.5.3 Impedance models

To get a handle on the controlling phenomena and to characterize the CL and the entire PEFC experimentally, AC impedance or electrochemical impedance spectroscopy (EIS) is often used. The idea is that by applying only a small perturbation to the current during operation, the system response can be studied *in situ* and in a noninvasive way. Typically, a frequency range is scanned in order to acquire signatures for the different phenomena which occur with different time constants; however, the very long time constant for water rearrangement inhibits the efficacy of EIS for mapping these phenomena.

To analyze the resulting output, a model of the system is required. These models typically assume an equivalent circuit (which can be relatively complicated) for the various physical processes occurring in the PEFC.[93,142-147] Figure 9 shows an example of such a circuit for a porous electrode where the membrane resistance is also considered. The use of equivalent-circuit analysis is really inadequate for studying operation in detail; however, it is very useful for characterizing the CL and membrane resistances and similar properties. These EIS studies allow one to determine the overall resistances in the PEFC, and notable, those of both the ionic and the electronic pathways in the CL.[93,146] Most of these studies show increased high-frequency resistance as the membrane dehydrates and an increased low-frequency loop as flooding occurs. EIS can also be used to map the changes occurring in the PEFC as a function of time. Such analysis allows for signatures to be determined for degradation concerns, such as those dealing with membrane hydration[148] or increased flooding due to loss of hydrophobicity.[149]

While a good equivalent-circuit representation of the transport processes in a PEFC can lead to an increased understanding, it is not as good as taking a physics-based model and taking it into the frequency domain. These models typically analyze the cathode side of the PEFC.[150-152] An exception is the model of Wiezell *et al.*[153] that analyzed the anode side and the membrane. In their analysis, they show that the HOR mechanistic steps give arise to various loops in the complex domain. In addition, water electroosmotic flow and impact of water on conductivity can also give arise to low-frequency loops that are semi-inductive and can indicate microstructural relaxation of the polymer. Of the cathode models, those of Springer *et al.*[151] and Guo and White[152] are perhaps the most complete. Guo and White utilize an embedded agglomerate model and develop extensive expressions for the various loops and time constants. They focus mainly on gas transport and show how it impacts the EIS spectra. The model of Springer *et al.* also includes a relatively simple membrane model and is based on their previous modeling work,[154] thereby allowing a nice comparison to the predicted governing phenomena and changes within the EIS spectra.

The use of impedance models allows for the calculation of parameters, like gas-phase tortuosity, which cannot be determined easily by other means, and can also allow for the separation of diffusion and migration effects. Overall, impedance is a very powerful experimental tool, especially for characterization and trends, but its results are only as meaningful as the model used for its analysis.

2.6 Model Implementation and Boundary Conditions

To finish this section, it is worthwhile to mention modeling implementation and boundary conditions. Almost all of the models utilize a control-volume approach to solving the equations. This approach is based on dividing the modeling domain into a mesh that determines the control volumes. Using Taylor series expansions, the governing equations are cast in finite-difference form, and typically the governing transport equations have been combined with the conservation equations to yield a set of second-order equations. In this fashion, one is performing conservation equations within each control volume. The exact details of the numerical methods can be found elsewhere (for example, see reference [155]).

The various PEFC layers or domains are linked to each other through boundary conditions. There are two main types of boundary conditions, those that are internal and those that are external. The internal boundary conditions occur between layers inside the modeling domain, and the external are the conditions at the boundary of the entire modeling domain. Typically, coupled conditions are used for internal boundaries wherein the superficial flux and interstitial concentration of a species are made continuous. However, as mentioned above, boundary conditions between the membrane and electrode can involve the fact that there is only ionic current in the membrane and electronic in the GDL. Another common boundary condition is to have a change in concentration because a species dissolves. This is similar to the internal boundary condition in the membrane and is used sometimes where phases are not continuous across the boundary.

The external boundary conditions specify the concentrations and values for all of the species and variables or their fluxes at the boundary. Examples include specifying the inlet conditions such as gas feed rates, composition, temperature, and humidity, or specifying the current density or potential or specifying the thermal flux to the coolant stream. The external boundary conditions are often the same as operating conditions, and therefore are very similar for most simulations, although there can be differences such as what condition is used for two-phase flow (*i.e.*, zero saturation or zero capillary pressure). One of the most important and perhaps most complex boundary conditions is that between the GDL and the flow channel, which can have a substantial impact on water management and performance (for example, see reference [133]); this condition is studied in more detail in section 4.2.2.

3 Water Movement in Gas-Diffusion Layers

Section 2 introduced the governing equations for water movement. While the recent membrane and CL modeling results were discussed in Sections 2.2 and 2.5, respectively, for the GDLs, only the two-phase-flow equations were mentioned (see Section 2.3). Furthermore, the impact of GDL design and optimization is now becoming more important than ever. The reasons are that the GDL has traditionally been a relatively ignored layer, many of the other layers are somewhat set in their designs, and the impact of GDL properties on water management is very significant. In this section, the functioning of the GDL is discussed. The discussion is separated into two parts. The first part focuses on more microscopic and pore-level treatments of liquid and gas transport in GDLs, and the second part discusses some specific modeling analyses with respect to GDL operation and optimization.

3.1 Microscopic Treatments

It is known that a GDL is comprised of carbon fibers which have been treated to be made hydrophobic. The actual microstructure is currently unknown, although imaging techniques such as X-ray tomography as described in Section 1.1, are getting closer. Liquid movement through the layer is similarly hard to quantify experimentally. Figure 9 shows two ideas as to how water moves throughout the GDL microstructure. In both mechanisms, liquid water within the GDL forms preferential pathways that begin to merge into each other and form one larger water conduit to the interface of the GDL with the gas channel. These pathways from through the carbon-fiber interces, and the formation gives rise to a tree-like water distribution (Figure 9(a)). Based on their experimental data, Litster *et al.* [23] propose a fingering and channeling transport method, as seen in Figure 9(b), where instead of small water branches coalescing to form one large break-through path, several water pathways develop in parallel. Once a dominant pathway forms, water from nearby channels is siphoned into the dominant conduit, and a droplet forms at the GDL / gas-channel interface, whereupon it is carried away, and the process begins anew. Although both mechanisms ensure that water moves toward the GDL surface, the initialization points and method vary greatly between the two explanations and can therefore change the creation and results of models. The capillary-tree mechanism will depend strongly on condensation effects within the medium because the initial braches are small. Alternatively, consideration of the channeling mechanism is less dependent on distributed sources throughout the medium and rather on water build-up at the CL / GDL interface. The constant advancing and receding of water also suggests that wetting hysteresis in the system could play a major role in what channels become dominant water pathways.

The end result of the above analysis is that it is hard to predict fluid movement in the physiochemical heterogeneous structure that is a GDL; a macrohomogeneous approach, as discussed in Section 2, is often utilized. Bulk-flow parameters and constitutive relations offer a simple means to capture average fluid movement and simplify the underlying complex geometry of the medium. The Carman-Kozeny equation[100] for determining absolute permeability, Wyllie equation for determining relative permeability,[100] and Leverett *J*-function for determining the capillary-pressure-saturation relationship[103,156] are the most commonly employed relations for modeling water movement through the GDL. The constitutive relations are typically empirically derived but their ability to capture bulk system characteristics is dependent on the assumption that the tested sample size is large enough for one to obtain a representative average and neglect end effects. However, the difficulty of procuring accurate measurements for GDL properties may be gleaned from the spread in the parameter values.[64,116,133,157-161] Furthermore, hysteresis and heterogeneities in the medium complicate quantifications and compromise predictive capabilities of macroscopic models with respect to transient phenomena. Microscopic models are thus becoming necessary to elucidate governing flow mechanisms and to predict differences in flow pathways for yet uncharacterized materials or changes due to GDL manufacturing or PEFC design.

Lattice-Boltzmann simulations have been extended to multi-phase flow,[162-164] and several full-morphology and network models have started to analyze flow through fibrous materials in particular.[165-169] Such microscopic modeling in general is still in the infancy stage and mechanistic understanding of how water moves through different porous media, *i.e.*, as thin films, slugs, droplets, or some combination thereof, is still being studied for both steady-state and transient conditions.[170,171] Nonetheless, some preliminary attempts have been made to derive constitutive relations—namely permeability and capillary-pressure-saturation curves—via direct treatment of microphysiochemical structure.

With respect to derivation of relative permeability for GDLs, Markicevic and Djilali[172] developed a two-scale model for flow around obstacles using saturation and phase length scales as variable parameters. Relative permeability was found to be dependent upon the relative sizes of the saturation and phase length scales. Relative permeability was seen to vary from a linear to nonlinear dependence on saturation depending on whether flow was in the Darcy, Brinkman, or Stokes regime.

The determination of capillary-pressure-saturation curves can be accomplished through the use of pore-network, full-morphology, and Lattice-Boltzmann modeling with pore-network simulations being most common.[167-169] Vogel *et al*.[167] compared the three techniques in terms of computational intensity and predictive capabilities. Pore-network modeling is the most simple of the three, and involves the idealization of a medium and assumption of the pore-size distribution and connectivity of the pores. Provided that these inputs were available, pore-network modeling was found to capture the same trend as the Lattice-Boltzmann model for saturation levels above 0.1. The full-morphology approach incorporates the next level of complexity in that the explicit microstructure of the medium is treated, but imbibition is idealized to proceed by advancement of spheres.[173] A consequence of the approach was consistent overprediction of saturation due to the artificially high intrusion of water into the pore because of the assumption of intrusion by spherical fronts. The Lattice-Boltzmann model was the most rigorous and accounted for interfacial phenomena best, but the detail comes at the price of being computationally expensive and also having the limitation of being grid-spacing dependent.[167]

Because of the relative ease with which pore-network modeling can be executed, attempts have been made to generate capillary-pressure-saturation curves using pore-network models. Sinha and Wang[169] developed an alternative expression for use with the Leverett *J*-function from that proposed by Udell[156] (see equation 61) by generating an idealized GDL structure and solving for the flow pattern as dictated by minimizing capillary pressure for each advancement. Curve fitting resulted in a similar function as that of Udell, except multiplied by a factor of 2.3 and with an additive constant. Schulz *et al.*[168] noted even closer agreement between their pore-network results and the Leverett *J*-function, which is surprising considering that the Leverett *J*-function was derived for soil systems.[103] Schulz *et al.* also went on to predict through-plane permeability at varying compression ratios, and observed reasonable agreement with experimental data despite the fact that neither breaking of fibers nor PTFE coating is taken into account in the simulation.[168]

The next step toward creating realistic GDL domains requires treatment of the wettability heterogeneities in the system. Simulations have yet to conquer the task of solving for constitutive relations for flow in porous media of mixed wettability in any system, let alone in fibrous systems and GDLs, but initial modeling and experimental advances are underway, as seen in Figure 10.[169,174]

3.2 Macroscopic Analyses

The above microscopic treatments allow for a much greater understanding of two-phase flow in the chemical heterogeneous and complex structure of a GDL. However, they are currently too detailed and computationally costly to be linked to the other PEFC layers and used for full-cell analyses. Hence, these analyses typically use the more macroscopic equations introduced in Section 2.3. While most recent models include GDLs using those governing equations in some form or another, many cell-level models now focus on various effects and properties within GDLs. Some of the more important effects and the corresponding simulation studies are detailed below, but before that begins, mention should be made concerning the different macroscopic approaches towards the determination of the transport parameters.

3.2.1 Determining two-phase-flow parameters

As noted in Section 2.3, the main point of two-phase-flow models is the determination of the liquid saturation and hence the gas-phase tortuosity or effective diffusion coefficient. Key among these parameters is the effective permeability of both the liquid and gas phases. As discussed in our previous review,[2] the effective permeability in a PEFC has not been measured accurately experimentally, and there is a multitude of expressions and models to determine it and associated two-phase-flow parameters. Below, a short discussion is given on the two-phase-flow parameters for completeness; the reader is referred to the respective references for more in-depth discussion and analysis.

The effective permeability of a system may be broken into two parts, the saturated or absolute and the relative permeabilities. The saturated permeability, or the permeability at complete saturation, of the medium, k_{sat}, is a function of geometry and microstructure alone, whereas the relative permeability, k_r, accounts for interactions between two or more fluids in a medium. The effective permeability is then taken to be the product of the two

$$k = k_r k_{\text{sat}} \tag{57}$$

Experimentally, the absolute permeability may be found from Darcy's law (Equation 29) by measuring the flowrate across a medium with a known pressure drop. The experiment is simple in principle, but prone to error and edge effects and thus should be performed at multiple flowrates and pressure drops to find the best fit of Darcy's law and ensure complete filling of the pore space by the fluid. The permeability of anisotropic materials is more difficult to ascertain since the three permeabilities are harder to decouple. Another common method for determining absolute permeability is use of the Carman-Kozeny equation,[100]

$$k_{\text{sat}} = \frac{\varepsilon^3}{k'\varepsilon(1-\varepsilon)^2 S_0^2} \tag{58}$$

where k' is the Kozeny constant, which depends on the medium and represents a shape and tortuousity factor, and S_0 is the specific surface area based on the solid's volume. The Carman-Kozeny equation is based on Poiseulle's equation and thus on laminar flow through capillary tubes; any derived permeability is still for idealized, isotropic conditions. Some attempts to incorporate the fibrous nature of GDLs have been made via use of the Ergun equation and fractal theory,[175,176] but without a definitive determination method, absolute permeability values used in models will probably continue to vary and be based on experimental values. The typical range of experimentally and theoretically determined values for k_{sat} is from 10^{-15} to 10^{-9} m^2, with most values lying between 10^{-13} and 10^{-12} m^2.[64,116,133,157,158,160,161,177]

More uniformity between models is seen with respect to the constitutive relation chosen to define the relative permeability. The most common expression is the Wyllie expression and is based on a cut-and-rejoin model of tubes and is used due to its simple form,

$$k_r = S^3 \tag{59}$$

Other options for ascertaining relative permeability include using the Corey[178] (Brooks-Corey)[179] relation, Van Genuchten relation,[180] and a statistical derivation.[64] One point of note is that the above relations are based on permeability experiments and calculations which have been predominantly studied in the context of soil science and oil reclamation. Their applicability to PEFC systems is nebulous because unlike a bed of sand, the GDL comprises a highly porous, mixed wettability, irregularly shaped, and interconnected fibrous microstructure. Nonetheless, most models utilize expressions and relations as developed in hydrological studies, since there are not any for the PEFC components due to experimental difficulties.

The most notable example of a hydrological expression that is applied frequently to PEFC systems is the Leverett expression that relates capillary pressure, P_c, to saturation, S[103]

$$P_c = \gamma \cos\theta \sqrt{\frac{\varepsilon}{k}} J(S) \tag{60}$$

where γ is the surface tension, θ is the contact angle, ε is the porosity, and $J(S)$ is found empirically and known as the Leverett *J*-function. The most commonly used expression for this function is that of Udell[156]

$$
\begin{aligned}
J(S) &= 1.417(1-S) - 2.120(1-S)^2 + 1.263(1-S)^3 && \text{for } \theta < 90^\circ \\
J(S) &= 1.417S - 2.120S^2 + 1.263S^3 && \text{for } \theta > 90^\circ
\end{aligned}
\tag{61}
$$

The applicability of the Leverett *J*-function has been debated.[87,158] One of the main limitations of the Leverett approach in describing a wide range of systems is that the square-root term does not scale across systems of varying topology.[100] Another source of concern has been the differences between the conditions under which the Leverett *J*-function was derived and the characteristics of the GDLs. The Leverett *J*-function was developed for an isotropic soil of uniform wettability and a small particle aspect ratio, whereas a standard GDL is anisotropic, of mixed wettability due to nonuniform PTFE coating—which also complicates the definition of a contact angle—and a large particle aspect ratio as is common for fibrous materials. Besides using a Leverett *J*-function, the only other alternatives are those based on tangential experimental results[181] or those that use an idealized construct.[85] Overall, despite concerns regarding the applicability of various constitutive relations on permeability and pressure-saturation curves, viable alternatives are yet lacking in the field. However, with further development of physically accurate pore-network or Lattice-Boltmann models, probing permeabilities and pressure-saturation curves with simulations is a possibility.

3.2.3 Microporous layers

With the increased understanding of the importance of GDL design, PEFC manufacturers have begun to examine composite GDLs of various layers tuned for specific tasks. The most common design is a bilayer one in which there is a macroporous layer (which is similar to a traditional GDL) and a microporous layer (MPL) (see Figure 1). MPLs are made from carbon black pressed with hydrophobic binder (they are usually hydrophobic) and are anywhere from 0.1 to 20 μm thick, with permeabilities an order of magnitude or two less than GDLs, small pore sizes, and various porosities.[157,182] MPL properties can be tailored by use of different carbons, different carbon-to-binder ratios, use of pore formers, *et cetera*.[182]

The idea behind the addition of the microporous layer is that if a less permeable material is placed between the cathode CL and GDL, water movement into the GDL would decrease and reactant transport increase. Another possible benefit would be to use a partially hydrophilic MPL to wick water away from the cathode CL, thereby decreasing flooding in it. Beyond the duty of water management, MPL incorporation may have the extra benefit of reducing contact resistance between the GDL and CL, increasing the usable active area of the CL, promoting efficient gas redistribution, and protecting the CL from pinhole formation caused by piercings from the GDL fibers. Amazingly, MPLs have improved PEFC performance consistently in experiments,[183-191] with initial empirical optimizations demonstrating increased peak power for composite GDL/MPLs that balance the strengths of high gas permeability and high hydrophobicity.[182] MPL traits that lead to better performance include higher hydrophobicity,[183-185] thinner layers,[190] and micron-sized pores,[191] just to name a few. Such experiments have provided valuable insight into how currently used MPLs compare. The next step underway is to use models to fine tune these general rules of thumb and elucidate what dictates MPL efficacy and how to optimize the MPL material properties for various operating conditions and optimization criteria.

General models that compare strictly the difference in PEFC performance between having a MPL and not show that addition of a MPL leads to more uniform membrane hydration and gas and current distribution over the entirety of the PEFC.[192-194] One of the first MPL-specific works is that of Pasaogullari and Wang,[195] who used a 1-D, half-cell, isothermal, and two-phase model to study the effects of MPL porosity, wettability, and thickness on performance. An interesting result stemmed from a comparison between their model and one that assumed a uniform gas pressure. In the case of nonuniform gas pressure, liquid flow from cathode to channel leads to a counterflow of gas from channel to cathode and higher capillary pressure and gas transport. Their model predicts as much as a 50 % increase in oxygen transport to the reactive surface, thus intimating the importance of accounting for varying gas pressure. Pasaogullari and Wang proposed that the discontinuity in saturation levels over the CL / MPL interface became so small as to take away the driving force to pull water into the MPL. One drawback of the Pasaogullari and Wang model is that by considering only the half-cell domain, the effect of back diffusion cannot be studied. Water distribution was ascertained based only on the idea that the MPL would wick water away from the cathode CL and neglected the possibility that the MPL would push water back toward the anode.

Weber and Newman examine this possibility by treating the entire PEFC sandwich; however they assume isobaric and isothermal conditions.[196] Through inclusion of the other half of the PEFC, Weber and Newman found that one of the major effects of the MPL is to promote back diffusion and membrane hydration. This is seen in Figure 11, which shows the predicted water pressure and saturation profiles throughout the PEFC sandwich. It is readily apparent that the MPL is acting to pressurize the liquid stream without flooding itself, thereby increasing the back flux of water through the membrane and decreasing the cathode GDL saturation level. Of interest would be what performance difference would have been observed if the gas pressure had not been kept constant. Applying Pasaogullari and Wang's theory of water movement triggering counterflow of the gas phase, the decrease in outward cathode-side water flux induced by including a MPL would also increase oxygen mass-transfer limitations inside the GDL, similar to that seen when nonisothermal phenomena are accounted for (see section 3.2.5). In the model of Weber and Newman, oxygen-transport limitations dominate and dictate the extent that power output can be improved under different conditions and material properties. The main lesson to be gleaned is that for system-level predictions, the perceived limiting mechanism has a large influence on which conditions benefit most from including a MPL and its optimal characteristics.

Increasing MPL thickness has been observed both in experiments and simulations to increase performance up to a critical thickness. After surpassing this critical thickness, the precise value depending on the operating conditions, performance steadily decreases.[190,196] The critical thickness arises mainly due to the trade-offs between increasing the liquid pressure and back flux versus increasing oxygen mass-transport limitations and ohmic drop.[190,196] Essentially, one is trying to minimize the overall saturation in Figure 11 of the composite MPL and GDL structure without significantly increasing the composite's resistance or thickness. Changing the fraction of hydrophilic pores in the MPL so as to balance the advantage of repelling water and keeping PTFE loadings low enough not to compromise electrical contact between the CL and GDL, also demonstrates a maximum at low values.[196] However, performance sensitivity is shown to be low until the MPL became more hydrophilic than the GDL, in which case the MPL begins to flood rapidly with changes in wettability. In terms of providing manufacturing guidance, this means that specifying the exact fraction of hydrophilic pores in not of utmost concern provided that the MPL is more hydrophobic than the GDL.

Karan *et al.*[186] sought to resolve two theories proposed at the time on how MPLs impact water management. The first theory centers on the idea that the MPL wicks away water from the cathode CL while the second claims that the MPL pushes water toward the anode. Note that the former hypothesis originates from half-cell models that could not allow for back-diffusion, and the second from full-cell models. However, upon accounting for variance in PEFC assemblies and measurement errors, they found no statistically significant change in the membrane net water with and without a MPL. Whether this result is general or specific to the operating conditions and MPL properties being examined is unclear. However, while their results seem to favor the first hypothesis of changes in the gas flow, a later full-cell model by Pasaogullari *et al.*[177] based on their half-cell model showed similar results of significant back flux as that of Weber and Newman, especially with a highly hydrophobic and dense MPL. Pasaogullari *et al.* also demonstrate that, the thicker the membrane, the better the performance gain with subsaturated feeds because there is a larger increase in the average membrane water content with a MPL than without one. Overall, the optimal MPL properties are seen to be highly dependent on the coupled physical phenomena in the cell, and so their simulation requires careful consideration of all mechanisms and trade-offs involved. Finally, there is still a need to validate fully the role of a MPL, especially the impact it has on nonisothermal phenomena and vice versa.

3.2.3 Temperature-gradient (heat-pipe) effect

Almost all of the recent models are now nonisothermal. Furthermore, most of them also account not only for heat generation, but also for the existence of temperature gradients. Nonisothermal modeling in this fashion is a change from what had been done earlier, where, due to the thinness of the PEFC sandwich, one assumed that at least the sandwich was at a uniform temperature. However, both experiments and modeling have shown that the low thermal conductivities and overall efficiency of a PEFC can result in temperature gradients through plane. Furthermore, these effects are expected to become larger as the PEFC is more humidified since, if liquid water is produced rather than water vapor, there is much more heat generated at the cathode CL (see equation 7). Finally, water management and thermal management are shown to be strongly coupled phenomena.[197-203]

The equations for treating nonisothermal phenomena are discussed in Section 2, and some of the nonisothermal effects are discussed throughout Section 4. In this section, we want to emphasize the coupling between water and thermal management in GDLs. Unlike the other PEFC layers, GDLs can sustain relatively large temperature gradients due to their relative thickness, and somewhat low thermal conductivity. Besides impacting transport properties, gas concentrations, *etc*., the GDL temperature gradient can create a heat-pipe effect, as shown in Figure 12. In the figure, a temperature gradient induces phase-change and net mass-transfer of water and thermal transfer of heat. Hence, water is evaporated in the cathode CL due to the heat of reaction and moves in the vapor phase down the temperature gradient. The water condenses as it moves along the gradient due to the change in vapor pressure with temperature. Obviously, the heat-pipe effect is more significant at higher temperatures and with larger gradients due to the change in water vapor pressure with temperature; this latter issue also causes much more dilution of reactant gases by water vapor at higher temperatures (see Figure 3(b), for example).

Two of the most extensive modeling studies of this effect are those of Wang and Wang[203] and Weber and Newman[52]. In both, simulations are completed to investigate the heat-pipe effect on both water and thermal movement. Both show that the heat-pipe effect can result in at least 15 % of the total heat transfer in the GDL, while simultaneously providing a means for water movement from the cell in the vapor phase. In fact, it may be that this water-vapor movement is the dominant method to remove water from the cell, and could be a reason why MPLs (which are much more thermally insulating) help in water management.

Wang and Wang show comparisons between nonisothermal cases where the heat-pipe effect and water phase change were and were not considered. The liquid-saturation contours from this comparison are shown in Figure 13. It is apparent that the heat-pipe effect causes a higher liquid condensation amount and hence saturation under the rib (land), which is the coolest part of the domain. This also results in larger liquid-pressure gradients in-plane, with more water moving from the rib to the channel. Not shown is the result that, when water phase change is considered, the temperature profile becomes more uniform and lower throughout the whole 2-D domain.

Weber and Newman use a 1-D model and not a 2-D one, and, similarly to that of Wang and Wang, they demonstrate that the heat-pipe effect can cause a substantial amount of water movement in the vapor instead of liquid phase, thereby causing overall lower liquid saturations in the GDL. Furthermore, the water vapor will move down the temperature gradient, which is opposite the incoming reactant gas flow, thereby resulting in an additional mass-transport limitation in the system. In other words, the temperature and hence water vapor-pressure gradients results in a retardation of the gas flow, which can even cause bulk gas-flow reversal (*i.e.*, convective flow is out of the system) in the anode GDL. Overall, the impact of temperature gradients inside the GDL, especially with saturated feeds, results in significant water-management aspects that should be considered.

3.2.4 Anisotropic properties

Proportionately few PEFC models treat anisotropies due to the paucity of definitive experimental data, additional computational complexity added by solving for extra dimensions, and the difficulty of then incorporating anisotropic values at the risk of losing convergence. The majority of PEFC models have arbitrarily applied in- or through-plane values. However, as more models incorporate higher dimensionalities, inclusion of anisotropies becomes increasingly important, particularly in light of design and limiting-behavior considerations. Strong anisotropies in any direction may completely reroute flow patterns and thereby overhaul the PEFC landscape being modeled. Anisotropies in GDL parameters (*i.e.*, diffusion coefficient, electronic and thermal conductivities, and permeability) are to be expected even if considering only manufacturing effects, *i.e.*, how carbon fibers are pressed to form paper GDLs or woven to form cloth GDLs. Compression effects can further exacerbate permeability anisotropies.[204] For these reasons and because of more efficient computational algorithms and processors, groups are starting to study the effects of property anisotropies on PEFC operation.[205-207] In all cases, in-plane values are typically believed to be larger than through-plane values.

Tomadakis and Sotirchos (TS) developed an expression to determine relative Knudsen diffusivities of fibrous networks that accounts for both in-plane, defined in relation to the main flat surface of the material, and through-plane differences in the material.[207] The effective diffusivity, D_{eff}, is given by

$$D_{\mathrm{eff}} = \varepsilon\left(\frac{\varepsilon-\varepsilon_p}{1-\varepsilon_p}\right)^{\alpha} D_{\mathrm{abs}} \tag{62}$$

where D_{abs} is the absolute molecular diffusivity and the constants ε_p and α are 0.11 and 0.521 and 0.11 and 0.785 for the in- and through-plane directions, respectively.[208] Note that under TS theory, in-plane values will always be greater than through-plane values. For GDLs with porosities greater than 0.2, this is typically the case, with through-plane values about twice those of in-plane ones and approaching them as the porosity increased.[209] Diffusion-coefficient anisotropies are the least extreme of those that are treated.

The in-plane electronic conductivity has also been found to be higher than in the through-plane by up to a factor of 10.[205,210] Electronic conductivity values directly influence current distribution, and incorporating 2-D effects can alter optimum design, e.g., rib-to-channel ratio, because the current-collector width should be minimized to promote oxygen flow while not impeding electron transport.

GDL thermal conductivities are also presumed to be higher in the in-plane direction than the through-plane direction with estimated values ranging from order 1 to 10 W/m-K.[209] Khandelwal and Mench[211] observed a near 50 % asymptotic decrease in through-plane conductivity by increasing PTFE loading from 0 to 20 % for their system, but whether the same magnitude of change or direction of trend would be seen in the in-plane direction is unknown.

As discussed above, temperature and temperature-gradient effects are intricately coupled to water management and PEFC performance.

The final transport parameter to be discussed, permeability, enjoys the distinction of being the most treated in the literature. As discussed in Section 3.2.1, the range of absolute permeabilities is relatively wide in the literature, both from experiment and model fits. In terms of anisotropy, Gostick *et al.*[208] found the in-plane permeability to be up to 2 times greater than through-plane permeability, in general agreement with the literature. However, the spread in measurements is great enough that in-plane and through-plane permeability values could be chosen such that through-plane is greater than in-plane permeability.[206] A counterintuitive consequence of incorporating anisotropies is that inhomogeneities in a medium increases the permeability.[212] While the term "anisotropic system" has typically been used to describe an orthotropic system for which the in-plane values in the along-the-channel and perpendicular-to-channel directions have been the same (x and y in Figure 4), Pharaoh[213] and Williams *et al.*[214] suggest that anisotropy between these values impacts the extent of convective transport in flow under the rib. Pharaoh found that convective flows that traverse serpentine flow channels become significant for through-plane permeabilities greater than $1\times10^{-8}\,\text{cm}^2$. The work portends the need for a 3-D model to capture fully water movement and distribution. As currently published anisotropic models deal primarily with the channel-rib-catalyst-layer plane, subsequent discussion will be duly simplified to this plane. The link between permeabilities and water movement is clear. But again, the net result of anisotropies on water management and performance optimization is quite nebulous, especially when considered in conjunction with previously discussed transport phenomena.

Several methods of tackling the question of what occurs in an anisotropic system have been proposed. One approach is to introduce a resistance at the boundaries of the GDL to compensate for lower through-plane values. This approach has been carried out for solving the cathode-side electron profile and suggested to be of use for elucidating temperature profiles as well because both flow patterns originate from the CL interface and feed into the current collector.[210] However, the approach is more or less empirical in terms of the resistance values to use. The success of this method may also be compromised due to the more complex and coupled movement of liquid and water vapor in the system.

As an initial step toward creating an anisotropic 2-D model, Pharoah *et al.*[205] studied separately the influence of thermal and electronic anisotropies on the current-density distribution in a cathode half-cell model. The results are shown in Figure 14 for the current density along the CL / GDL boundary. For Figure 14(a), the model tested 3 values for D_{eff}, the first found by applying the Bruggeman relation to in-plane permeability, the second by applying the in-plane TS expression, and the third by incorporating anisotropy by using both in- and through-plane values from TS theory. For all scenarios studied, the current density using the isotropic Bruggeman expression was greatest, followed by the anisotropic expression, and lastly the in-plane isotropic expression. The trend is explained by noting two points. First, the Bruggeman expression results in values greater than both values derived from TS theory.[207] Second, the anisotropic case has higher current densities even though the through-plane permeability is less than its isotopic counterpart because nonuniformities in void networks lead to less resistance to movement.[212] A general observation is that, while the magnitude of current density differs for each case, the general shape of the current-distribution curves remain the same as seen in Figure

14(a). The anisotropic and isotropic TS results remain similar under the channel but differ increasingly as one moves under the rib, where diffusion limitations become more severe. The maximum current density shifts toward the rib upon accounting for anisotropy, but the peaks align as the system handles larger loads since oxygen consumption becomes dominant over lateral diffusion for oxygen transport.

Figure 14(b) shows the results of the case when the diffusivity is kept isotropic but the electronic conductivity is either isotropic or anisotropic with a higher value in plane. From the figure, it is clear that not only does the anisotropic case have a higher current density, but it also follows the opposite trend from the isotropic case of having higher current density under the collector than under the channel. The current distribution becomes more strongly dependent on the oxygen distribution as electronic conductivity increases and facilitates movement of electrons toward the collector. Higher in-plane conductivity enables current to spread out more evenly over the rib, thus reducing primary-current effects and increasing efficient use of the collector. It is worth noting that in both the diffusivity and conductivity anisotropy studies, the overall polarization behavior did not change significantly until very high current densities. This shows that the overall polarization often masks local fluctuations and heterogeneities.

Pasaogullari *et al.*[206] input anisotropic values for diffusivity, electronic and thermal conductivity, and permeability simultaneously. Their results also demonstrate a much smaller effect on the global polarization scale than on the local distributions. It is worth noting that for their isotropic case, through-plane values were used everywhere, as opposed to using in-plane values, which is more typical in the literature. Diffusion values were taken from TS theory, electronic and thermal conductivity from experiments—with in-plane values being greater than through-plane values—and permeabilities taken from experiments but with through-plane permeability being an order of magnitude higher than in-plane permeability. Effects of anisotropies in electronic conductivity are similar to those obtained by Pharaoh *et al*. The temperature profiles mirror the potential profiles, which is not too surprising since they have similar boundary conditions and anisotropies.

Of more interest is examining the effect of collective anisotropies on water management. Figure 15. Due to the additional coupling of transport phenomena and treatment of multiphase transport, one sees changes in the liquid pressure and saturation. The impact of the anisotropies leads to a lower overall temperature and smaller temperature gradients, which in turn with the anisotropic permeability causes higher observed levels of saturation and spreading of liquid water over the entirety of the GDL. As noted, the values used by Pasaogullari *et al*. for the isotropic case are smaller than the anisotropic one, and it would be of interest to see how different values (*e.g*., average between the two) changes the impact of the anisotropic properties. In any event, there is a need for further theoretical and experimental studies to determine accurately the effects and values of anisotropic transport properties in the GDL.

3.2.5 Compression

A key difference between the state of a GDL *in* and *ex situ* is the existence of a compressive force applied by the flow fields and PEFC assembly. PEFC components are held together with a compressive load to ensure contact between the layers, but the additional force also affects porosity, pore-size distribution, conductivities, and contact resistances.[197,215-222] Regions under the rib or land are expected to have decreased diffusivities and permeability in the in-plane direction and increased though-plane conductivity due to the vertical compaction of fibers.[219,221] Experimentally, most GDLs exhibit an ideal compression value that balances the benefit from decreasing contact resistance with the penalty of impeding gas and liquid flow.[215,216,220,221] The level of trade-off observed has been seen to be dependent on current density; the greater the current density, the more severe the performance decrease with increasing pressure.[220]

Another interesting consequence of GDL compression is the changing of ratios between through-plane and in-plane transport parameters and subsequent augmentation or diminishment of parameter anisotropies.[204] Several groups found that electrical conductivity increased primarily in the though-plane direction and similar results are postulated for thermal conductivity.[216,221] Because through-plane conductivities are assumed to be smaller than their in-plane counterparts, increases in conductivities due to compression may reduce anisotropies under ribs.[205,209,210] The extent to which compression alters GDL properties is highly dependent upon the GDL material.[216,220] For example, carbon cloth is mechanically less rigid and therefore suffers greater decreases in porosity than does carbon paper.[223] Decreased rigidity of carbon cloth GDLs also implies that they cannot spread pressure from the rib toward the region under the channel as well as carbon paper can, thus leading to distinct flow properties in the medium.

With respect to modeling the compression, cues can be taken from experimental results. Based on their experiments, Ihonen *et al.*[216] and Ge *et al.*[220] conclude that thermal and electrical contact resistances are the main source of impedance and therefore should be incorporated into PEFC models. Although accounting for clamping effects by tuning contact resistances allows for their quick incorporation into fuel-cell models,[197,219] adjusted contact resistances do not account for deformations nor changes to the internal properties of the GDL.

Wu and colleagues have been one of the few groups to treat both changes in contact resistance and deformation effects.[217,218] Based on the observation that the GDL has the lowest compressive modulus of the PEFC components, all deformation was assumed to occur in the GDL.[217,224] GDL porosity was adjusted according to deformation theory[225]

$$\varepsilon = \frac{\varepsilon_o - 1 + e^{\varepsilon_V}}{e^{\varepsilon_V}} \tag{63}$$

where ε_o is the uncompressed porosity and ε_V is the bulk strain. In their models, Wu and coworkers examined flooding and performance on the cathode side of the cell in both crossflow and flow-under-the-rib situations. Figure 16 demonstrates the compression of the GDL and its expansion into the gas channel. In terms of water management, compression effects result in higher liquid saturations and a penetration of the high-saturation front from under the channel towards the rib. The flow-under-the-rib simulations of Wu and coworkers demonstrate a lower saturation when compression is considered. This is opposite to that seen in Figure 16, and begs the question as to the dominant water-movement pathway and the correct modeling geometry. However, even though the saturation is lower upon compression, the current density is lower everywhere as well, as shown in Figure 17. The reason is because the changes in the effective oxygen diffusion coefficient due to compression effects on porosity, *etc*. outweigh the decreased flooding. These results affirm that PEFC performance is dominated primarily by oxygen-transport limitations rather than just by the amount of liquid water. This observation is in agreement with experimental results from Ihonen *et al*. wherein the same value for optimum clamping pressure is obtained for differing humidity conditions.[216]

An additional complexity when modeling water content stems from temperature variations that arise due to compression. In their simulation, Hottinen *et al*.[222] observe higher temperatures under the rib due to a decreased thermal contact resistance with the rib upon compression. Higher temperatures may partially offset the increase saturation levels under the channel and thereby impede the onset of flooding. Alternatively, the preferential formation of water pathways under regions of compression—cause by formation of hydrophilic pathways due to breaking of fibers and PTFE coating—may dominate saturation profiles.[226] To understand fully the underlying mechanisms and physics of how compression changes PEFC performance, there is a need for improved imaging techniques (see Section 1.1) and/or microscopic, mechanical models to account for fluid flow through packed, and possibly broken, fibers.

4 Design Considerations

In most operating cells, even at steady state the same materials must operate over a range of conditions due to nonuniformities in a variety of critical parameters including temperature, current density, reactant concentration, and relative humidity. These nonuniformities arise primarily due to system limitations. For example, isothermal conditions are not achievable in-plane in most applications because a finite coolant flow rate must be used. Similarly, oxygen concentrations change substantially in-plane because low air flow rates are desirable from the perspective of parasitic power and cell humidification. Of course, these two variables are also coupled to one another along with the other parameters listed above.

Such nonuniformities play a critical role in cell power output and durability, largely due to their impact on cell hydration. If a region of the cell is operated with a low relative humidity, ionic conductivity in that region is reduced, and the local current density goes down. Such operation has also been shown to lead to membrane failure.[227] On the other hand, if a region of the cell operates with too much liquid water present, mass transport will be impeded and the local current density will drop. Because it is likely that at least one of these undesirable hydration states will exist somewhere on the cell planform, it is important to be able to predict their effects accurately. In this section, therefore, modeling approaches to low-relative-humidity operation are covered as are modeling techniques for the presence of liquid water in the flow field. In addition, models for common strategies that have been developed for dealing with the potential for nonoptimal cell hydration are reviewed.

4.1 Low-Relative-Humidity Operation

Humidification of reactant streams onboard a power plant can be onerous due to the additional mass (volume), complexity, and cost required. This is especially true on the cathode side where a large amount of inert gas must be humidified along with the oxygen. For these reasons, developers often try minimize or eliminate humidification. As a result, the cell is susceptible to dryout, particularly at the reactant inlets. Predicting the location and magnitude of cell dehydration, as well as the impact on performance, is the subject of this section. As noted, many multidimensional models now allow for the study of unsaturated feeds; example examinations since the last reviews[2,3] are discussed below.

Due to the nonuniformities described above, it is difficult to use either a 1-D through-plane model or a channel/rib 2-D model by itself to predict the effects of low relative humidity operation on overall cell performance. For this reason 1+1-D or 1+2-D models are used to determine the current-density distribution down the channel, assuming low-relative-humidity gas streams at the inlet.

An example of a 1+2-D model of this type is presented by Guvelioglu and Stenger.[228,229] In this case a linear channel/rib combination is divided into control volumes along the length of the channel. For the through-plane direction the model is a 2-D, isothermal, single-phase CFD simulation which takes inlet molar flow rates, cell temperature, and cell voltage, and computes the local cell current density and average reactant concentrations. These concentrations are then used as inlet conditions for the next control volume down the channel. Note that mass transport in the porous media in the direction parallel to the gas channels is neglected. The step size along the channel is set such that the molar flow rates for each component change by less than 2%.

The advantage of the 1+2-D model is its relative simplicity, which translates into reasonably run time. Detailed velocity profiles are not calculated in the channels, and the gas pressure is assumed constant within the gas channels (although through-plane gradients are calculated). This assumption breaks down for cells that have high pressure drop along the gas channel, as is often the case when a serpentine flow geometry is used. Pressure variations affect both relative humidity and velocity profiles significantly.[230]

One way to account for this pressure drop is to approximate it from one control volume to the next based on gas flow rates and the channel geometry. Another is to add a full third dimension. The latter approach is taken by Meng and Wang.[231] Like the 1+2-D model, their approach is to use the assumptions of single-phase flow and an isothermal cell, but the domain considered includes the full cell sandwich as well as multi-pass anode and cathode channels. 3-D velocity profiles are computed within the channels. A critical disadvantage to the full 3-D approach is in processing time; comparing the two cases results in roughly an order of magnitude longer run time for the 3-D case. This is a considerable price to pay considering that the isothermal assumption adds a significant level of uncertainty to the results of either model.

Thermal management and water management are intricately coupled, and one might expect that, for low-relative-humidity-feeds, thermal effects are significant due to the large water phase change. However, Weber and Newman[52] calculate that the cell is typically more isothermal in-plane than nonisothermal for low relative humidity in the gas channels due to evaporation of water in the gas channels leading to a smaller peak temperature. This analysis is the same as taking the overall heat generation (see equation 7) and using the enthalpy potential for the lower heating value instead of the higher one (*i.e.*, water is produced as a vapor).

A key boundary condition that is generally used is that the temperature on the back side of each of the bipolar plates is constant. While the temperatures of the cell materials and gases can vary in three dimensions, they are anchored to isothermal boundary planes. For models with relatively small domains, such as that by Djilali and coworkers[232] (2 cm^2) or Ju *et al.*[200,233,234] (50 cm^2), this simplification is probably justified. On the other hand, most commercial cells are considerably larger. As a result, when full-size cells are modeled using an isothermal backplane assumption, as in Van Zee and coworkers (480 cm^2),[235] the results are questionable because in the real system the coolant temperature typically varies by about 10 °C from inlet to outlet.[236,237]

To address this problem, Wang and Wang[237] have recently extended the model presented in Ju *et al*. to represent a full-size cell (200 cm^2), including coolant flow channels. By doing so only the inlet conditions for the coolant (flow rate and temperature) need to be specified, and the "backplane" temperature is calculated as a function of position. Results from this type of analysis are shown in Figure 18. Temperature profiles for the cell at the membrane-cathode interface are shown in Figure 18 (a) for a cell run at 1.0 A/cm^2 with coolant flow representative of normal operating conditions. The difference between the minimum and the maximum temperature is over 10 °C, illustrating the importance of a nonisothermal backplane when modeling full-size cells. The corresponding membrane water content at the same location is shown in Figure 18(b). Of course, the drawback to this approach is complexity. The authors report that 23.5 million gridpoint calculations are required, resulting in a 20 h run time on 32 parallel computing nodes.

4.2 Liquid Water in Gas Channels

Water in the vapor phase can condense within the reactant channels, just as it can in the porous media. If the condensed water agglomerates it can cause significant changes in pressure drop within the cell (possibly forcing flow to adjacent cells (channels) within a stack (cell)) and can also affect mass transfer of the reactants from the channel to the electrodes. Reactant starvation of this type can cause cell power output to drop or fluctuate and may lead to corrosion under some circumstances.[48,238]

To date, simulations of liquid water within the flow fields have been simplified. This is primarily because of the complicated nature of the physical phenomenon, which is unsteady two-phase flow coupled with the complex physics of PEFC operation, and because most modeling activities have been devoted to the PEFC sandwich. At the same time, a lack of reliable experimental observations has made it difficult to understand the level of detail that is sufficient to describe the physical system. Advances in *in-situ* imaging, however, are rapidly negating the latter point, as discussed in Section 1.1 and shown in Figure 19.

As Figure 19 demonstrates, there are several different liquid-water transport mechanisms that can occur in the flow channels. The dominant one depends on the operating conditions (primarily flowrate, temperature, current density or potential) and surface and material properties of the flow-field plate and the GDL. These mechanisms can be classified as mist or fog flow coupled with GDL water-droplet expulsion and detachment (Figure 19(a)), (annular) film and corner flow along the flow-field plate (Figure 19(b)), and slug flow, where blockage of the channel results (Figure 19(c)). The mechanisms portrayed in Figure 19 can be seen as a progression, where the blockage and slug flow occurs as the film and droplets agglomerate due to liquid-water buildup. In this subsection, first the movement of liquid water in the flow field is discussed with emphasis on recent models, followed by the coupling of water droplets and the GDL / gas-channel interface.

4.2.1 Gas-channel analyses

The most common approach taken in multiphase models is to treat the liquid water in the channel as a species that is dispersed in the gas stream (*i.e.*, mist or fog flow) or as a thin liquid film. Either way, its presence is accounted for using the continuity equation ,but its volume is considered negligible and does not affect gas transport (*i.e.*, the droplets are ignored).[239,240] If the model is nonisothermal, the heat of vaporization is included as a source term in the energy equation.[52,239]

One use for these types of models is as a means of predicting at what point along the channel condensation will begin or end as a function of operating conditions and geometry, in other words, where the wet-to-dry and dry-to-wet transitions occur. An example is the study of Lee and Chu,[241] who use a 3-D, CFD, straight-channel isothermal model to show the effects of cathode relative humidity on the location of the interface between the water in the vapor and liquid phases. Figure 20 contains the results of one such analysis for a cell operating at a fixed voltage of 0.7 V at 70 °C. The anode relative humidity is fixed at 100 % at the cell temperature. The lines on the plot correspond to the predicted location of condensation at different cathode inlet relative humidity values. A similar analysis was completed in 1-D by Yi *et al.*[242] In both of these cases, the effect the liquid water has once it is formed in the channel is not rigorously accounted for, but the probable location for liquid-water formation is estimated.

While neglecting transport effects due to liquid water in the channel may be appropriate as a first approximation (or under some operating conditions), the imaging studies clearly indicate the presence of agglomerated liquid water in the channels.[19-22,25,243] It is highly unlikely that these large droplets have no effect on cell performance. The challenge is that describing the behavior of these droplets rigorously constitutes an unsteady two-phase flow problem that is highly coupled with the operation of the PEFC. While attempts to simulate this phenomenon are discussed in the next section, with regard to the flow field specifically, one of two approaches is taken. Either electrochemical models are used and the presence of water droplets is neglected (as described above), or CFD simulations of droplets in channels are used, and the presence of the rest of the PEFC is largely neglected (*i.e.*, it is just an interface).

Examples of the latter approach are presented by Zhan *et al.*,[244] Jiao *et al.*,[245] and Quan and Lai.[246] In all three cases, 3-D CFD modeling is used assuming isothermal conditions and saturated inlet gases (*i.e.*, no phase change), no gas-phase transport through the channel or GDL walls, and no PEFC reactions. Zhan *et al*. examine the movement of the droplets as a function of the Reynolds, Capillary, and Weber numbers in the channel. They find that straight channels are better than serpentine in discharging water, inertial forces are dominant for gas velocities higher than 4 m/s, and for lower gas velocities, the wettability of the flow-field plate and the GDL determine the ease of water movement; the more hydrophobic the GDL and hydrophilic the plate the better.

Jiao *et al.* use their model to predict the behavior of liquid water as it travels through a stack of 3 cells with serpentine channels. The cells are connected by straight inlet and outlet manifolds. The distribution of liquid water within the system is specified as an initial condition. Gas of constant inlet velocity then flows through the system, and the redistribution of water with time is simulated. Examples of initial conditions include suspended droplets in the inlet manifold or a constant-thickness film on a channel wall. Figure 21 shows results based on the initial condition of a 0.2 mm liquid water film distributed along the leeward side of each gas channel. Each subplot shows the predicted location of the water droplets (shaded) at a different time step. After 0.075 seconds most water has been purged from the system since there is no source for liquid water within the system.

Quan and Lai consider a single U-shaped flow channel. Rather than specifying an initial distribution of water, a constant flux of water through the face representing the GDL is applied as a boundary condition. A constant-inlet-velocity gas flow is applied, and the simulation runs until the water film thickness arrives at a steady state. A comparison is made between a channel with square corners and one with a radius and no corners. The effect of the interior surface contact angle is also investigated.

The value of these types of models is that they provide insight into the dynamics of liquid water as a function of local features and surface properties. For example, Jaio's model predicts that liquid water tends to collect in films in the turns of the serpentine channels and that water leaves these films primarily in the form of small droplets. Quan and Lai's model predicts that whether the liquid water accumulates in a relatively uniform film on the GDL surface or whether it separates and moves along the corners formed by the intersection of the GDL and channel is dependent upon the contact angle of the surfaces. Using these models to predict actual liquid water distribution within a full-size cell, however, cannot be done accurately because the details of energy, momentum, and mass transport into and out of the gas channel through the PEFC sandwich is neglected.

4.2.2 Droplet models and gas-diffusion-layer / gas-channel interface

From the previous section, one can see the importance of accounting for liquid-water flow in the gas channel rigorously, and the need to connect such models of water movement in the gas channel with that of the PEFC sandwich. As noted, in most models this is accomplished by simultaneous mass and energy balances in the channel along with possible pressure drop and gas-flow equations. The inherent assumption is that of mist flow. Although simplistic, this treatment allows for pseudo dimensional or (1+1-D or 1+2-D) models where the 1 is the along-the-channel balances.[52]

The key issue is how to treat the GDL / gas-channel interface. This boundary condition is extremely important since it determines the water management and saturations inside the PEFC sandwich to a significant amount. This boundary condition is typically a specification of flux or concentration for water vapor and one of saturation or liquid pressure for liquid water (see Section 2.6). However, if one is using a two-phase model without a residual effective permeability, then setting saturation equal to zero could be problematic in terms of convergence since this condition enforces the fact that all water must leave the GDL in the vapor phase since the effective permeability will go to zero. We believe that it is better to set the liquid pressure or capillary pressure, and ideally this pressure should be associated with the formation and existence of droplets on the GDL surface. However, such droplets emerge from defined locations, and in the absence of a microstructural GDL model, one is required to assume some kind of average value. Meng and Wang[247] do this in their model by assuming a film on the GDL surface that essentially acts as an interfacial liquid-pressure increase, much like a contact resistance. They demonstrate that higher saturations and lower performance are obtained with such a method, although the value of the film thickness requires empirical fitting.

To understand water droplet behavior, emergence, and detachment, and to provide more physical basis for modeling the interface, detailed droplet-specific studies have been accomplished.[19,243,248,249] These studies focus only on single droplets and are not necessarily valid next to a rib, where the hydrophilic-plate interaction can result in annular and corner flow along the plate (see Figure 19). The four models take the same approach of a force balance for the droplet in the gas channel that is attached to the GDL

$$F_\gamma + F_D = 0 \tag{64}$$

where F_γ is the surface-tension or adhesion force and F_D is the drag force on the droplet. When the drag force is greater than or equal to the surface-tension force, the droplet becomes unstable and detaches from the GDL surface. For these models, fully developed laminar flow in the channel is assumed. For the geometric analysis, it is known that the droplet exhibits a contact-angle hysteresis in that the advancing angle is typically greater than the receding one. In essence, this gives the drop a deformation from a perfect hemisphere or sphere on the GDL surface, and thus the contact-angle hysteresis can be used as an interaction parameter of the droplet with the GDL surface, as discussed below.

All of the models use a similar form for the surface-tension force, which arises from integrating the force around the droplet[243]

$$F_\gamma = \frac{\pi}{2}\gamma c\left[\frac{\sin(\Delta\theta - \theta_A) - \sin(\theta_A)}{\Delta\theta - \pi} + \frac{\sin(\Delta\theta - \theta_A) - \sin(\theta_A)}{\Delta\theta + \pi}\right] \tag{65}$$

where c is the chord length of the contact area between the droplet and GDL surface, γ is the surface tension, $\Delta\theta$ is the contact angle hysteresis, $\Delta\theta = \theta_A - \theta_R$, and θ_A and θ_R are the advancing and receding contact angles, respectively. The models vary slightly in their geometric analysis and trigonometric identities. (He *et al.*[249] assume that the chord length is the same as the mean pore size in the GDL, Zhang *et al.*[19] assume symmetric deviations from the static contact angle, and Chen *et al.*[248] use $r_d \sin(\theta_A)$ for the wetted area, where r_d is the droplet radius).

For the drag force, He *et al.* and Zhang *et al.* both use flow past a sphere

$$F_D = \frac{1}{2} K c_D \rho_G \langle v \rangle^2 A_d \tag{66}$$

where $\langle v \rangle$ is the average velocity in the rectangular channel for laminar flow,[50] A_d is the projected normal area of the droplet to the flow, which is determined from geometric analysis, c_D is the coefficient of drag,

$$F_D = \frac{24}{\mathrm{Re}}\left(1 + 0.1925\,\mathrm{Re}^{0.63}\right) \tag{67}$$

where Re is the Reynolds number

$$\mathrm{Re} = \frac{2\rho_G r_d \langle v \rangle}{\mu_G} \tag{68}$$

In equation 66, Zhang *et al*. use *K* as a fitting function that accounts for the fact that the droplet is not a perfect sphere and also for the assumption of only creeping flow (used for the determination of c_D). He *et al*. integrate the drag force (without *K*) over the actual droplet geometry.

The other two droplet models, those of Kumbur *et al*. and Chen *et al*., adopt a different strategy for the drag force. They assume that the drag force is made up of a pressure force that acts on the droplet itself and a shear force that acts on the top of the droplet. The expression differ slightly due to the assumed geometry, but are of the form[243]

$$F_D = \frac{12\mu_G \langle v \rangle B h_d^2}{\left(B - \frac{h_d}{2}\right)^2 \left(1 - \cos(\theta_A)\right)^2} \left(1 + \frac{2B}{\left(B - \frac{h_d}{2}\right)}\right) \tag{69}$$

where h_d is the droplet height and *B* is the half-width of the channel.

In the above expressions, most of the parameters are known since they are functions of the channel geometry and operating conditions (temperature, flowrate, gas composition, *etc*.). The ones that are not known can be related to the drop morphology on the GDL surface. In turn, these can be related to the contact-angle hysteresis (assuming a deformed hemispherical drop with the given advancing and receding contact angles). There are various ways to examine such a value. Chen *et al*. use the contact-angle hysteresis as the independent variable, and then match stability predictions with experimental findings. He *et al*. assume that the drop behaves with the same form of hysteresis as on Teflon, and they use that function along with the observed static contact angle of water on the GDL. Zhang *et al.* essentially fold the hysteresis into *K*, to get an expression for the droplet diameter in terms of the unknown constant, which is then fit to data. Finally, Kumbur *et al*. perform a linear regression from data for the contact-angle hysteresis, where it is assumed to depend on the channel Reynolds number, and the droplet height and wetted radius or chord. All of the models rely on empirical functions and values for the *a priori* unknown contact-angle hysteresis, with the last one being the most attractive since it is the most physically reasonable and could be used for model predictions.

The use of the force balance and droplet models provides a means to determine droplet-stability diagrams. Two such diagrams are shown in Figure 22. In the figure, the independent variable is chosen to be the aspect ratio of the drop, where larger aspect ratios will correspond to more unstable drops, meaning that a lower channel Reynolds number is required to cause drop detachment. The figure clearly shows that spreading of the drop makes it more stable and thus will cause larger mass-transfer limitations for the reactant gases. The figure also displays the impact of hydrophobicity, with more hydrophobic surfaces lowering the drop stability. From

Figure 22, it can be seen that the force model is slightly overpredicting the stability of the drops. This behavior was investigated by Chen et al.,[248] who compared the simple force model with a complex 2-D CFD one in which all relevant interactions are accounted. They determined that the reason why the force models overpredict stability is due to the neglect of the inertial effects on the droplet by the flow (*i.e.*, it is not purely creeping flow).

While the above droplet models could be used in full-cell simulations (with some assumption or function for the contact-angle hysteresis), the only study so far to attempt this has been that of He *et al*.[249] As noted, they use a form of equation 66 for the drag coefficient and assume that the particles are the same diameters as the mean GDL pore size and the contact-angle hysteresis is similar to that on Teflon with the static values fit to Zhang *et al*.[19] Their droplet model is incorporated into the mass-conservation equations in a 2-D, along-the-channel model. Their results show that low surface tension and hydrophobic surfaces are better overall for water removal. In all, the GDL / gas-channel boundary condition is extremely important and complex. The droplet models are a start, but they need to be coupled with the effects of the ribs and flow-field plates as discussed in Section 4.2.1, as well as detailed PEFC sandwich models.

4.3 Water-Management Strategies

Various cell-design strategies have been developed to enhance water management. Each of these has in common the goal of providing optimal cell hydration to as large a fraction of the cell area as possible. Optimal cell hydration occurs when the membrane conductivity is maximized with concurrent reactant-transport-loss minimization. Several of the most common strategies are discussed below, with a focus on the models that have been developed to predict their effects.

4.3.1 Gas-flow direction

One method for optimizing cell hydration is to manipulate the orientation of the flow of the reactants and coolant relative to one another. A simple example would be to coflow the cathode gas stream and the coolant. By doing so, the amount of cathode inlet dryout is likely to be reduced relative to a counterflow arrangement due to the lower local cell temperature.[236,237] Of course, at the stack level this approach has the disadvantage that the cathode air leaves the cell with a higher water content, making water balance more of a challenge, and so a trade-off must be made between the durability and performance of the cell and the size and complexity of the system.

Numerous models for cell hydration as a function of fluid-flow orientation have been developed, where it should be noted that counterflow is much harder to simulate than coflow since it requires an extra external iteration loop (*i.e.*, it is a boundary-value instead of an initial-value problem). For this reason, most simulations, especially the 3-D ones, assume coflow. Most of the low-orientation studies focus on reactant flows, assuming either a constant coolant temperature or a predefined temperature gradient. An example is the model by Wilkinson and St-Pierre,[250] which is 1-D (down the channel), assumes a uniform current distribution, a linear temperature gradient, and does not account for reactant pressure drop or net water flow through the PEFC sandwich. These simplifications enable a rapid first approximation of reactant relative humidity and concentration as a function of position along the channel for different reactant flow orientations relative to one another as well as relative to the coolant-flow direction. This approach is extended to 1+1D by Berg *et al.*,[251] who retain the assumption of a prescribed temperature gradient down the channel while improving accuracy by calculating water transport through the membrane and membrane conductivity. These models demonstrate that counterflow results in more uniform hydration profiles than coflow with low-relative-humidity feeds. Finally, due to manifolding issues, the most appropriate type of reactant-gas flow is probably crossflow. This situation was looked at by Weber and Newman,[78] through the use of a 1-D model that is run in a 2-D array of node points, where each point was connected to each other through simultaneous mass and energy balances. They found that crossflow increases the average humidity and provides around a 30% increase in current density for 25 % relative-humidity feeds than the coflow case.

CFD models have also been used to study relative flow orientation effects, although most have been isothermal, which limits their applicability towards full-size cells.[252-254] While use of a nonisothermal model can improve the simulation accuracy, the complexity of fully-nonisothermal, 3-D, CFD models limits the usefulness of these models for rapid-design iteration.[237] A simplified approach is presented by Büchi and coworkers.[107,236] Here, a detailed nonisothermal 1-D through-plane model, which includes heat transfer to coolant channels as well as multiphase flow effects, is coupled via a 2+1D network. This approach utilizes a plug flow assumption in the channels; detailed velocity profiles are not computed. However, both the through-plane and in-plane temperature gradients are computed for full-size cells with a fraction of the complexity and computational cost of a full CFD model. Figure 23 shows a comparison of the current density profile predicted and measured in a 200 cm^2 cell as a function of reactant-flow orientation. The triangular symbol containing a "T" in each plot represents the temperature gradient imposed on the cell by the coolant. Comparing plots a and b to plots b and c shows that the effect of the coolant temperature gradient is at least as important as that of reactant-flow orientation.

4.3.2 Interdigitated flow fields

One strategy that is used in an attempt to reduce mass-transport limitations due to water buildup is that of interdigitated flow fields (IDFF).[255-257] In this design, the reactant flow channels are not continuous, and there is flow through the GDL from one channel to the other. The intent is to force reactant transport to the electrode by convection rather than diffusion and to use momentum transfer to reduce liquid water accumulation in the GDLs. Cells with interdigitated flow fields often do show higher performance at higher current densities (*i.e.*, in the mass-transfer-limited regime). However, this gain comes at the expense of higher reactant pressure drop. As a result, either the parasitic power required for driving the flow increases or the flow channel depth must increase. Whether a net increase in system power density can be expected, therefore, depends on the amount of performance gained per square centimeter relative to the amount of additional pressure drop.

A number of models have been developed to simulate the effect of IDFFs. These have been used in two ways. First, some have been developed to investigate whether this approach truly lowers mass-transport limitations in the manner described above. Second, some are intended as design tools that can be used in the performance-versus-pressure-drop tradeoff study. Before examining IDFF models, it should be mentioned that in-plane convection through the GDL may occur between adjacent channels in cells where an IDFF is not used. This is most likely to occur between adjacent legs of a serpentine flow channel due to the high pressure drop per unit length that this geometry normally imposes, especially if there is blockage of the bend due to water droplets. Models have been developed to study the relative importance of convection and diffusion as a function of channel geometry (such as rib-to-channel width ratio) and GDL properties. These range in complexity from the simplified but fully-analytical approach presented by Advani and coworkers[258] to the 3-D CFD numerical simulation presented by Park and Li.[259] Both approaches show that cross-leakage is a strong function of GDL permeability; for typical values of permeability (ca. 10^{-12} m^2) they predict that the fraction of "cross-leakage" through the GDL will generally be less than 5 % (assuming no blockage of the gas channel).

When IDFF is used on all or part of the cell, 100 % of the flow will be through the GDL where the IDFF channels end. Models describing this phenomenon can be divided into two categories. The first is full CFD models[260-263] in which all terms in the Navier Stokes equations are accounted for and the full cell sandwich is simulated. Models in the second category[256,257,264-269] simplify the momentum equation to Darcy's law and restrict the simulated domain to only part of the full cell sandwich, usually the cathode GDL. Some of the earliest models of IDFFs, those of Nguyen and coworkers[256,257] and Kazim *et al.*[270] demonstrated the importance of having more gas channels with smaller widths, among other things. An early full 3-D approach for IDFFs was developed by Wang and Liu.[260] In this case the full cell sandwich is considered in with coflow in straight reactant channels. For a given side of the cell, the exit of the channel that the reactant gas enters is impermeable (blocked), while the entrance of the adjacent cell is impermeable and the exit is permeable (open). As a result, the gas must flow through the GDL. The model is nonisothermal, although the condensation of water vapor is not considered in the energy equation. Yan *et al.*[261] extend this approach to include multiple sets of

IDFF channels and to compare different *x-y* plane channel flow patterns (*e.g.,* the Z-type flow pattern). The planform considered, however, is still quite small (5 cm^2).

A feature of the CFD models is that they estimate both the pressure drop associated with IDFF as well as the performance impact with one set of equations once the geometry is defined. The disadvantage is computational complexity and run time. In the second category of models, simplifications are made in order to reduce the computational load. An example is presented by Yamada *et al.,*[264] where a 2-D channel/rib model is used, considering the GDL only. In addition, Darcy's law, instead of the full Navier-Stokes equation is used to describe the gas flow. The model is isothermal, but, unlike any of the CFD models, the presence of liquid water is explicitly accounted for. Water is allowed to condense in locations where the activity of water is greater than unity, and local liquid water saturation is calculated. Saturation, in turn, affects both gas permeability and gas diffusion coefficients. A similar isothermal 2-D model is presented by Zou *et al,.*[265] although a single-phase assumption is used. Unlike all of the other models reviewed in this section, however, this is a transient model. While these models can calculate cell performance as a function of the specific IDFF geometry, they do not calculate the overall pressure drop (that of the channels plus the substrate), which is also important.

To include the pressure drop, one approach is to calculate performance using a simplified model similar to those described above and to predict pressure drop separately. An example is presented by Arato and Costa[266] (performance model) and Arato *et al.*[267] (pressure-drop model). In the pressure-drop model, the system is simplified to two dimensions, *x* and *y*. Two adjacent IDFF channels are defined such that the long dimensions align with the *x* direction. The migration velocity from channel 1 to channel 2 is defined by the variable *v*, which is a function of *x* only. The gas pressures in each channel, P_1 and P_2, are also functions of x only. The migration velocity is then given by a simplified version of Darcy's law,

$$v = \frac{f_1 k(P_1 - P_2)}{\mu d} \tag{70}$$

where f_1 is a shape factor. The gas-phase pressure and velocity for channel *j* is given by

$$\frac{dP_j}{dZ} = -\frac{f_2 32 u_j \mu}{(2B)^2} \tag{71}$$

$$\frac{du_j}{dZ} = -\frac{f_3 v h}{(2B)^2} \tag{72}$$

where f_2 and f_3 are shape factors, *h* is the thickness of the GDL, and *b* is the width of the gas channel. By solving the above three equations, the gas-phase velocity, migration velocity, and pressure as a function of channel position are obtained.

An alternate approach for the pressure-drop calculation is presented by Inoue and coworkers.[268] A detailed 2-D channel/rib model of the GDL only is used to calculate oxygen concentration and cell performance based on Darcy flow. However, this model is then integrated with a 2-D in-plane thermal model and a plug-flow, 1-D channel model which provides boundary conditions for the GDL model. A single-phase approximation is used, and diffusion and heat conduction are neglected in the flow channel. Using this approach, complex flow geometries on the scale of a full-size cell can be simulated.

While the Arato and Inoue approaches are simplified relative to the full CFD models, they offer a design tool to estimate rapidly whether or not IDFF may offer a significant power density advantage and to approximate the impact of different channel-geometry parameters, such as rib-to-channel ratio.

4.3.3 Water-transport plates

Nonuniformities in cell hydration arise either because there is no source for water in a given location or because there is no sink for excess water. Often these conditions coexist on the same cell planform, at the cathode inlets and exits, respectively. A strategy that has been developed to counter this effect is to provide simultaneously a source and a sink for water by using a hydrophilic porous bipolar plate (called a water-transport plate, or WTP), which is filled with water and is maintained at a liquid pressure that is lower than the gas pressure.[242,271] By doing so, the reactants can be internally humidified throughout the entire planform, thereby minimizing dry regions, while at the same time excess water can be removed in the liquid phase through the WTP, thereby minimizing flooded regions.

A detailed analysis of the WTP system is presented by Weber and Darling.[272] Here the 1+1D, multiphase, nonisothermal model developed by the authors to describe solid-plate cells[52] is adapted to porous bipolar plates. Properties of all of the layers in the PEFC sandwich are identical to the solid-plate case with the exception of the plates themselves. Governing equations for the plates include Darcy's law and an energy balance. Boundary conditions at the back side of the WTP are the coolant pressure and temperature. Excess coolant flow is assumed, so that the surface in contact with the coolant is assumed to be at the coolant inlet temperature all along the length of the channel. The model is used to compare WTP and solid-plate performance under low-relative-humidity conditions as well as to explore the performance of the WTP as a function of various parameters, such as gas-to-liquid pressure difference, GDL wettability, and WTP properties. The idea of having a passive or low-power active liquid-water-management strategy similar to WTPs has been investigated with such applications as direct liquid water injection (which is also discussed in the next section),[273] wicking of liquid water through adsorbent wicks or sponges in the flow field,[274-276] and electroosmotic pumps within the cell.[277] However, those applications have not been modeled extensively. In addition, as discussed in section 3.2.3, advanced GDL designs and the use of MPLs can be used to mitigate water-management concerns.

4.3.4 Alternate cooling approaches

For many applications, liquid or forced-air cooling utilizing dedicated coolant flow channels is the predominant approach to thermal management. Alternatives include evaporative cooling and passive cooling. In evaporative cooling, liquid water is injected into the PEFC, changes phase due to the heat production within the cell, and exits the cell in the vapor phase. Because the heat of vaporization for water is so high, the total liquid flow rate is very small compared with that for conventional cooling. For example, using pure water, to achieve 1 kW of cooling using a 10 °C ΔT requires roughly 24 g/s of coolant flow. With evaporative cooling the flow rate drops to 0.43 g/s, or 55 times less. As a result of the very small flow rates required, the liquid can either be sprayed into the reactant inlet(s) as a fog or it can be distributed via fine channels or a WTP. The advantage of the former approach is that it can eliminate one of the bipolar plates. The advantage of the latter is greater uniformity across the planform. Modeling of evaporatively cooled cells is limited to date. A systems-level view relating the required stack air exit temperature to the operating pressure is presented by Meyers *et al.*[278]

Passively cooled cells rely on natural convection to provide both fresh oxidant to the cathode as well as cell cooling. Passive cooling generally is limited to single-cell applications such as portable power. To model these devices, the coupled effects of heat and mass transfer must be considered. An example is the model presented by Djilali and coworkers,[279] in which a steady-state 2-D CFD analysis is used to predict oxygen concentration and temperature as a function of position within the cell. Heat transfer is assumed to occur by natural convection only. A similar approach is taken by Hwang and coworkers[280] and by Litster and Djilali,[281] although in the latter case the solution was obtained through a semi-analytical technique rather than CFD. Common to each of these models, however, are the following assumptions which greatly limit their applicability and accuracy. First, there is no net water transport through the membrane and the conductivity of the membrane does not depend on water content. In addition, water is formed and exists only in the vapor phase.

5 Transient Operation and Load Changes

Although some (stationary) applications for PEFCs require a relatively constant power output (providing base-load electricity for a building, for example), many target applications, including materials handling, back-up power generation, and transportation, require frequent load changes and transient operation. Several processes affect cell performance during these transients. Of primary importance are the changes in temperature profile, cell hydration, and reactant availability. The amount of waste heat generated by the cell, given by equation 7, will change during the transient. This means that the temperature profile within the cell will change as the cell finds a new steady-state temperature to drive the removal of the waste heat. The steady-state hydration profile will also change, which can result in water within the cell changing phase, leading to two-phase-flow effects in either the PEFC sandwich or the channels. Reactant availability can be an issue if the time constant for transport of hydrogen or oxygen to the catalyst surface is on the same order as the transient time or if a dramatic increase in mass transport resistance occurs due to the presence of liquid water films or droplets.

Since our last review in 2004,[2] there has been a larger focus on simulating transient operation. This section discusses the more recent models for transient operation above 0°C, and Section 6.2 discusses those models for transient operation below 0°C (*i.e.*, where freezing affects water management). The models presented in this section are categorized based on their thermal- and water-management strategies (*i.e.*, single-phase or two-phase flow for water and isothermal and nonisothermal, respectively). Before discussing the details of individual models, it is important to contemplate the timescales of the processes involved in a load transient. By doing so, the reader will be in a better position to evaluate the importance of inclusion of each process and therefore the validity of the assumptions made in the models covered below.

5.1 Relative Timescales

To judge whether or not a process may be rate limiting, it is necessary first of all to understand the desired maximum time for a transient. This will vary with the application. As an example, one can consider automotive targets as put forward by the Department of Energy.[282] These targets specify a time of 1 second or less for a step change from 10 % to 90 % of rated power.

A summary of time scales for the different fuel-cell processes is presented in Table 1, which is a modified version of a similar table in Mueller *et al.*[283] The table is arranged in order of ascending time constant. From this analysis, one can see that the charging and discharging of the double layer and the electrochemical reaction rate are very fast relative to other transients. For this reason they can be neglected without concern (*i.e.*, assume pseudo steady-state for them). On the other hand, species diffusion, membrane equilibration, and heat transfer all occur on time scales that are relevant to the 1 second automotive requirement. An accurate model for this application, therefore, would consider each of these processes. It is also worth noting that, according to this analysis, it will take 10's of seconds for the cell to equilibrate completely after a transient has occurred, which is in disagreement with some findings that water rearrangement in the GDL can be on the order of minutes and tens of minutes.[18,181,284,285]

5.2 Single-Phase-Flow Models

As discussed throughout this article, the use of single-phase models is appropriate only if one is dealing with situations where water is not expected to condense. While the neglect of two-phase-flow effects changes the overall water-management results, it does provide for a simpler model and one that is much easier to run for transient conditions. Such models tend to rely heavily on empirical inputs, such as polarization-curve fits, and generally are useful for power-plant-level controls development but have limited utility in the cell design process.

5.2.1 Isothermal

The simplest approach to modeling transient behavior is with a 0-D, lumped model in which the cell properties and operational parameters are considered to be independent of position. An example is the model of Haddad and coworkers,[286] which attempted to incorporate hydration effects into a 0-D model. In this case, the conductivity of the membrane was made an explicit function of the reactant humidification. Using this relationship, the change in cell voltage due to fluctuating ionic resistance is predicted. Note that the relationship used in this case is purely empirical and assumes instantaneous equilibration of the membrane with the reactant humidification level. In addition, no distinction is made between anode and cathode humidification.

Considering the effects of membrane hydration more rigorously requires computing membrane water content as a function of position, as by Friede *et al.*[287] and Yu and Ziegler.[288] In their models, λ values are computed as a function of the z-coordinate, and membrane conductivity, water diffusivity, and the electroosmotic coefficient are all modeled as direct functions of $\lambda(z)$. This enables explicit treatment of differences in water content between anode and cathode (due to reactant humidity, product water, *etc*.). Chen *et al.*[289,290] use a similar approach, but also account for membrane swelling as a function of λ. Vorobev *et al.*[290] account for the time required for equilibrium to be reached between liquid water in the membrane phase in the CLs and the surrounding vapor-phase water. Finally, the model of Nazarof and Promislow[291] examines the ignition and extinction behavior of a PEFC system with well mixed gas channels.[292] Their analysis agrees with experimental data showing that a minimum membrane water content is necessary for ignition behavior during PEFC startup. This value depends mainly on the feedback between proton conduction and water production.

The 0-D and 1-D models discussed so far can be used to model the effects of membrane conductivity on performance during a transient. However, to predict reactant-transport effects accurately, it is usually necessary to model in more than one dimension due to the fact that neither current density nor reactant concentrations are uniform throughout the cell. As a result, it can be difficult to predict the appropriate boundary conditions for a 1-D model. Along-the-channel models represent one means of addressing this issue. An example is the 2-D model presented by Rao and Rengaswamy.[293] In this case, the domain consists of the membrane, cathode CL, GDL, and gas channel. Average current density or cell voltage is provided as an input while the oxygen-partial-pressure profile as a function of time and position down the channel is the primary output. An alternate approach is presented by Yan *et al.*,[294] who formulated a 2-D model to look at the current-density and oxygen-concentration profiles under the channel and rib rather than down the channel. As with Rao, the model considers only the membrane and cathode.

Simplified 2-D models, such as those described above, provide tools with which to evaluate both system-design parameters, such as optimal reactant-feed stoichiometry during a transient, and cell-design parameters, such as acceptable rib-to-channel ratios. 3-D models combine these two domains (along-the-channel and under-the-rib) to provide a unified solution to the transient problem. The 3-D model of Van Zee and coworkers[193,295] is an example. Here the domain considered contains both anode and cathode flow channels and ribs, GDLs, and the membrane and CLs are considered to be one layer. The flow channels are oriented in a serpentine fashion, with a total of 20 passes. Membrane hydration is explicitly considered, meaning that the effects of reactant relative humidity can be investigated. Using this model, the oxygen-concentration and current-density profiles at the CL-membrane-CL surface can be observed as a function of time.

Wang and Wang[296,297] also developed a 3-D, isothermal, transient model. Although the domain considered is a straight channel as opposed to serpentine, the PEFC sandwich is resolved into its constituent layers, providing an additional level of resolution. Results from a sample simulation are provided in Figure 24. In this case, a step change in current is applied, and the cell-voltage response is simulated. The operating temperature is 80°C, and the inlet relative humidity of the anode and cathode gases is set to be 50 % and 0 %, respectively, at the cell operating temperature. In the figure, four cases are shown, with each one corresponding to a larger step change in current density. The larger the step change, the greater the "undershoot" in cell voltage—that is, the voltage minimum relative to the steady-state value. Undershoot in this case is caused by temporary anode-side dehydration. When the current changes, the increased electroosmotic flux tends to dry out the anode while the increased water production tends to increase cathode hydration. The undershoot represents the time required for the excess cathode water to back-diffuse, rehydrating the anode and decreasing anode-side ionic resistance. In the most extreme case, for a step change from 0.1 to 0.7 A/cm^2, the increase in resistance is so high that the current cannot be supported and the cell voltage drops to zero.

5.2.2 Nonisothermal

An early example of a single-phase, nonisothermal, transient model is that of Amphlett *et al.*[298] Their approach is to couple a 0-D, steady-state, cell-performance model with a transient thermal model. The steady-state performance model is based on an semi-empirical formulation and simplifies to

$$V = V\left(i, T\right) \tag{73}$$

where T is the lumped stack temperature. Fitting parameters based on experimental data are used to determine V. The transient thermal model is

$$\frac{dT}{dt} = \frac{1}{m_{stack}\hat{C}_P^{stack}}\left(Q - Q_{sens} - Q_{loss}\right) \tag{74}$$

where the energies on the right side of the equation, from left to right, correspond to the theoretical heat production (see equation 7), the heat transferred to the coolant and reactants (including the heat of vaporization of water), and the heat lost to the environment from the surface of the stack. Each of these terms are included in expanded form in equation 20 with the exception of the last one, which is simply the difference between the lumped stack temperature and the ambient temperature multiplied by a heat transfer coefficient and an effective surface area. By using this model, the authors demonstrate good agreement with stack data. However, the timescale of the transients considered is on the order of minutes, which is roughly the time required to change the bulk temperature of the stack by tens of degrees.

For a higher-frequency load profile, where the current density oscillates rapidly while the stack temperature changes very little, the voltage response caused by rapid changes in hydration will not be captured by this type of model. For example, Chen *et al.*[299] modeled membrane hydration in 1-D during a transient (considering electroosmotic flow and diffusion effects) and found that the time to reach steady state varied between 1 and 10 seconds depending on the magnitude of the change in current density.

Shan and Choe[199,300] present a nonisothermal 1-D model that addresses this issue. In their system, the PEFC sandwich is considered, and membrane hydration effects are included. Reactant transport from the channels to the CL is by diffusion only. An energy balance is completed with respect to each control volume as follows:

$$\sum_i C_{p_i} c_i A_c l_{CV} = \sum \dot{m}_{in} A_c C_{p_j} (T_{in} - T_{CV}) + Q_{conv} A_c + Q_{cond} A_c + Q_{res} A_c + Q A_c \tag{75}$$

where the terms on the right are for mass flow in, convective heat transfer, conductive heat transfer, heat production due to ohmic losses, and heat production due to the fuel cell reaction (as given by equation 7), respectively. This 1-D cell model is further integrated into a stack level.[52] The 1-D cell stack consists of cells divided by cooling layers (in a 1-to-1 ratio), with this layered entire layered structure bounded on either side by the layers that represent stack end structure. An energy balance is performed, allowing the temperature profile within a given cell as well as throughout the stack to be modeled during a transient.

Multidimensional nonisothermal transient models are also present in the literature. In 2-D, both the down-the-channel case as well as under-the-rib case[301] have been considered. An example of the down-the-channel case is the approach taken by Huang *et al.*[230] In this case, the cell temperature in the *z*-direction is considered constant, but the temperature is allowed to vary along the channel, in a similar approach to that of Fuller and Newman.[302] In this way, the effect of temperature on the current-density distribution and reactant concentrations can be approximated without the added complexity of computing the through-plane thermal profile. Given the fact that the down-the-channel temperature variation is generally large relative to the through-plane variation,[203,236,272] this is often a reasonable approximation. The model also incorporates pressure-drop effects in the channels (neglecting entrance and exit effects) as well as pressure-driven water flow through the membrane via Darcy's law, enabling analysis of the effect of running the anode and cathode at different pressures.

Despite the fact that the reactant pressure and velocity are not constant down the channel in the model of Huang *et al.*, detailed fluid dynamics is neglected. That is, fully-developed laminar flow is assumed, and the *average* gas velocity is computed parallel to the channel only, while reactant convection is neglected in the through-plane direction. In contrast, CFD methods can be used to solve the Navier-Stokes equations and predict the velocity field within the channel, as shown in the 2-D, transient, nonisothermal model by Shan *et al.*[303]

To model temperature, reactant-concentration, and current-density profiles during a transient at the full-cell level, 3-D analysis is often required, especially when the reactant gases and/or coolant make multiple passes across the cell planform. Naturally, completing transient calculations with a full 3-D model can be computationally intensive, and methods of simplification with minimal loss in accuracy are desirable. One approach is to use a 2+1D approach in which species transport is modeled in detail in the through-plane direction, while in-plane the only reactant flow is in the gas channels. This is the technique used by Mueller *et al.*[283] They divide the cell into eight control volumes in the through-plane direction: a coolant channel, anode and cathode solid plates, anode and cathode gas channels, anode and cathode GDLs, and an MEA. Each control volume is characterized by a single lumped temperature, pressure, and set of species mole fractions. In-plane, the cell is discretized into 35 nodes arranged in a grid pattern. This model exhibits good agreement with experimental data for both steady-state and transient, as shown in Figure 25, operation. The figure again shows the dip in potential as seen in Figure 24; however, the transient response is now much longer than in that figure and matches experimental data. The long transient demonstrates the importance of thermal management and nonisothermal effects on transient operation.

5.2 Two-Phase-Flow Models

All of the transient models listed above have neglected the presence of liquid water outside the membrane phase. As discussed throughout this article, this is valid only for some regions of the cell where the activity of water is typically less than one (*e.g.*, at the reactant inlets) or for modeling low-relative-humidity operation. For other conditions, one must consider flow in both the liquid and vapor phases. Furthermore, it is often seen that the rearrangement of liquid water and development of the saturation profiles are the longest time constants in the system.[181,285,304] While this is known, transient modeling with two-phase flow becomes very complicated, and there are only a few such models currently.

To consider two-phase-flow effects in a relatively simple manner for transient operation, one could assume that the cell is at a uniform temperature, thereby eliminating the need to have a varying water vapor pressure and computing the complete energy balance. Ziegler *et al.*[305] present a cathode-side, 1-D model of this type, with the primary application to the study of potential-sweep experiments to understand the potential-current hysteresis in terms of water content changes in the membrane. To calculate two-phase flow, they use the methods described previously with cubic dependence of the permeability on saturation and a GDL model similar to that of Weber *et al.*[85] A similar model to that of Ziegler *et al.*, is the one by Chang and Chu,[306] who use an embedded-agglomerate model with a film in the cathode CL instead of only a porous-electrode model. This analysis allowed them to examine in detail the dynamics of water movement, with a focus on the CL and GDL porosities, showing how the approach to steady state (dip in Figure 20) depends on porosity, with high porosities exhibiting an increase and not a decrease.

A final layer of complexity can be added to the transient models by considering not only multiple phases but also the strongly coupled temperature distribution. This is done by adding the energy equation to the models described above. In Section 5.1.2, a similar approach was used to make single-phase models nonisothermal. However, in this case the energy equation must contain a source term for the heat of vaporization to account for energy transferred by the phase change of water.

One-dimensional models of this type have been presented by Song *et al.*[307] as well as Shah *et al.*[192] The former considers only the cathode GDL while the latter consider the full cell sandwich, including optional microporous layers. These models offer cell designers powerful tools to evaluate the effect of material properties such as porosity, gas and liquid permeability, and contact angle on transient performance. As with single-phase models, however, evaluating reactant-distribution effects most often requires modeling in more than one dimension. This is all the more true in the nonisothermal case because the temperature can vary significantly across the planform.

One approach is to use a 3-D CFD model as by Guilin and Jianren[308] and Van Zee and coworkers.[309] In both of these cases the full-cell sandwich is resolved through-plane, and in-plane a serpentine flow geometry is considered. In the channels and GDLs, homogeneous two-phase flow is assumed, meaning that liquid water is assumed to be dispersed within the gas phase and to move at the local gas velocity. This stands in contrast to the 1-D models discussed above, where liquid water is assumed to condense on the surfaces of pores and to move under the influence of a capillary-pressure gradient. To account for the effect of the presence of liquid water on reactant gas transport, Guilin and Jianren use an effective diffusivity, which simply multiplies the diffusion coefficient for a gas species by the gas-phase saturation. Van Zee and coworkers do not use this type of correction; instead they employ a liquid-film resistance on top of the platinum particles in the CL. In Guilin and Jianren's model, the membrane conductivity is not computed as a function of position; instantaneous equilibration is assumed between membrane water content and the gas phase. For this reason the effects of transients on membrane hydration are highly simplified. Van Zee's model does account for local, time-dependent membrane conductivity.

Oxygen mole fraction as a function of position and time during a transient, as predicted by Van Zee's analysis, is shown in Figure 26. The x-axis position corresponds to a cross-section of the serpentine cell which is normal to the predominant flow direction of the channels (*i.e.*, it cuts through the channels and ribs). This is the reason for the oscillations as a function of x: the low points correspond to under-the-channel locations while the high points correspond to under-the-rib locations. The higher the value of x, the closer the position is to the exit of the channel. Figure 27 shows values of average cell current density and cell voltage during this transient. For comparison, the current density prediction is also shown for the same voltage transient using the isothermal, single-phase model described in reference 39, highlighting the importance of accounting for temperature effects.

6 Freeze

Hydrogen fuel cells produce water in addition to electricity and heat, and most proton-exchange-membrane materials require hydration in order to conduct ions. As a result, cold-weather operation of these devices presents unique challenges for their water and thermal management. Residual water in the various PEFC porous media might freeze during shutdown, inhibiting proper functionality on restart while possibly causing irreversible damage. In addition, during the cold-start process, the primary mode of product water removal – that is, in the vapor phase – is unavailable due to the low vapor pressure of water at low temperatures. As a result, if the cell does not heat up fast enough, flooding of the GDLs and CLs will occur, and the PEFC will be unable to continue operating without external heat input.

For automotive applications, several targets relating to cold start have been set by the Department of Energy.[282] First, the PEFC must be able to start unassisted from −40°C. Second, it must be able to start from −20°C to 50 % net power within 30 s. Third, the total amount of energy expended during the start-up *and* shutdown cannot exceed 5 MJ. No requirement is stated by the DOE for the number of freeze start cycles. However, a report by Pesaran *et al.*[310] at NREL did use historical weather records to estimate how often a PEFC vehicle operated in the U.S. may experience freezing temperatures, concluding that on average between 1961 and 1988, 43 states experienced −20°C at least once per year, while 25 states recorded −20°C over 40 times per year. The expected lifetime of a PEFC system inside a vehicle is 10 years.

One common approach to enable cold start is to dry the PEFC prior to allowing it to freeze, thereby minimizing the risk of damage by ice formation and maximizing the amount of volume available within the porous media to absorb product water on restart. However, while this approach may result in improved start performance, it has significant drawbacks. First, the purge requires energy and time to complete. Second, it reduces the ionic conductivity of the membrane, lowering the amount of power initially available on restart. Third, it exposes the membrane to the stress of a relative-humidity cycle, which can lead to membrane failure.[311]

To develop new materials and methodologies that will enable cold start while addressing the issues listed above, modeling is required. However, this subject remains one of the least-explored areas of water modeling in the literature. A number of papers have dealt with stack-level temperature response during shutdown and start-up, but only a handful have attempted modeling water within the PEFC sandwich under these conditions.

6.1 Shutdown and Freezing

Once the PEFC stack stops operating, its temperature will gradually decay until it reaches ambient temperature, assuming the stack is not restarted. If the ambient temperature is below 0°C, liquid water present in the PEFC porous media may freeze depending on the pore wettability. In addition, the thermal gradient that is imposed on the cell during the cool down and freeze can in fact result in the movement of significant amounts of water from one part of the cell to another, first in the vapor phase (above 0°C), and then in the liquid phase (below 0°C).

Water that has redistributed can then freeze in locations that inhibit proper cell functionality on restart. Understanding the parameters that control this water redistribution, such as the shutdown procedure and the material properties, is critical if system designers are to be able to incorporate mitigation strategies. The mechanisms for the movement of water and the existing models are discussed in this section.

6.1.1 Stack-level models

As stated above, it is the presence of thermal gradients within the PEFC sandwich during cooling that result in the redistribution of water. The origin of these thermal gradients comes from the fact that, in most applications, cells are arranged into stacks with lengthscales typically on the order of tens of centimeters. As a result, when a warm stack which is no longer generating heat is exposed to a cool environment, cooling occurs from the outside in. For example, considering only the z-direction, this means that the cells at the end of the stack cool first while the middle cells cool last. As a result, a given cell will experience a change in temperature in the z-direction during the cooling process.

To understand the magnitude of the thermal gradients, stack-level thermal models are generally used. The simplest of these is a 0-D lumped-cell stack model, as presented by Pesaran and coworkers.[310] Here the entire cell stack is considered to be a homogeneous mass thermally connected to the environment through a heat-transfer coefficient, h_{stack}. The total cool-down time, t_{cd}, required for the stack to move from the initial temperature, T_0 to a target temperature T_t, with an environmental temperature of T_{ext}, is given by

$$t_{cd} = \frac{m_{stack} C_P^{stack}}{A_{stack}} \left(\frac{1}{h_{stack}} + \frac{l_{ins}}{k_{ins}} \right) \ln \left(\frac{T_0 - T_{ext}}{T_t - T_{ext}} \right) \tag{76}$$

where C_P^{stack} is the heat capacity of the stack, and A_{stack} is the surface area. The parameter k_{ins} in this case is the thermal conductivity of any insulation used to keep the stack warm. If there is no insulation present, $k_{ins} \to \infty$.

The lumped stack model gives a first approximation for the cool-down time, and provides a simple framework for evaluating the number of freeze cycles that a stack may see for a given application as well as the impact of insulation thickness, l_{ins}, since $k_{ins} = k_{ins}(l_{ins})$. It should be noted, however, that equation 76 does not contain a term to account for the heat of fusion of ice, which will act to increase t_{cd}. Therefore this model is limited to $T_t > 0°\text{C}$. Of course, the missing term could be added, but this would not solve the inherent drawback to this model, which is that, because the entire stack is assumed to be at one temperature, this approach provides no useful information regarding the thermal gradient that a given cell may experience.

To obtain such information, the transient temperature profile within the stack must be determined. A one-dimensional approach to this problem is presented by Bradean *et al.*[312] Here, the heat conduction equation is solved along the length of the stack (z-direction) assuming that the stack is insulated on one end and is cooled from the other. That is,

$$\frac{\partial T}{\partial t} = \alpha_s \frac{\partial^2 T}{\partial z^2} \quad \text{for } 0 < z < L_{stack} \tag{77}$$

where L_{stack} is the stack length and α_s is the average thermal diffusivity. As in the lumped case, a heat-transfer coefficient is used to connect the stack to the ambient temperature. However, this term removes heat only from the end of the stack, resulting in a temperature gradient in the z-

direction during cooling. This boundary condition is given by matching the conductive heat flux out of the system with Newton's law of cooling.

Naturally, the above approach can be extended to 2- or 3-D. Whether or not this is worthwhile largely depends on cell-stack geometry. In many stacks, the "sides" are flat and easily insulated, whereas the fluid, structural, and electrical connections are made through the ends of the stack. These connections are often made of metal and therefore readily conduct heat away from the stack and are difficult to insulate effectively. Therefore it is often the case that most of the cell-stack heat is lost through the ends and the 1-D cool-down model is sufficient.

6.1.2 Cell-level models

Once the thermal gradients within the stack are known, this information may be used to estimate water movement as a function of time during shutdown. There are two primary mechanisms for this water movement that are treated in the literature. The first is vapor-phase movement of water driven by the difference in partial pressure from one side of the cell to the other. Second, there is liquid-phase motion due to changes in capillary pressure that occur while the cell freezes. These will be discussed in turn.

6.1.2.1 Vapor phase. Modeling transient vapor-phase transport through the cell can be accomplished by applying equation 20, described in Section 2.1.3. This is done by setting the temperature boundary conditions to the temperatures computed using the cool-down model described above, setting the cell current density to zero, and allowing the cell to equilibrate to roughly 5°C, at which point vapor-phase transport becomes insignificant. An alternate, empirical approach is presented by Bradean *et al.*,[312] where the 1-D stack cool-down model described above is used to predict vapor-phase water transport within the cell. This is done by discretizing the temperature profile along the stack length, L_{stack}, based on the cell thickness. In other words, the n^{th} cell in the stack is assigned a temperature, $T_n(z,t)$ based on its position within the stack as well as time. Furthermore, $\Delta T_n(z,t)$ represents the approximate temperature gradient across the cell, that is $T_{n+1} - T_n$. These variables are then input into an empirically-derived water vapor flux equation of the form

$$f_w(T_n, \Delta T_n) = C_1 * \Delta T_n \exp(C_2 * T_n) \text{ if } \mathrm{w}_{\mathrm{mea}} > \mathrm{w}_{\mathrm{mea,min}} \ 0 < z < L_{stack} \tag{78}$$

$$f_w(T_n, \Delta T_n) = 0 \text{ if } \mathrm{w}_{\mathrm{mea}} \leq \mathrm{w}_{\mathrm{mea,min}} \tag{79}$$

where f_w is the water mass flux from the cell sandwich into the cold-side reactant channel, C_1 and C_2 are constants that are dependent on the membrane-electrode-assembly design, and w_{mea} is the mass water content of the cell. The constant $w_{mea,min}$ represents the minimum cell water content, which is hypothesized to be present primarily in the membrane. Once condensed in the channel, the water can presumably be purged out in the liquid phase prior to freezing. To obtain the water content for a given cell n as a function of time, the flux is integrated and subtracted from the initial water content, $w_{mea,0}$.

Verification of this model was undertaken and a sample result is shown in Figure 28. In this case, after 12 hours of cooling, at which point the cell stack is at a uniform temperature of 24°C, the amount of water present in the PEFC sandwich is measured, and the results compared to the model predictions. Good agreement exists between the simulation and model, and this serves to underscore the importance of vapor-phase water movement during cool-down as well as the importance of cell position. The cells on the end of the stack which was being cooled, where the thermal gradient was the highest, lost roughly half of their initial water content to the channels. The amount of water movement on the end of the stack, which was adiabatic, was minimal.

6.1.2.2 Liquid phase. As the cell continues to cool and the temperature approaches 0°C, vapor-phase transport of water becomes negligible. Once the cell is below 0°C, liquid water transport through the porous layers in the cell can occur, despite the fact that the temperature is below the freezing point of bulk water. This is possible because of the surface energies of pore network and water droplets, as governed by the Gibbs-Thomson equation,[313]

$$T_{FPD} = \frac{-2\overline{V}_{ice}\gamma T_m}{r\Delta H_f} \tag{80}$$

where T_{FPD} is the amount of freezing-point depression, $\overline{V}_{ice}$ is the molar volume of ice, γ is the surface tension of the ice-liquid interface, T_m is the melting (freezing) temperature for bulk water, ΔH_f is the heat of fusion of ice, and r is the pore radius. The amount of freezing-point depression in a given pore is primarily a function of pore radius – smaller pores tend to freeze at a lower temperature due to the shift in chemical potential. Because real media have distributions of pore radii, the fraction of unfrozen water vs. temperature is generally a continuum below 0°C.

As water freezes within the medium, the average effective pore radius is reduced. Consequently, the liquid pressure is also reduced according to capillary phenomena and assuming hydrophilic pores (see equation 39). In other words, the freezing of the water lowers the liquid pressure. This change in pressure can drive liquid water flow in two ways. First, within a homogeneous medium, if a temperature gradient exists (the medium is frozen from one side, for example), a pressure gradient will also exist. The liquid water in the cold region will be at a lower pressure than the hot region due to the lower average effective pore radius and to a much lesser extent, the lower density. Consequently, water will flow from hot to cold. Second, for two porous media in fluid contact, if the liquid-pressure versus saturation characteristics are different, a pressure differential will exist between the media as the cell is cooled, even if no temperature gradient exists. This pressure gradient can also drive liquid-water flow.

Under some conditions, the liquid-water flow described above can contribute to a phenomenon known as frost heave. During frost heave, a layer of pure ice known as an ice lens grows within the medium, displacing the surrounding material. Frost heave has been studied extensively in soil science and civil engineering due to its destructive impact on infrastructure. The phenomenon is not related to the volume expansion of water during freezing, as it has long been known to occur also within materials, such as benzene, which contract upon freezing.[314] In addition, ice lenses have been shown to grow in both hydrophobic and hydrophilic materials.[315]

For an ice lens to form, the forces holding the medium together, namely, the tensile strength of the material and any compressive force supplied externally, must be overcome. The sum of these forces is referred to as the "overburden." The maximum frost heave pressure, p_{max}, must therefore exceed the overburden pressure, p_0. Often the rigid-ice model, first described by Miller,[316] is used to determine p_{max}. In this case, it is assumed that the ice within the medium is continuous and at a uniform pressure, p_i, which is equivalent to p_{max}. To calculate p_i, the generalized Clapeyron equation (GCE) developed by Loch[317] is used. The GCE is derived from the Gibbs-Duhem equation and relates the ice pressure to the freezing-point depression,

$$\frac{p_i}{\rho_i} - \frac{p_w}{\rho_w} = -\Delta H_f \left(\frac{T_{FPD}}{T_m} \right) \tag{81}$$

Recent work by Rempel *et al.*[318] has called into question the validity of the rigid-ice model under conditions where a mixed zone of liquid and ice (called a "frozen fringe") is connected to the ice lens. In this case, the authors maintain, the maximum frost-heave pressure will be less than predicted by the GCE due to the forces acting on the ice within the fringe. Other models of frost heave also exist and have been reviewed by Henry.[319]

While frost heave has been investigated for decades, applying the models that have been developed to the PEM environment has only recently been attempted. He and Mench[320,321] have presented a 1-D, two-phase transient model which seeks to simulate both the movement of water during freeze as well as the growth of ice lenses. In their model, the domain includes half of the cell sandwich, from the membrane through one bipolar plate. The energy equation, which includes a source term for the heat of formation of ice, is used to predict the temperature profile in the domain during the freezing process based on an adiabatic condition on one boundary and heat loss via a heat-transfer coefficient linked to the ambient temperature on the other boundary.

Water is present in the model in membrane, liquid and ice phases; the movement of ice through regelation is neglected. Air is present in the channel, GDL, and CL, but is assumed to be at a constant and uniform pressure. In the membrane, a pure-diffusion model is used to account for liquid-water movement. Within the GDL and CL, liquid water moves under the influence of gradients in capillary pressure that occur once ice begins to form. The local capillary pressure is given by a Leverett *J*-function based on the effective saturation (see section 3.2.1). Gradients in water pressure are related to water flow in the model through the continuity equation and Darcy's law. The effective liquid permeability depends on the effective liquid saturation to the ninth power.

For an ice lens to initiate within the domain, the criteria of $p_i > p_0$ must be met. For growth of the ice lens to occur, in addition to the ice pressure continuing to exceed the overburden pressure, a supply of liquid water must be available to the "hot" side of the lens. That is, the growth rate of the ice lens is given by

$$\rho_i \frac{d\delta_{il}}{dt} = \rho_w (v_{in} - v_{out}) \tag{82}$$

where δ_{il} is the thickness of the ice lens and v_{in} and v_{out} are the velocities of the water coming into and out of the ice lens, respectively. The change in heat transfer due to the presence of the ice lens is also accounted for in the model.

While the model is 1-D, an attempt is made to simulate conditions under the rib as well as under the channel. This is done by adding a domain between the bipolar plate and the GDL which can simulate either an open channel or a rib. In the case of the open channel, liquid water is allowed to be expelled into the channel if the liquid pressure exceeds the air pressure. In the case of the rib, the water is constrained to stay within the porous media and membrane. Ice saturation predictions for both cases (under the rib and under the channel) during a freeze that starts at 5°C at time zero are shown in Figure 29. In this case, the initial liquid-water saturation was assumed to be 0.6 in the GDL, 0.1 in the CL, and λ=19 in the membrane. From the figure, one can clearly see that, as expected, more ice is formed under the rib; furthermore, the ice formation occurs principally from the rib into the GDL, although there is some in the wet membrane.

6.2 Startup from a Frozen State

Modeling water movement during cell shutdown and freeze is inherently difficult because it is a transient problem with multiple phase transitions that must be considered. It is made considerably simpler, however, by the fact that no electrochemical reaction is taking place. Unfortunately, this is not true during a startup from a frozen condition, making full simulations of this process quite complex.

In a typical startup, the initial condition is that the cell is at steady state at a temperature below 0°C, meaning that the majority of the residual water within the cell is frozen. Reactants are then fed to the stack until open circuit voltage is observed. A load is then applied across the stack. This load serves two purposes. First, it provides electricity to the power plant for equipment heating or useful load, depending on the cold-start strategy. Second, the waste heat generated within the stack raises the stack temperature. Eventually the stack warms itself to normal operating temperature, and the system operates as it normally would. Such a procedure is often referred to as a "bootstrap start," because the PEFC is in a sense "pulling itself up by its own bootstraps" since no heat input external to the power plant is utilized.

In practice, achieving a successful bootstrap start (as described above) is quite difficult. First, reactants must have sufficient access to both CLs. This means that, during the shutdown, ice must not have blocked reactant channels or the porous media. Second, assuming that the reactants are initially able to access the CL, the cell must heat up rapidly enough so that product water can be removed before it completely floods the porous media. This is especially troublesome for cells near the ends of the stack because of the high rate at which these cells lose heat to the environment. Of course, the objective of the start-up is not simply to heat the stack but for the power plant to deliver useful power as quickly as possible, adding another challenge to those described above. Available power is reduced during the cold start because all of the principal processes that contribute to cell inefficiency are negatively impacted by the low temperature. Mass-transport limitations increase due to both the presence of ice reducing the available open pore volume and product water build-up. Ionic conductivity is reduced due to the presence of ice in the membrane,[322] and the ORR is hindered both by the Arrhenius dependence on temperature (see equation 15) as well as reduced proton activity.[323]

To counter the difficulties of cold start, system designers use both procedural strategies and materials design. Examples of procedural strategies include adjusting the load profile applied during start to optimize performance or circulating coolant through the stack during start to improve thermal uniformity. Materials-design examples include reducing thermal mass to reduce warm-up time or adjusting pore structure to provide a greater reservoir for product water during cold start. However, evaluating these strategies experimentally is time-consuming and expensive. For this reason, having a model available that can be used to assess such strategies rapidly is very valuable. As with shutdown/freeze models, the (relatively few) cold-start models that have been published fall into two broad categories: stack level and cell level. These will be discussed in turn.

6.2.1 Stack-level models

The simplest model for startup is 0-D in that it treats the cell stack as a lumped mass with uniform properties. Such an approach was used by Pesaran[310] to estimate the total amount of thermal energy, Q_{tot}, required to raise the temperature of a cell stack from –20°C to +5°C. In this case the expression used is

$$Q_{tot} = \left(m_{comp} \hat{C}_{p,comp} + m_i \hat{C}_{p,i} \right) \Delta T_1 + m_i \Delta H_f + (m_{comp} \hat{C}_{p,comp} + m_w \hat{C}_{p,w}) \Delta T_2 \qquad (83)$$

where the subscript "comp" refers to the components of the stack, ΔT_1 is 0°C minus the starting temperature, and ΔT_2 is the final temperature minus 0°C.

The utility in this simple calculation is that it can be used to estimate start time roughly, assuming that the performance of the stack during startup is known. For example, assuming a stack with $n = 400$ cells, each with an active area of $A = 300 \text{ cm}^2$ operating at an average cell voltage of $V_c = 0.750$ V/cell at a current density of $i = 0.1 \text{ A/cm}^2$, the total amount of waste heat per unit time, q_{stack}, will be 8.8 kW. This is calculated from

$$Q_{stack} = n_c A_c Q \qquad (84)$$

where Q is given by equation 7. Assuming that $Q_{tot} = 5$ MJ is required to raise the temperature of the stack from –20°C to +5 °C, the total heat-up time would be calculated by dividing Q_{tot} by Q_{stack}, yielding roughly 570 seconds in this case. Note that this represents a lower bound for the actual heat-up time because heat loss during startup is not accounted for.

An alternate approach to that above is given by De Francesco and Arato,[324] who define the variable T_{stack} as the lumped stack temperature and present the expression

$$m_{stack} \hat{C}_{p,stack} \frac{\partial T_{stack}}{\partial t} = h_{air} a_{air} (T_{air} - T_{stack}) + h_{ext} a_{ext} (T_{ext} - T_{stack}) + Q \qquad (85)$$

where h_{air} is the heat-transfer coefficient between the cathode air and the stack and a_{air} is the contact area for the cathode air. Similarly, h_{ext} is the heat-transfer coefficient between the stack and the environment and a_{ext} is the external surface area of the stack. This approach has the advantage that the temperature of the stack is explicitly given as a function of time and that the temperature dependence of the cell voltage can be incorporated. It should be noted, however, that this approach does not account for the heat of fusion of ice within the cell.

0-D models can be used to estimate some design parameters for PEFC components. For example, for a given target start time, the maximum allowable thermal mass for the components and a minimum per-cell performance criterion could be specified. However, these would only be preliminary estimates due to nonuniformities in operating temperature, both from cell to cell and within a given cell.

One significant source of cell-to-cell nonuniformity in temperature is heat loss through the stack end structure. One way to address this problem is to use a 1-D model, such as that developed by Sundaresan and Moore.[325,326] This model predicts variations in temperature along the length of the stack, including end structure. To do this, the stack is divided into layers, including two 3-layer end structure assemblies as well as *n* 7-layer cells. Each layer is assumed to have homogeneous properties, including temperature. To solve for the temperature of a given layer, an energy balance, similar to that in equation 22, is utilized. The amount of heat generated by a given cell will depend on its cell voltage and current, and the cell voltage will in turn depend on the cell temperature; the model incorporates a correction to cell voltage based on the Nernst equation (equation 4).

6.2.2 Cell-level models

Cell performance is a function not only of temperature, but also of the amount and state of water present in the porous media and membrane. These parameters affect both ionic conductivity and mass-transport limitations, and the stack models described above do not account for these effects. To do so, more detailed cell-level models are required.

A semi-empirical approach to this problem is presented by Oszipok *et al.*[327] The authors performed isothermal, potentiostatic "cold-sweep" experiments using a single cell with a 33 cm^2 active area. Cold-sweep experiments differ from cold starts in that the cell temperature remains fixed at a point below 0°C rather than being allowed to rise under the influence of the cell's waste heat. Cold sweeps may be either potentiostatic or galvanostatic. In either case, the cell power will eventually drop to zero once enough product water is frozen to block reactant access to the catalyst completely.

In this case, during the experiment the current density was observed to rise asymptotically and then decrease rapidly to near zero. The authors attempt to model this behavior using a 1-D isothermal approach that accounts for four effects: the membrane resistance, the contact resistance, the exchange current density, and the oxygen diffusion coefficient. Each of these parameters is related empirically to the cumulative charge transfer. The results of the model predict a decrease in R_m with time during the cold sweep, presumably because the membrane is absorbing water and becoming liquid equilibrated. Other empirical relations are given that predict, with increasing charge transfer, an increasing contact resistance, a decreasing exchange current density, and a decreasing oxygen diffusion coefficient. To predict the overall current density as a function of time, these four parameters are used as inputs into the 1-D model of

Springer *et al.*[154] at each time step. Using this model, the behavior of the current density observed in the experiment is simulated with some success, as shown in Figure 30. The current density increases as the membrane resistance decreases, but once the cumulative charge transfer reaches a critical threshold, it drops due to increasing contact resistance and GDL flooding.

On the one hand, this type of model provides a framework for explaining a given cell's behavior during a cold sweep. On the other hand, it is difficult to use as a design tool, that is, to use it to predict *a priori* how a cell will behave based on its material properties. This is because of the fact that, with regards to water management, the various cell layers are lumped together and the properties that one usually specifies in the design process, such as thickness, permeability, and porosity, are not explicitly considered. In addition, although the isothermal nature of the model means that it is fairly simple, it limits its usefulness for two reasons. First, it cannot be used to predict cell heat-up during cold start. It is possible to impose a thermal profile for a heat-up and time-step the model to predict performance based on that profile, but this assumes that one already knows the thermal profile, which implies that the model is being used to explain observed behavior, not to design a cell in advance. Second, the effect of nonuniformities in a given cell's temperature cannot be predicted, which is a significant limitation for modeling full-size cells.

Nonisothermal models can be used to address these problems, as shown by Hishinuma *et al.*[328] In their model, an energy balance is included, meaning that, given adiabatic boundary conditions, the cell temperature depends on the cell performance with time and *vice-versa*. In addition, thermally the model is 3-D. The cell performance in each of the discretized segments is determined using a cathode-performance model in which flooding of the electrode by ice is accounted for by modifying the Butler-Volmer equation (equation 14) to allow the active ares to decrease proportionally to the amount of ice frozen in the cell during each time step. Any water produced that is not removed in the gas phase by the reactant gases is assumed to freeze immediately, assuming that the cell temperature is below 0°C.

Using this model, either a cold sweep or a cold start can be evaluated simply by adjusting the thermal boundary conditions. Furthermore, the current-density profile across the cell planform can be predicted. Therefore it can be used in the design process to aid in predicting performance based on startup procedures as well as planform shape (*e.g.,* aspect ratio). However, as with the Oszipok model, the layers of the PEFC sandwich are not sufficiently distinguishable, and, therefore, the model is not well suited for evaluating proper cell-material specifications. In addition, liquid-phase-water removal from the cathode CL once the cell is above 0°C is not considered.

Mao and Wang[329] present a similar cold-start model that does incorporate a reduced set of material properties for individual layers and therefore may be useful as a preliminary design tool. These properties include CL porosity and ionomer content, GDL porosity, and the heat capacities of each layer. The model is 1-D, and water is considered to exist either in the membrane phase, as vapor, or as ice. An energy balance is included to account for thermal losses to the reactant gases and the surroundings. Because it is a cold-start model, the cell temperature is allowed to change with time, but the cell temperature is taken as a lumped parameter that is constant with position. As with Hishinuma *et al.*, this model assumes that all ice forms in the CL and neglects liquid-water transport out of the CL once the cell is above the freezing point. Unlike Hishinuma *et al.*, removal of product water into the membrane phase is accounted for explicitly.

Mao and Wang[330] have also developed a transient, multiphase, nonisothermal, 3-D model to simulate cold sweep. In the model, liquid water is not allowed, but water does exist in the membrane, vapor, and ice phases. As in their 1-D model, the presence of ice in a given porous medium reduces its permeability and restricts diffusion. In the CL, ice saturation also restricts the electrochemical area. As a result, as time proceeds, more and more product water turns to ice, and eventually the ORR is cut off, and the cell power goes to zero. Similar to the Hishinuma *et al*. model, a valuable output of this simulation is the current-density distribution down the channel with time. This helps one to understand which parts of the cell flood first. Unlike the Hishinuma *et al*. model, however, the properties of the individual PEFC layers are modeled explicitly, thereby providing greater insight into where the buildup of water is occurring and providing a tool for investigating the effects of some material properties.

Figure 31 shows results obtained from Mao and Wang given a cold sweep at −20°C and 0.04 A/cm^2. Each subplot represents a 2-D representation of ice saturation. The two dimensions are through-plane (*z*-direction) and in-plane (*y*-direction, rib and channel cross-section). Each column of subplots represents a different time during the sweep while each row represents the *x*-position along the channel. In this case, at any point in time, ice is predicted to be the greatest at the channel inlet and to form preferentially under the rib (the top half of the *y*-axis).

In summary, the most detailed cell models to date have focused on predicting cell performance and flooding during cold-sweep experiments. Due to the fixed-temperature boundary condition and the absence of liquid water in the porous media, this type of analysis is simpler than modeling a true cold start. It is also simpler to verify experimentally. Some models have been constructed for cold start, but to date these treat the cell sandwich as isothermal and do not consider the effects of liquid water once the cell temperature passes through the melting point. Unfortunately, the relationship between the predictions made by the cold-sweep analyses and the behavior of a cell during a cold start remains unclear. In other words, if a cell that is being constructed to start from a frozen condition is designed using a detailed cold-sweep model, it is not clear to what degree the material specifications will be correct. There is at least one basic material property, thermal conductivity, which plays a significant role in cold start, but which cannot be specified on the basis of a cold-sweep model. Clearly a gap exists in the ability to predict a complete cold start (*i.e.,* from the frozen state all the way to normal operating temperature) and in understanding when such a model should be used as opposed to a (simpler) cold-sweep model. To achieve the ability to optimize fully materials and procedures for cold start, this relationship must be explored further.

7 Higher-Temperature Operation

As the operating temperature of a PEFC is increased, there are several advantages. The most important perhaps is the ability for easier control and thermal (and water) management due to the higher temperature. Automotive manufacturers have a set a target of 120°C for operation, which is akin to the operating temperature of the internal combustion engine of today.[311,331] However, operation at that temperature requires the use of novel materials, and specifically, the membrane. The reason is that due to the exponential increase of water vapor pressure with temperature and the need not to pressurize and fully humidify the feed gases, the PEFC must operate at lower humidity to avoid diluting the oxygen too much. Therefore, the membrane must be able to conduct at low relative humidity; furthermore, it must also remain durable, work in the CLs, and conduct in the presence of liquid water which occurs during cool down and startup. The ideal situation is a membrane that conducts with dry feeds. Such a holy grail provides drastic simplifications for the PEFC system; however, there is not such a material currently, although it is an active area of research.[56] There are several reviews on the topic of higher-temperature (120 to 180°C) PEFC material requirements,[332-335] and the best and most comprehensive is the recent one by that of de Brujin *et al.*[336]

Before proceeding to discuss the handful of high-temperature PEFC models, the advantages and disadvantages of going to higher temperatures and (hence) lower relative humidities is discussed. In terms of advantages, as mentioned, the most important is system and water-management simplification if the humidity requirement can be removed. If it cannot to a significant degree, then the system is too large and too complex with too many parasitic power losses to be feasible; in addition, while flooding would be avoided, water management becomes a tradeoff between membrane conduction and gas-phase dilution by water vapor. Other advantages of higher-temperature operation include higher impurity tolerance, especially with carbon monoxide,[337] and faster kinetics and transport coefficients. However, the latter could be detrimental in terms of increasing the rate of side reactions such as carbon oxidation and platinum dissolution and increasing the gas crossover rates; also, the rate of physiochemical degradation of the various components may increase. Overall, the advantages seem to outweigh the disadvantages, assuming that the necessary material-property targets can be met.

While there has been substantial work experimentally for higher-temperature operation, especially in terms of novel membrane synthesis, there is a dearth in the number of models for these systems[202,338-343] and overall full-cell results.[344-347] This is not too surprising since the materials are still being developed and characterized *ex situ*, and the fabrication of the higher-temperature cells, especially the CLs, are difficult, as noted below. Figure 32 shows the polarization and high-frequency resistance results for a Nafion®-based system as the operating temperature is increased, keeping a more-or-less fixed inlet water partial pressure. These results are similar to the ones observed in section 4.1 and in Figure 3(b). As the temperature increases, the main factor becomes the membrane dehydration as seen in the resistance measurements. However, even if one *IR* corrects the data, there are significant oxygen-dilution mass-transfer effects at the end of the cell, which is one reason that the oxygen gain at 120°C is better than one expects from kinetics alone. As noted, although these data can be collected with Nafion®, the lifetime of the cell in Figure 32 is extremely short due to the low durability of Nafion® at temperatures greater than 100°C.

In terms of modeling, the higher-temperature systems can be modeled using the approaches and equations discussed throughout this article. In fact, the model is somewhat simpler since liquid water and two-phase flow are no longer significant factors. In terms of the novel membranes, most can be modeled using the same set of material properties as Nafion® (*i.e.*, electroosmotic coefficient, water diffusion coefficient, conductivity) just with a weaker dependence on water content and humidity. An exception to this is the polybenzimidazole (PBI) system since there is a phosphoric-acid electrolyte with both mobile cations and anions;[348,349] the modeling of this system is discussed separately below.

The most significant changes in the modeling approach are probably within the CLs, and specifically the cathode CL. These changes arise because of two factors. First, while replacing the membrane as a separator with a novel membrane is somewhat straightforward, placing a high-temperature membrane within a CL is more difficult due to problems of dispersing the ionomer and creating an efficient microstructure.[350,351] It may be that a different ionomer is required in the CLs, such as a low equivalent weight Nafion®-type polymer,[42] but this can create dissolution problems when liquid water exists, and there may be interfacial resistances and durability concerns due to the different properties of the membrane separator and CL ionomer.[352] The second factor pertains to a change in the rate of the ORR. This rate is now known to be dependent on the local relative humidity, where the reaction rate drops off rapidly below a relative humidity of 60% or so.[42,353,354] Whether this dependence is due to platinum surface species deactivation, lack of liquid water in the hydrophilic primary pores causing smaller active surface areas, or a decrease in the proton activity, accessibility, and possibly concentration is not known definitively.

Besides the simple models used for the above data analysis including equivalent circuits and the PBI models, the higher-temperature models are from Wang and coworkers.[202,342,343] In this set of models, they examine higher temperature (but not 120°C) operation with lower humidity feeds. The models demonstrate the need for water-management strategies and GDL properties to keep the membrane hydrated without diluting the oxygen gas rather than to prevent flooding (in fact, the models are single phase). It is determined that a functionally graded GDL is optimal, where it is more tortuous at the inlet to pressurize the water and hydrate the membrane and less tortuous near the exit to prevent more severe oxygen diffusional losses with the diluted oxygen. None of these models account for the CL effects mentioned above.

One of the most promising and developed membranes for PEFC high-temperature operation is that of PBI.[348,349] This system utilizes a membrane that contains impregnated or possibly tethered phosphoric acid.[355] Hence, it is similar to phosphoric acid fuel cells (PAFCs), which operate in the range of 180 to 200°C.[356] PAFCs have been modeled and experimentally explored, and a review of them is outside the scope of this article. Many of the features of PBI cells are similar to those PAFCs including problems of acid leaching and durability concerns of the electrodes and gains of high conductivity and minimal water management. In terms of modeling, a few numerical studies have been conducted with PBI PEFCs.[338-341] Of these models, Peng and Lee[338] conclude that thermal effects are dominant in the system, and that a key optimization is the channel to land area ratio. Hu *et al.*[341] examine durability and degradation concerns with a specific focus on matching experimental data regarding loss of active area and changes within the CLs. Finally, the models of Cheddie and Munroe[339,340] are perhaps the most detailed and examine such aspects as acid doping level in addition to the more typical analyses. They also show a relatively large influence of the thermal gradients and temperature increase among the cells as well as low catalyst utilization and various limitations in the CL.

8 Summary

In this review, we have examined recent modeling efforts to understand and optimize water management in polymer-electrolyte fuel cells (PEFCs) operating with hydrogen. The major focus has been on transport of the various species within the PEFC, and the different facets of water management such as the balance between membrane dehydration and cathode flooding. The basic governing equations and regions of the PEFC were introduced, and the detailed studies involving water-management phenomena discussed. These investigations include design considerations to optimize water management, examination of freeze and subzero effects, accumulation of water and transient effects both within a full cell and a constitutive layer, and detailed models of two-phase flow in the gas-diffusion layers.

Where appropriate, models were compared to one another, but, for the most part, the results of the models were discussed. In addition, the models were broken down into their constitutive parts in terms of describing the phenomena of interest. The reason for this is that model validation occurs with varying sets of experimental data, some of which are cell specific and all of which are somewhat general and tangential to the specific aspect being explored. This is one reason why it is hard to justify one approach over another by just looking at the modeling results, especially when one deals with different levels of model complexity and empiricism. In general, it seems reasonable that the more complex models, which are based on physical arguments, account for several dimensions, and do not contain many fitting parameters, are perhaps closest to reality. Of course, this assumes that they fit the experimental data and observations. For any model, a balance must be struck between the complexity required to describe the physical reality and the additional computational costs of such complexity. In other words, while more complex models more accurately describe the physics of the transport processes, they are more computationally costly and may have so many unknown parameters that their results are not as meaningful. Hopefully, this review has shown and broken-down for the reader the vast complexities and aspects of water management within PEFCs, and the various ways they have been and can be understood better through mathematical modeling.

9 Acknowledgements

The authors would like to acknowledge Dr. Mordechay Schlesinger for his invitation to write this review and Dr. Michael Hickner for providing the neutron-imaging results. This work was supported by UTC Power and the Assistant Secretary for Energy Efficiency and Renewable Energy, Office of Hydrogen, Fuel Cell, and Infrastructure Technologies, of the U. S. Department of Energy under contract number DE-AC02-05CH11231.

10 Nomenclature

a_i^α = activity of species *i* in phase α

$a_{k,p}$ = interfacial surface area between phases *k* and *p* per unit volume, 1/cm

$a_{1,2}^{\mathrm{o}}$ = interfacial area between the electronically conducting and membrane phases with no flooding, 1/cm

A = surface area, cm^2

A_{agg} = specific external surface area of the agglomerate, 1/cm

A_{c} = active area, cm^2

A_{d} = projected normal area, cm^2

A_{Pt} = reactive surface area of platinum, cm^2/g

B = channel half-width, cm

c = chord length, cm

c_{D} = coefficient of drag

$c_{i,k}$ = interstitial concentration of species *i* in phase *k*, mol/cm^3

c_T = total solution concentration or molar density, mol/cm^3

$\mathrm{C_j}$ = fitting parameter, index j

$\hat{C}_{p_k}$ = heat capacity of phase *k*, J/g-K

d = rib width, cm

$\mathbf{d}_i$ = driving force per unit volume acting on species *i* in phase *k*, J/cm^4

D_{abs} = absolute molecular diffusivity, cm^2/s

D_{eff} = effective diffusivity, cm^2/s

D_i = Fickian diffusion coefficient of species i in a mixture, cm^2/s

D_S = capillary diffusivity, cm^2/s

$D_{i,j}$ = diffusion coefficient of i in j, cm^2/s

D_{K_i} = Knudsen diffusion coefficient of species i, cm^2/s

E = effectiveness factor

f_k = shape factor, index number k

f_w = mass flux of water, g/cm^2-s

F = Faraday's constant, 96487 C/equiv

F_D = Drag force, N

$F\gamma$ = Surface tension force, N

$\mathbf{g}$ = acceleration due to gravity, cm/s^2

ΔG_h = Gibbs free energy of reaction h, J/mol

h = GDL thickness, cm

h_d = droplet height, cm

$h_{k,p}$ = heat-transfer coefficient between phases k and p, J/cm^{2}s-K

$\overline{H}_{i,k}$ = partial molar enthalpy of species i in phase k, J/mol

$H_{i,j}$ = Henry's constant for species i in component j, mol/cm^{3}kPa

ΔH_f = heat of fusion of ice, J/mol or J/g

ΔH_l = heat or enthalpy of reaction l, J/mol

i = superficial current density through the membrane, A/cm^2

$\mathbf{i}_k$ = current density in phase k, A/cm^2

i_{0_h} = exchange current density for reaction h, A/cm^2

i_h = transfer current density of reaction h per interfacial area between phases k and p, A/cm^2

$i_{\lim}$ = limiting current density, A/cm^2

$J(S)$ = Leverett J-function

$\mathbf{J}_{i,k}$ = flux density of species i in phase k relative the mass-average velocity of phase k, mol/cm^{2}s

k = effective hydraulic permeability, cm^2

k_{T_k} = thermal conductivity of phase k, J/cm^{2}K

k_r = relative hydraulic permeability

k_{sat} = saturated hydraulic permeability, cm^2

k_Φ = electrokinetic permeability, cm^2

K = Stokes law fitting function for droplet

$K_{i,j}$ = frictional interaction parameters between species i and j

l_k = thickness of phase or element k

L = catalyst layer thickness, cm

m = mass, g

m_{Pt} = loading of platinum, g/cm^2

M_i = molecular weight of species i, g/mol

$M_i^{z_i}$ = symbol for the chemical formula of species *i* in phase *k* having charge z_i

n_c = number of cells

n_h = number of electrons transferred in electrode reaction *h*

$\mathbf{N}_{i,k}$ = superficial flux density of species *i* in phase *k*, mol/cm^{2}s

p_0 = overburden pressure, kPa

p_i = partial pressure of species *i*, kPa

p_C = capillary pressure, kPa

p_k = total pressure of phase *k*, kPa

p_w^{vap} = vapor pressure of water, kPa

$\mathbf{q}_k$ = superficial heat flux through phase *k*, J/cm^{2}s

Q = total amount of heat generated, J/cm^{2}s

$Q_{k,p}$ = heat flux transferred between phases *k* and *p*, J/cm^{3}s

r = pore radius, cm

r_d = pore radius, cm

r_{evap} = rate of evaporation, mol/cm^{3}s

$r_{l,k-p}$ = rate of reaction *l* per unit of interfacial area between phases *k* and *p*, mol/cm^{2}s

R = ideal-gas constant, 8.3143 J/mol-K

R_{agg} = agglomerate radius, cm

$R_{g,k}$ = rate of homogenous reaction *g* in phase *k*, mol/cm^{3}s

$R_{i,j}$ = resistance of resistor *i,j* in Figure 8 where *ct* stands for charge-transfer, Ω cm^2

R' = total ohmic resistance, Ω cm^2

Re = Reynolds number

$s_{i,k,l}$ = stoichiometric coefficient of species *i* in phase *k* participating in reaction *l*

S = liquid saturation

S_0 = specific surface area, cm^2/cm^3

ΔS_h = entropy of reaction *h*, J/mol-K

t = time, s

T = absolute temperature, K

T_m = melting point of ice, K

u_i = mobility of species *i*, cm^{2}mol/J-s

u_j = velocity in channel *j*, cm/s

v = velocity, cm/s

U = reversible cell potential, V

U^θ = standard potential of reaction

U_H = enthalpy potential, V

$\mathbf{v}_k$ = superficial velocity of phase *k*, cm/s

V = cell potential, V

$\overline{V}_i$ = (partial) molar volume of species *i*, cm^3/mol

$\mathrm{w}_{\mathrm{mea}}$ = water content per unit area of membrane electrode assembly, g/cm^2

$W_{\mathrm{O}_2}^{\mathrm{diff}}$ = molar flow rate of oxygen to the agglomerate, mol/cm^{3}s
x = distance across the flow field, cm
$x_{i,k}$ = mole fraction of species *i* in phase *k*
y = distance along the flow-field channel, cm
z = distance across the cell sandwich, cm
z_i = valence or charge number of species *i*

Greek

α_a = anodic transfer coefficient
α_c = cathodic transfer coefficient
α_s = average stack thermal diffusivity, cm^2/s
α_w = water transport coefficient, mol^2/J-cm-s
β = net water flux per proton flux through the membrane
γ = surface tension, N/cm
δ_n = diffusion length or thickness of region *n*, cm
δ_{il} = ice lens thickness, cm
ζ = characteristic length, cm
ε_k = volume fraction of phase *k*
ε_o = bulk porosity
ε_V = bulk strain
ν_k = kinematic viscosity of phase *k*, cm^2/s

ξ = electroosmotic coefficient

Π_h = Peltier coefficient for charge-transfer reaction *h*, V

ρ_k = density of phase *k*, g/cm^3

σ_o = standard conductivity in the electronically conducting phase, S/cm

η_h = electrode overpotential of reaction *h*, V

η_{s_h} = surface overpotential of reaction *h*, V

θ = contact angle, degrees

$\Delta\theta$ = contact angle hysteresis, degrees

κ = conductivity of the ionically conducting phase, S/cm

λ = moles of water per mole of sulfonic acid sites

λ_L = relative mobility of the liquid phase

μ = viscosity, Pa-s

μ_i = (electro)chemical potential of species *i*, J/mol

μ_i^α = electrochemical potential of species *i* in phase α, J/mol

$\boldsymbol{\tau}$ = stress tensor, kPa

τ_k = tortuosity of phase *k*

ϕ = Thiele modulus, defined by eq 51 for the ORR

Φ_k = potential in phase *k*, V

ψ_i = Permeation coefficient of species i

Subscripts/Superscripts

0 = initial

1 = electronically conducting phase

2 = ionically conducting phase

A = advancing

agg = agglomerate

amb = ambient

cd = cool down

CL = catalyst layer

CV = control volume

eff = effective value, corrected for tortuosity and porosity

ext = external to the control volume

f = fixed ionic site in the membrane

film = film covering the agglomerate

FPD = freezing point depression

g = homogeneous reaction number

G = gas phase

h = electron-transfer reaction number

HOR = hydrogen-oxidation reaction

irrev = irreversible

i = generic species, element index, or ice phase

in = into the control volume

ins = insulation

j = generic species

k = generic phase

l = heterogeneous reaction number

L = liquid phase

m = mixture or membrane

m_0 = Oxygen partial pressure dependence (see eq 15)

max = maximum

min = maximum

ORR = oxygen-reduction reaction

out = out of the control volume

p = generic phase

R = receding

ref = parameter evaluated at the reference conditions

res = resistive

rev = reversible

s = solid phases

sens = sensible

stack = stack average value

t = target

tot = total

w = water

11 References

1. A. Prasanna, H. Y. Ha, E. A. Cho, S. A. Hong and I. H. Oh, *J. Power Sources*, 137, 1 (2004).
2. A. Z. Weber and J. Newman, *Chemical Reviews*, 104, 4679 (2004).
3. C. Y. Wang, *Chemical Reviews*, 104, 4727 (2004).
4. P. Costamagna and S. Srinivasan, *J. Power Sources*, 102, 242 (2001).
5. P. Costamagna and S. Srinivasan, *J. Power Sources*, 102, 253 (2001).
6. T. Okada, *J. New Mater. Electrochem. Syst.*, 4, 209 (2001).
7. M. A. J. Cropper, S. Geiger and D. M. Jollie, *J. Power Sources*, 131, 57 (2004).
8. W. Q. Tao, C. H. Min, X. L. Liu, Y. L. He, B. H. Yin and W. Jiang, *J. Power Sources*, 160, 359 (2006).
9. N. Djilali, *Energy*, 32, 269 (2007).
10. S. Tsushima, K. Teranishi and S. Hirai, *Electrochemical and Solid State Letters*, 7, A269 (2004).
11. S. Tsushima, K. Teranishi and S. Hirai, *Energy*, 30, 235 (2005).
12. K. R. Minard, V. V. Viswanathan, P. D. Majors, L. Q. Wang and P. C. Rieke, *J. Power Sources*, 161, 856 (2006).
13. K. W. Feindel, S. H. Bergens and R. E. Wasylishen, *Chemphyschem*, 7, 67 (2006).
14. J. St-Pierre, *J. Electrochem. Soc.*, 154, B88 (2007).
15. M. A. Hickner, N. P. Siegel, K. S. Chen, D. N. McBrayer, D. S. Hussey, D. L. Jacobson and M. Arif, *J. Electrochem. Soc.*, 153, A902 (2006).
16. R. Satija, D. L. Jacobson, M. Arif and S. A. Werner, *J. Power Sources*, 129, 238 (2004).
17. A. Turhan, K. Heller, J. S. Brenizer and M. M. Mench, *J. Power Sources*, 160, 1195 (2006).
18. J. J. Kowal, A. Turhan, K. Heller, J. Brenizer and M. M. Mench, *J. Electrochem. Soc.*, 153, A1971 (2006).
19. F. Y. Zhang, X. G. Yang and C. Y. Wang, *J. Electrochem. Soc.*, 153, A225 (2006).
20. X. Liu, H. Guo, F. Ye and C. F. Ma, *Electrochim. Acta*, 52, 3607 (2007).
21. K. Tuber, D. Pocza and C. Hebling, *J. Power Sources*, 124, 403 (2003).
22. X. G. Yang, F. Y. Zhang, A. L. Lubawy and C. Y. Wang, *Electrochemical and Solid State Letters*, 7, A408 (2004).

23. S. Litster, D. Sinton and N. Djilali, *J. Power Sources*, 154, 95 (2006).

24. P. K. Sinha, P. Halleck and C. Y. Wang, *Electrochemical and Solid State Letters*, 9, A344 (2006).

25. I. Manke, C. Hartnig, M. Grunerbel, W. Lehnert, N. Kardjilov, A. Haibel, A. Hilger, J. Banhart and H. Riesemeier, *Appl. Phys. Lett.*, 90, 3 (2007).

26. J. Newman and K. E. Thomas-Alyea, *Electrochemical Systems*, John Wiley & Sons, New York (2004).

27. A. J. Bard and L. R. Faulkner, *Electrochemical Methods: Fundamentals and Applications*, John Wiley & Sons, Inc., New York (2001).

28. D. M. Bernardi, E. Pawlikowski and J. Newman, *J. Electrochem. Soc.*, 132, 5 (1985).

29. L. Rao and J. Newman, *J. Electrochem. Soc.*, 144, 2697 (1997).

30. K. C. Neyerlin, W. B. Gu, J. Jorne and H. A. Gasteiger, *J. Electrochem. Soc.*, 153, A1955 (2006).

31. J. X. Wang, T. E. Springer and R. R. Adzic, *J. Electrochem. Soc.*, 153, A1732 (2006).

32. A. J. Appleby, *J. Electrochem. Soc.*, 117, 328 (1970).

33. K. Kinoshita, *Electrochemical Oxygen Technology*, John Wiley & Sons, Inc., New York (1992).

34. A. Parthasarathy, B. Dave, S. Srinivasan, A. J. Appleby and C. R. Martin, *J. Electrochem. Soc.*, 139, 1634 (1992).

35. P. D. Beattie, V. I. Basura and S. Holdcroft, *J. Electronanal. Chem.*, 468, 180 (1999).

36. A. Parthasarathy, S. Srinivasan, A. J. Appleby and C. R. Martin, *J. Electrochem. Soc.*, 139, 2530 (1992).

37. A. Parthasarathy, S. Srinivasan, A. J. Appleby and C. R. Martin, *J. Electrochem. Soc.*, 139, 2856 (1992).

38. Y. W. Rho, O. A. Velev and S. Srinivasan, *J. Electrochem. Soc.*, 141, 2084 (1994).

39. A. Parthasarathy, S. Srinivasan, A. J. Appleby and C. R. Martin, *J. Electronanal. Chem.*, 339, 101 (1992).

40. J. Perez, E. R. Gonzalez and E. A. Ticianelli, *Electrochim. Acta*, 44, 1329 (1998).

41. F. A. Uribe, T. E. Springer and S. Gottesfeld, *J. Electrochem. Soc.*, 139, 765 (1992).

42. K. C. Neyerlin, H. A. Gasteiger, C. K. Mittelsteadt, J. Jorne and W. B. Gu, *J. Electrochem. Soc.*, 152, A1073 (2005).

43. W. Liu and D. Zuckerbrod, *J. Electrochem. Soc.*, 152, A1165 (2005).

44. U. A. Paulus, T. J. Schmidt, H. A. Gasteiger and R. J. Behm, *J. Electronanal. Chem.*, 495, 134 (2001).

45. S. F. Burlatsky, V. Atrazhev, N. Cipollini, D. Condit and N. Erikhman, *ECS Transactions*, 1, 239 (2006).

46. R. M. Darling and J. P. Meyers, *J. Electrochem. Soc.*, 150, A1523 (2003).

47. R. M. Darling and J. P. Meyers, *J. Electrochem. Soc.*, 152, A242 (2005).

48. C. A. Reiser, L. Bregoli, T. W. Patterson, J. S. Yi, J. D. L. Yang, M. L. Perry and T. D. Jarvi, *Electrochemical and Solid State Letters*, 8, A273 (2005).

49. J. P. Meyers and R. M. Darling, *J. Electrochem. Soc.*, 153, A1432 (2006).

50. R. B. Bird, W. E. Stewart and E. N. Lightfoot, *Transport Phenomena*, John Wiley & Sons, Inc., New York (2002).

51. J. J. Hwang, C. H. Chao, C. L. Chang, W. Y. Ho and D. Y. Wang, *Int. J. Hydrog. Energy*, 32, 405 (2007).

52. A. Z. Weber and J. Newman, *J. Electrochem. Soc.*, 153, A2205 (2006).

53. L. M. Onishi, J. M. Prausnitz and J. Newman, *J. Phys. Chem. B*, 111, 10166 (2007).

54. A. Z. Weber and J. Newman, *J. Electrochem. Soc.*, 150, A1008 (2003).

55. R. B. Moore and C. R. Martin, *Macromolecules*, 21, 1334 (1988).

56. M. A. Hickner, H. Ghassemi, Y. S. Kim, B. R. Einsla and J. E. McGrath, *Chemical Reviews*, 104, 4587 (2004).

57. K. D. Kreuer, S. J. Paddison, E. Spohr and M. Schuster, *Chemical Reviews*, 104, 4637 (2004).

58. A. Z. Weber and J. Newman, in *Advances in Fuel Cells, Vol. 1*, T. S. Zhao, K.-D. Kreuer and T. V. Nguyen Editors, Elsevier, Amsterdam (2007).

59. J. Fimrite, H. Struchtrup and N. Djilali, *J. Electrochem. Soc.*, 152, A1804 (2005).

60. B. Carnes and N. Djilali, *Electrochim. Acta*, 52, 1038 (2006).

61. J. Fimrite, B. Carnes, H. Struchtrup and N. Djilali, *J. Electrochem. Soc.*, 152, A1815 (2005).

62. T. Thampan, S. Malhotra, H. Tang and R. Datta, *J. Electrochem. Soc.*, 147, 3242 (2000).

63. M. Wohr, K. Bolwin, W. Schnurnberger, M. Fischer, W. Neubrand and G. Eigenberger, *Int. J. Hydrog. Energy*, 23, 213 (1998).

64. A. Z. Weber and J. Newman, *J. Electrochem. Soc.*, 151, A311 (2004).

65. P. N. Pintauro and D. N. Bennion, *Ind. Eng. Chem. Fundam.*, 23, 230 (1984).

66. T. F. Fuller, Solid-polymer-electrolyte Fuel Cells, in, University of California, Berkeley, CA (1992).

67. B. S. Pivovar, *Polymer*, 47, 4194 (2006).

68. M. W. Verbrugge and R. F. Hill, *J. Electrochem. Soc.*, 137, 886 (1990).

69. R. Schlögl, *Zeitschrift für physikalische Chemie, Neue Folge*, 3, 73 (1955).

70. T. Okada, *J. Electronanal. Chem.*, 465, 1 (1999).

71. T. Okada, G. Xie and M. Meeg, *Electrochim. Acta*, 43, 2141 (1998).

72. J. Divisek, M. Eikerling, V. Mazin, H. Schmitz, U. Stimming and Y. M. Volfkovich, *J. Electrochem. Soc.*, 145, 2677 (1998).

73. M. Eikerling, A. A. Kornyshev and U. Stimming, *J. Phys. Chem. B*, 101, 10807 (1997).

74. P. Choi, N. H. Jalani and R. Datta, *J. Electrochem. Soc.*, 152, A1548 (2005).

75. P. Choi, N. H. Jalani and R. Datta, *J. Electrochem. Soc.*, 152, E84 (2005).

76. A. Z. Weber and J. Newman, *AIChE J.*, 50, 3215 (2004).

77. I. Nazarov and K. Promislow, *J. Electrochem. Soc.*, 154, B623 (2007).

78. A. Z. Weber and J. Newman, *J. Electrochem. Soc.*, 154, B405 (2007).

79. S. S. Kocha, J. D. L. Yang and J. S. Yi, *AIChE J.*, 52, 1916 (2006).

80. A. Taniguchi, T. Akita, K. Yasuda and Y. Miyazaki, *J. Power Sources*, 130, 42 (2004).

81. X. Cheng, Z. Shi, N. Glass, L. Zhang, J. J. Zhang, D. T. Song, Z. S. Liu, H. J. Wang and J. Shen, *J. Power Sources*, 165, 739 (2007).

82. M. S. Mikkola, T. Rockward, F. A. Uribe and B. S. Pivovar, *Fuel Cells*, 7, 153 (2007).

83. R. C. Makkus, A. H. H. Janssen, F. A. de Bruijn and R. Mallant, *J. Power Sources*, 86, 274 (2000).

84. K. Promislow, J. Stockie and B. Wetton, *Proc. R. Soc. London, A*, 462, 789 (2006).

85. A. Z. Weber, R. M. Darling and J. Newman, *J. Electrochem. Soc.*, 151, A1715 (2004).

86. J. H. Nam and M. Kaviany, *Int. J. Heat Mass Transfer*, 46, 4595 (2003).

87. J. T. Gostick, M. W. Fowler, M. A. Ioannidis, M. D. Pritzker, Y. M. Volfkovich and A. Sakars, *J. Power Sources*, 156, 375 (2006).

88. J. Benziger, J. Nehlsen, D. Blackwell, T. Brennan and J. Itescu, *J. Membr. Sci.*, 261, 98 (2005).

89. J. J. Hwang, *J. Electrochem. Soc.*, 153, A216 (2006).

90. A. Z. Weber and J. Newman, *ECS Transactions*, 1 (16), 61 (2005).

91. R. E. De La Rue and C. W. Tobias, *J. Electrochem. Soc.*, 106, 827 (1959).

92. D. A. G. Bruggeman, *Ann. Physik.*, 24, 636 (1935).

93. G. Li and P. P. Pickup, *J. Electrochem. Soc.*, 150, C745 (2003).

94. D. M. Bernardi, Mathematical Modeling of Lithium(alloy) IronSulfide Cells and the Electrochemical Precipitation of Nickel Hydroxide, in, University of California, Berkeley (1986).

95. M. Knudsen, *The Kinetic Theory of Gases*, Methuen, London (1934).

96. L. B. Rothfeld, *AIChE J.*, 9, 19 (1963).

97. A. Z. Weber and J. Newman, *International Communications in Heat and Mass Transfer*, 32, 855 (2005).

98. E. A. Mason and A. P. Malinauskas, *Gas Transport in Porous Media: The Dusty-Gas Model*, Elsevier, Amsterdam (1983).

99. C. T. Miller, G. Christakos, P. T. Imhoff, J. F. McBride, J. A. Pedit and J. A. Trangenstein, *Advances in Water Resources*, 21, 77 (1998).

100. F. A. L. Dullien, *Porous Media: Fluid Transport and Pore Structure*, Academic Press, Inc., New York (1992).

101. J. Bear, *Dynamics of Fluids in Porous Media*, Dover Publications, Inc., New York (1988).

102. W. O. Smith, *Physics*, 4, 425 (1933).

103. M. C. Leverett, *Petroleum Division Transactions of the American Institute of Mining and Metallurgical Engineers*, 142, 152 (1941).

104. C. Y. Wang and P. Cheng, *Adv. Heat. Trans.*, 30, 93 (1997).

105. C. Y. Wang and P. Cheng, *Int. J. Heat Mass Transfer*, 39, 3607 (1996).

106. Z. H. Wang, C. Y. Wang and K. S. Chen, *J. Power Sources*, 94, 40 (2001).

107. S. A. Freunberger, M. Santis, I. A. Schneider, A. Wokaun and F. N. Buchi, *J. Electrochem. Soc.*, 153, A396 (2006).

108. F. N. Buchi, A. B. Geiger and R. P. Neto, *J. Power Sources*, 145, 62 (2005).

109. H. Meng and C. Y. Wang, *J. Electrochem. Soc.*, 151, A358 (2004).

110. A. Fischer, J. Jindra and H. Wendt, *J. Appl. Electrochem.*, 28, 277 (1998).

111. E. A. Ticianelli, J. G. Beery and S. Srinivasan, *J. Appl. Electrochem.*, 21, 597 (1991).

112. X. Cheng, B. Yi, M. Han, J. Zhang, Y. Qiao and J. Yu, *J. Power Sources*, 79, 75 (1999).

113. E. Passalacqua, F. Lufrano, G. Squadrito, A. Patti and L. Giorgi, *Electrochim. Acta*, 46, 799 (2001).

114. M. Uchida, Y. Aoyama, N. Eda and A. Ohta, *J. Electrochem. Soc.*, 142, 4143 (1995).

115. P. Berg, A. Novruzi and K. Promislow, *Chem. Eng. Sci.*, 61, 4316 (2006).

116. G. Y. Lin, W. S. He and T. Van Nguyen, *J. Electrochem. Soc.*, 151, A1999 (2004).

117. W. Sun, B. A. Peppley and K. Karan, *Electrochim. Acta*, 50, 3359 (2005).

118. K. M. Yin, *J. Electrochem. Soc.*, 152, A583 (2005).

119. G. Q. Wang, P. P. Mukherjee and C. Y. Wang, *Electrochim. Acta*, 51, 3139 (2006).

120. G. Q. Wang, P. P. Mukherjee and C. Y. Wang, *Electrochim. Acta*, 51, 3151 (2006).

121. Z. N. Farhat, *J. Power Sources*, 138, 68 (2004).

122. J. Xie, D. L. Wood, K. L. More, P. Atanassov and R. L. Borup, *J. Electrochem. Soc.*, 152, A1011 (2005).

123. Y. Bultel, P. Ozil and R. Durand, *J. Appl. Electrochem.*, 30, 1369 (2000).

124. Y. Bultel, P. Ozil and R. Durand, *Electrochim. Acta*, 43, 1077 (1998).

125. Y. Bultel, P. Ozil and R. Durand, *J. Appl. Electrochem.*, 28, 269 (1998).

126. Y. Bultel, P. Ozil and R. Durand, *J. Appl. Electrochem.*, 29, 1025 (1999).

127. O. Antoine, Y. Bultel, R. Durand and P. Ozil, *Electrochim. Acta*, 43, 3681 (1998).

128. J. Euler and W. Nonnenmacher, *Electrochim. Acta*, 2, 268 (1960).

129. J. S. Newman and C. W. Tobias, *J. Electrochem. Soc.*, 109, 1183 (1962).

130. J. Newman and W. Tiedemann, *AIChE J.*, 21, 25 (1975).

131. J. O. M. Bockris and S. Srinivasan, *Fuel Cells: Their Electrochemistry*, McGraw-Hill, New York (1969).

132. P. DeVidts and R. E. White, *J. Electrochem. Soc.*, 144, 1343 (1997).

133. A. A. Shah, G. S. Kim, W. Gervais, A. Young, K. Promislow, J. Li and S. Ye, *J. Power Sources*, 160, 1251 (2006).

134. H. S. Fogler, *Elements of Chemical Reaction Engineering*, Prentice-Hall, Upper Saddle River, NJ (1992).

135. E. W. Thiele, *Industrial & Engineering Chemistry*, 31, 916 (1939).

136. M. Eikerling, A. S. Ioselevich and A. A. Kornyshev, *Fuel Cells*, 4, 131 (2004).

137. M. Secanell, K. Karan, A. Suleman and N. Djilali, *Electrochim. Acta*, 52, 6318 (2007).

138. Q. P. Wang, M. Eikerling, D. T. Song, Z. S. Liu, T. Navessin, Z. Xie and S. Holdcroft, *J. Electrochem. Soc.*, 151, A950 (2004).

139. D. T. Song, Q. P. Wang, Z. S. Liu, M. Eikerling, Z. Xie, T. Navessin and S. Holdcroft, *Electrochim. Acta*, 50, 3347 (2005).

140. M. Eikerling, *J. Electrochem. Soc.*, 153, E58 (2006).

141. C. Y. Du, T. Yang, R. F. Shi, G. R. Yin and X. Q. Cheng, *Electrochim. Acta*, 51, 4934 (2006).

142. M. Eikerling and A. A. Kornyshev, *J. Electronanal. Chem.*, 475, 107 (1999).

143. N. Wagner, *J. Appl. Electrochem.*, 32, 859 (2002).

144. C. Y. Yuh and J. R. Selman, *AIChE J.*, 34, 1949 (1988).

145. I. D. Raistrick, *Electrochim. Acta*, 35, 1579 (1990).

146. R. Makharia, M. F. Mathias and D. R. Baker, *J. Electrochem. Soc.*, 152, A970 (2005).

147. O. Himanen and T. Hottinen, *Electrochim. Acta*, 52, 581 (2006).

148. J. M. Le Canut, R. M. Abouatallah and D. A. Harrington, *J. Electrochem. Soc.*, 153, A857 (2006).

149. M. Schulze, N. Wagner, T. Kaz and K. A. Friedrich, *Electrochim. Acta*, 52, 2328 (2007).

150. F. Jaouen and G. Lindbergh, *J. Electrochem. Soc.*, 150, A1699 (2003).

151. T. E. Springer, T. A. Zawodzinski, M. S. Wilson and S. Gottesfeld, *J. Electrochem. Soc.*, 143, 587 (1996).

152. Q. Z. Guo and R. E. White, *J. Electrochem. Soc.*, 151, E133 (2004).

153. K. Wiezell, P. Gode and G. Lindbergh, *J. Electrochem. Soc.*, 153, A749 (2006).

154. T. E. Springer, T. A. Zawodzinski and S. Gottesfeld, *J. Electrochem. Soc.*, 138, 2334 (1991).

155. S. Patankar, *Numerical Heat Transfer and Fluid Flow*, Hemisphere Publishing Corporation (1980).

156. K. S. Udell, *Int. J. Heat Mass Transfer*, 28, 485 (1985).

157. J. P. Feser, A. K. Prasad and S. G. Advani, *J. Power Sources*, 162, 1226 (2006).

158. E. C. Kumbur, K. V. Sharp and M. M. Mench, *J. Power Sources*, 168, 356 (2007).

159. U. Pasaogullari and C. Y. Wang, *J. Electrochem. Soc.*, 152, A380 (2005).

160. C. H. Chao and A. J. J. Hwang, *J. Power Sources*, 160, 1122 (2006).

161. V. Gurau, M. J. Bluemle, E. S. De Castro, Y. M. Tsou, T. A. Zawodzinski and J. A. Mann, *J. Power Sources*, 165, 793 (2007).

162. X. W. Shan and H. D. Chen, *Physical Review E*, 47, 1815 (1993).

163. X. W. Shan and H. D. Chen, *Physical Review E*, 49, 2941 (1994).

164. C. Pan, M. Hilpert and C. T. Miller, *Water Resources Research*, 40 (2004).

165. C. R. Ethier, *AIChE J.*, 37, 1227 (1991).

166. K. E. Thompson, *AIChE J.*, 48, 1369 (2002).

167. H. J. Vogel, J. Tolke, V. P. Schulz, M. Krafczyk and K. Roth, *Vadose Zone Journal*, 4, 380 (2005).

168. V. P. Schulz, J. Becker, A. Wiegmann, P. P. Mukherjee and C. Y. Wang, *J. Electrochem. Soc.*, 154, B419 (2007).

169. P. K. Sinha and C. Y. Wang, *ECS Transactions*, 3, 387 (2006).

170. M. S. Valavanides and A. C. Payatakes, *Advances in Water Resources*, 24, 385 (2001).

171. M. Prat, *Int. J. Heat Mass Transfer*, 50, 1455 (2007).

172. B. Markicevic and N. Djilali, *Physics of Fluids*, 18 (2006).

173. R. D. Hazlett, *Transport in Porous Media*, 20, 21 (1995).

174. V. Sygouni, C. D. Tsakiroglou and A. C. Payatakes, *Physics of Fluids*, 18 (2006).

175. Y. Shi, J. S. Xiao, M. Pan and R. Z. Yuan, *J. Power Sources*, 160, 277 (2006).

176. G. L. He, Z. C. Zhao, P. W. Ming, A. Abuliti and C. Y. Yin, *J. Power Sources*, 163, 846 (2007).

177. U. Pasaogullari, C. Y. Wang and K. S. Chen, *J. Electrochem. Soc.*, 152, A1574 (2005).

178. A. T. Corey, *Producer's Monthly*, 18, 38 (1954).

179. R. H. Brooks and A. T. Corey, in *Hydrology Papers*, Colorado State University (1964).

180. M. T. Vangenuchten, *Soil Science Society of America Journal*, 44, 892 (1980).

181. D. Natarajan and T. V. Nguyen, *J. Electrochem. Soc.*, 148, A1324 (2001).

182. X. L. Wang, H. M. Zhang, J. L. Zhang, H. F. Xu, Z. Q. Tian, J. Chen, H. X. Zhong, Y. M. Liang and B. L. Yi, *Electrochim. Acta*, 51, 4909 (2006).

183. M. S. Wilson, J. A. Valerio and S. Gottesfeld, *Electrochim. Acta*, 40, 355 (1995).

184. N. Hara, K. Tsurumi and M. Watanabe, *J. Electronanal. Chem.*, 413, 81 (1996).

185. E. Passalacqua, G. Squadrito, F. Lufrano, A. Patti and L. Giorgi, *J. Appl. Electrochem.*, 31, 449 (2001).

186. K. Karan, H. Atiyeh, A. Phoenix, E. Halliop, J. Pharoah and B. Peppley, *Electrochemical and Solid State Letters*, 10, B34 (2007).

187. Z. G. Qi and A. Kaufman, *J. Power Sources*, 109, 38 (2002).

188. Z. G. Zhan, J. S. Xiao, D. Y. Li, M. Pan and R. Z. Yuan, *J. Power Sources*, 160, 1041 (2006).

189. G. J. M. Janssen and M. L. J. Overvelde, *J. Power Sources*, 101, 117 (2001).

190. V. A. Paganin, E. A. Ticianelli and E. R. Gonzalez, *J. Appl. Electrochem.*, 26, 297 (1996).

191. C. S. Kong, D.-Y. Kim, H.-K. Lee, Y.-G. Shul and T.-H. Lee, *J. Power Sources*, 108, 185 (2002).

192. A. A. Shah, G. S. Kim, P. C. Sui and D. Harvey, *J. Power Sources*, 163, 793 (2007).

193. S. Shimpalee, U. Beuscher and J. W. Van Zee, *J. Power Sources*, 163, 480 (2006).

194. J. Chen, T. Matsuura and M. Hori, *J. Power Sources*, 131, 155 (2004).

195. U. Pasaogullari and C. Y. Wang, *Electrochim. Acta*, 49, 4359 (2004).

196. A. Z. Weber and J. Newman, *J. Electrochem. Soc.*, 152, A677 (2005).

197. E. Birgersson, M. Noponen and M. Vynnycky, *J. Electrochem. Soc.*, 152, A1021 (2005).

198. J. Ramousse, J. Deseure, O. Lottin, S. Didierjean and D. Maillet, *J. Power Sources*, 145, 416 (2005).

199. Y. Y. Shan and S. Y. Choe, *J. Power Sources*, 145, 30 (2005).

200. H. Ju, H. Meng and C. Y. Wang, *Int. J. Heat Mass Transfer*, 48, 1303 (2005).

201. G. L. Hu and J. R. Fan, *Energy Fuels*, 20, 738 (2006).

202. H. C. Ju, C. Y. Wang, S. Cleghorn and U. Beuscher, *J. Electrochem. Soc.*, 153, A249 (2006).

203. Y. Wang and C. Y. Wang, *J. Electrochem. Soc.*, 153, A1193 (2006).

204. O. N. Scholes, S. A. Clayton, A. F. A. Hoadley and C. Tiu, *Transport in Porous Media*, 68, 365 (2007).

205. J. G. Pharoah, K. Karan and W. Sun, *J. Power Sources*, 161, 214 (2006).

206. U. Pasaogullari, P. P. Mukherjee, C. Y. Wang and K. S. Chen, *J. Electrochem. Soc.*, 154, B823 (2007).

207. M. M. Tomadakis and S. V. Sotirchos, *AIChE J.*, 37, 74 (1991).

208. J. T. Gostick, M. W. Fowler, M. D. Pritzker, M. A. Ioannidis and L. M. Behra, *J. Power Sources*, 162, 228 (2006).

209. T. I. I. Toray Carbon Fiber Paper "TGP-H" Property Sheet, in.

210. H. Meng, *J. Power Sources*, 161, 466 (2006).

211. M. Khandelwal and M. M. Mench, *J. Power Sources*, 161, 1106 (2006).

212. G. W. Jackson and D. F. James, *Can. J. Chem. Eng.*, 64, 364 (1986).

213. J. G. Pharoah, *J. Power Sources*, 144, 77 (2005).

214. M. V. Williams, H. R. Kunz and J. M. Fenton, *J. Electrochem. Soc.*, 151, A1617 (2004).

215. W. K. Lee, C. H. Ho, J. W. Van Zee and M. Murthy, *J. Power Sources*, 84, 45 (1999).

216. J. Ihonen, M. Mikkola and G. Lindbergh, *J. Electrochem. Soc.*, 151, A1152 (2004).

217. P. Zhou, C. W. Wu and G. J. Ma, *J. Power Sources*, 163, 874 (2007).

218. P. Zhou and C. W. Wu, *J. Power Sources*, 170, 93 (2007).

219. P. C. Sui and N. Djilali, *J. Power Sources*, 161, 294 (2006).

220. J. B. Ge, A. Higier and H. T. Liu, *J. Power Sources*, 159, 922 (2006).

221. W. R. Chang, J. J. Hwang, F. B. Weng and S. H. Chan, *J. Power Sources*, 166, 149 (2007).

222. T. Hottinen and O. Himanen, *Electrochemistry Communications*, 9, 1047 (2007).

223. M. Mathias, J. Roth, J. Fleming and W. Lehnert, in *Handbook of Fuel Cells: Fundamentals, Technology, and Applications, Vol. 3*, W. Vielstich, A. Lamm and H. A. Gasteiger Editors, John Wiley & Sons, Inc., New York (2003).

224. Y. L. Tang, A. M. Karlsson, M. H. Santare, M. Gilbert, S. Cleghorn and W. B. Johnson, *Materials Science and Engineering a-Structural Materials Properties Microstructure and Processing*, 425, 297 (2006).

225. O. C. Zienkiewicz and R. L. Taylor, *The Finite Element Method*, Butterworth-Heinemann, Oxford, UK (2000).

226. A. Bazylak, D. Sinton, Z. S. Liu and N. Djilali, *J. Power Sources*, 163, 784 (2007).

227. E. Endoh, S. Terazono, H. Widjaja and Y. Takimoto, *Electrochemical and Solid State Letters*, 7, A209 (2004).

228. G. H. Guvelioglu and H. G. Stenger, *J. Power Sources*, 147, 95 (2005).

229. G. H. Guvelioglu and H. G. Stenger, *J. Power Sources*, 163, 882 (2007).

230. W. Huang, B. Zhou and A. Sobiesiak, *J. Electrochem. Soc.*, 153, A1945 (2006).

231. H. Meng and C. Y. Wang, *Chem. Eng. Sci.*, 59, 3331 (2004).

232. P. T. Nguyen, T. Berning and N. Djilali, *J. Power Sources*, 130, 149 (2004).

233. H. C. Ju, C. Y. Wang, S. Cleghorn and U. Beuscher, *J. Electrochem. Soc.*, 152, A1645 (2005).

234. H. Ju, G. Luo and C. Y. Wang, *J. Electrochem. Soc.*, 154, B218 (2007).

235. S. Shimpalee, S. Greenway, D. Spuckler and J. W. Van Zee, *J. Power Sources*, 135, 79 (2004).

236. S. A. Freunberger, A. Wokaun and F. N. Buchi, *J. Electrochem. Soc.*, 153, A909 (2006).

237. Y. Wang and C. Y. Wang, *J. Power Sources*, 153, 130 (2006).

238. T. W. Patterson and R. M. Darling, *Electrochemical and Solid State Letters*, 9, A183 (2006).

239. P. W. Li, L. Schaefer, Q. M. Wang, T. Zhang and M. K. Chyu, *J. Power Sources*, 115, 90 (2003).

240. Y. Zong, B. Zhou and A. Sobiesiak, *J. Power Sources*, 161, 143 (2006).

241. C. I. Lee and H. S. Chu, *J. Power Sources*, 161, 949 (2006).

242. J. S. Yi, J. D. L. Yang and C. King, *AIChE J.*, 50, 2594 (2004).

243. E. C. Kumbur, K. V. Sharp and M. M. Mench, *J. Power Sources*, 161, 333 (2006).

244. Z. G. Zhan, J. S. Xiao, M. Pan and R. Z. Yuan, *J. Power Sources*, 160, 1 (2006).

245. K. Jiao, B. Zhou and P. Quan, *J. Power Sources*, 154, 124 (2006).

246. P. Quan and M. C. Lai, *J. Power Sources*, 164, 222 (2007).

247. H. Meng and C. Y. Wang, *J. Electrochem. Soc.*, 152, A1733 (2005).

248. K. S. Chen, M. A. Hickner and D. R. Noble, *International Journal of Energy Research*, 29, 1113 (2005).

249. G. L. He, P. W. Ming, Z. C. Zhao, A. Abudula and Y. Xiao, *J. Power Sources*, 163, 864 (2007).

250. D. P. Wilkinson and J. St-Pierre, *J. Power Sources*, 113, 101 (2003).

251. P. Berg, K. Promislow, J. St Pierre, J. Stumper and B. Wetton, *J. Electrochem. Soc.*, 151, A341 (2004).

252. E. Birgersson and M. Vynnycky, *J. Power Sources*, 153, 76 (2006).

253. S. Um and C. Y. Wang, *J. Power Sources*, 156, 211 (2006).

254. Y. Wang and C. Y. Wang, *J. Power Sources*, 147, 148 (2005).

255. M. S. Wilson, Fuel cell with interdigitated porous flow-field, in, The Regents of the University of California Office of Technology Transfer, U.S. (1995).

256. W. He, J. S. Yi and T. V. Nguyen, *AIChE J.*, 46, 2053 (2000).

257. J. S. Yi and T. V. Nguyen, *J. Electrochem. Soc.*, 146, 38 (1999).

258. J. P. Feser, A. K. Prasad and S. G. Advani, *J. Power Sources*, 161, 404 (2006).

259. J. Park and X. G. Li, *J. Power Sources*, 163, 853 (2007).

260. L. Wang and H. T. Liu, *J. Power Sources*, 134, 185 (2004).

261. W. M. Yan, H. Y. Li and W. C. Tsai, *J. Electrochem. Soc.*, 153, A1984 (2006).

262. J. J. Hwang, C. H. Chao, W. Y. Ho, C. L. Chang and D. Y. Wang, *J. Power Sources*, 157, 85 (2006).

263. S. Um and C. Y. Wang, *J. Power Sources*, 125, 40 (2004).

264. H. Yamada, T. Hatanaka, H. Murata and Y. Morimoto, *J. Electrochem. Soc.*, 153, A1748 (2006).

265. J. Zou, X. F. Peng and W. M. Yan, *J. Power Sources*, 159, 514 (2006).

266. E. Arato, M. Pinna and P. Costa, *J. Power Sources*, 158, 206 (2006).

267. E. Arato and P. Costa, *J. Power Sources*, 158, 200 (2006).

268. G. Inoue, Y. Matsukuma and M. Minemoto, *J. Power Sources*, 157, 136 (2006).

269. K. V. Zhukovsky, *AIChE J.*, 49, 3029 (2003).

270. A. Kazim, H. T. Liu and P. Forges, *J. Appl. Electrochem.*, 29, 1409 (1999).

271. C. Reiser, Ion Exchange Membrane Fuel Cell Power Plant with Water Managament Pressure Differentials, in, UTC Fuel Cells, United States (1997).

272. A. Z. Weber and R. M. Darling, *J. Power Sources*, 168, 191 (2007).

273. D. L. Wood, Y. S. Yi and T. V. Nguyen, *Electrochim. Acta*, 43, 3795 (1998).

274. T. Yang and P. Shi, *J. Electrochem. Soc.*, 153, A1518 (2006).

275. S. H. Ge, X. G. Li and I. M. Hsing, *J. Electrochem. Soc.*, 151, B523 (2004).

276. S. H. Ge, X. G. Li and I. M. Hsing, *Electrochim. Acta*, 50, 1909 (2005).

277. C. R. Buie, J. D. Posner, T. Fabian, C. A. Suk-Won, D. Kim, F. B. Prinz, J. K. Eaton and J. G. Santiago, *J. Power Sources*, 161, 191 (2006).

278. J. P. Meyers, R. M. Darling, C. Evans, R. Balliet and M. L. Perry, *ECS Transactions*, 3, 1207 (2006).

279. S. Litster, J. G. Pharoah, G. McLean and N. Djilali, *J. Power Sources*, 156, 334 (2006).

280. J. J. Hwang, S. D. Wu, R. G. Pen, P. Y. Chen and C. H. Chao, *J. Power Sources*, 160, 18 (2006).

281. S. Litster and N. Djilali, *Electrochim. Acta*, 52, 3849 (2007).

282. Hydrogen, fuel cells & infrastructure technologies program; multi-year research, development and demonstration plan, Tables 3.4.2 and 3.4.3., in, p. 14, U.S. Department of Energy (2007).

283. F. Mueller, J. Brouwer, S. G. Kang, H. S. Kim and K. D. Min, *J. Power Sources*, 163, 814 (2007).

284. W. S. He, G. Y. Lin and T. V. Nguyen, *AIChE J.*, 49, 3221 (2003).

285. R. Mosdale, G. Gebel and M. Pineri, *J. Membr. Sci.*, 118, 269 (1996).

286. A. Haddad, R. Bouyekhf, A. El Moudni and M. Wack, *J. Power Sources*, 163, 420 (2006).

287. W. Friede, S. Rael and B. Davat, *Ieee Transactions on Power Electronics*, 19, 1234 (2004).

288. H. M. Yu and C. Ziegler, *J. Electrochem. Soc.*, 153, A570 (2006).

289. F. L. Chen, M. H. Chang and C. F. Fang, *J. Power Sources*, 164, 649 (2007).

290. A. Vorobev, O. Zikanov and T. Shamim, *J. Power Sources*, 166, 92 (2007).

291. I. Nazarov and K. Promislow, *Chem. Eng. Sci.*, 61, 3198 (2006).

292. J. Benziger, E. Chia, J. F. Moxley and I. G. Kevrekidis, *Chem. Eng. Sci.*, 60, 1743 (2005).

293. R. M. Rao and R. Rengaswamy, *Chem. Eng. Sci.*, 61, 7393 (2006).

294. W. M. Yan, C. Y. Soong, F. L. Chen and H. S. Chu, *J. Power Sources*, 143, 48 (2005).

295. S. Shimpalee, W. K. Lee, J. W. Van Zee and H. Naseri-Neshat, *J. Power Sources*, 156, 355 (2006).

296. Y. Wang and C. Y. Wang, *Electrochim. Acta*, 50, 1307 (2005).

297. Y. Wang and C. Y. Wang, *Electrochim. Acta*, 51, 3924 (2006).

298. J. C. Amphlett, R. F. Mann, B. A. Peppley, P. R. Roberge and A. Rodrigues, *J. Power Sources*, 61, 183 (1996).

299. F. L. Chen, Y. G. Su, C. Y. Soong, W. M. Yan and H. S. Chu, *J. Electronanal. Chem.*, 566, 85 (2004).

300. Y. Shan and S. Y. Choe, *J. Power Sources*, 158, 274 (2006).

301. H. Wu, P. Berg and X. G. Li, *J. Power Sources*, 165, 232 (2007).

302. T. F. Fuller and J. Newman, *J. Electrochem. Soc.*, 140, 1218 (1993).

303. Y. Y. Shan, S. Y. Choe and S. H. Choi, *J. Power Sources*, 165, 196 (2007).

304. D. Natarajan and T. V. Nguyen, *J. Power Sources*, 115, 66 (2003).

305. C. Ziegler, H. M. Yu and J. O. Schumacher, *J. Electrochem. Soc.*, 152, A1555 (2005).

306. S. M. Chang and H. S. Chu, *J. Power Sources*, 161, 1161 (2006).

307. D. T. Song, Q. P. Wang, Z. S. Liu and C. Huang, *J. Power Sources*, 159, 928 (2006).

308. H. Guilin and F. Jianren, *J. Power Sources*, 165, 171 (2007).

309. S. Shimpalee, D. Spuckler and J. W. Van Zee, *J. Power Sources*, 167, 130 (2007).

310. A. A. Pesaran, G.-H. Kim and J. D. Gonder, *NREL*, MP-540-38760 (2005).

311. M. F. Mathias, R. Makharia, H. A. Gasteiger, Jason J. Conley, T. J. Fuller, C. J. Gittleman, S. S. Kocha, Daniel P. Miller, C. K. Mittelsteadt, T. Xie, S. G. Yan and P. T. Yu, *The Electrochemical Society Interface*, 14, 24 (2005).

312. R. Bradean, H. Haas, K. Eggen, C. Richards and T. Vrba, *ECS Transactions*, 3, 1159 (2006).

313. M. Modell and R. C. Reid, *Thermodynamics and its Applications*, Prentice-Hall (1974).

314. S. Taber, *J. Geol.*, 38, 303 (1930).

315. J. D. Sage and M. Porebska, *Journal of Cold Regions Engineering*, 7, 99 (1993).

316. R. D. Miller, *Proceedings of the Third International Conference on Permafrost*, 707 (1978).

317. J. P. G. Loch, *Soil Science*, 126, 77 (1978).

318. A. W. Rempel, J. S. Wettlaufer and M. G. Worster, *J. Fluid Mech.*, 498, 227 (2004).

319. K. S. Henry, A review of the thermodynamics of frost heave, in, H. US Army Cold Regions Research and Engineering Laboratory, NH, report TR-00-16 Editor, p. 1 (2000).

320. S. H. He and M. M. Mench, *J. Electrochem. Soc.*, 153, A1724 (2006).

321. S. He and M. M. Mench, *ECS Transactions*, 3, 897 (2006).

322. E. L. Thompson, T. W. Capehart, T. J. Fuller and J. Jorne, *J. Electrochem. Soc.*, 153, A2351 (2006).

323. E. L. Thompson, J. Jorne and H. A. Gasteiger, *J. Electrochem. Soc.*, 154, B783 (2007).

324. M. De Francesco and E. Arato, *J. Power Sources*, 108, 41 (2002).

325. M. Sundaresan and R. M. Moore, *Fuel Cells*, 5, 476 (2005).

326. M. Sundaresan and R. M. Moore, *J. Power Sources*, 145, 534 (2005).

327. M. Oszcipok, A. Hakenjos, D. Riemann and C. Hebling, *Fuel Cells*, 7, 135 (2007).

328. Y. Hishinuma, T. Chikahisa, F. Kagami and T. Ogawa, *Jsme International Journal Series B-Fluids and Thermal Engineering*, 47, 235 (2004).

329. L. Mao and C. Y. Wang, *J. Electrochem. Soc.*, 154, B139 (2007).

330. L. Mao and C. Y. Wang, *J. Electrochem. Soc.*, 154, B341 (2007).

331. H. A. Gasteiger and M. F. Mathias, in *Proton Conducting Membrane Fuel Cells III*, J. W. Van Zee, T. F. Fuller, S. Gottesfeld and M. Murthy Editors, The Electrochemical Society Proceeding Series, Pennington, NJ (2002).

332. J. L. Zhang, Z. Xie, J. J. Zhang, Y. H. Tanga, C. J. Song, T. Navessin, Z. Q. Shi, D. T. Song, H. J. Wang, D. P. Wilkinson, Z. S. Liu and S. Holdcroft, *J. Power Sources*, 160, 872 (2006).

333. C. Yang, P. Costamagna, S. Srinivasan, J. Benziger and A. B. Bocarsly, *J. Power Sources*, 103, 1 (2001).

334. Y. Y. Shao, G. P. Yin, Z. B. Wang and Y. Z. Gao, *J. Power Sources*, 167, 235 (2007).

335. T. M. Thampan, N. H. Jalani, P. Choi and R. Datta, *J. Electrochem. Soc.*, 152, A316 (2005).

336. F. A. De Bruijn, R. C. Makkus, R. K. A. M. Mallant and G. J. M. Janssen, in *Advances in Fuel Cells, Vol. 1*, T. S. Zhao, K.-D. Kreuer and T. V. Nguyen Editors, Elsevier, Amsterdam (2007).

337. R. C. Jiang, H. R. Kunz and J. M. Fenton, *J. Electrochem. Soc.*, 152, A1329 (2005).

338. J. Peng and S. J. Lee, *J. Power Sources*, 162, 1182 (2006).

339. D. F. Cheddie and N. D. H. Munroe, *J. Power Sources*, 160, 215 (2006).

340. D. F. Cheddie and N. D. H. Munroe, *Int. J. Hydrog. Energy*, 32, 832 (2007).

341. J. W. Hu, H. M. Zhang, Y. F. Zhai, G. Liu, J. Hu and B. L. Yi, *Electrochim. Acta*, 52, 394 (2006).

342. P. K. Sinha, C. Y. Wang and U. Beuscher, *J. Electrochem. Soc.*, 154, B106 (2007).

343. P. K. Sinha, C. Y. Wang and A. Su, *Int. J. Hydrog. Energy*, 32, 886 (2007).

344. J. L. Zhang, Y. H. Tang, C. J. Song, X. A. Cheng, J. J. Zhang and H. J. Wang, *Electrochim. Acta*, 52, 5095 (2007).

345. H. Xu, H. R. Kunz and J. M. Fenton, *Electrochim. Acta*, 52, 3525 (2007).

346. Y. Song, J. M. Fenton, H. R. Kunz, L. J. Bonville and M. V. Williams, *J. Electrochem. Soc.*, 152, A539 (2005).

347. Y. H. Tang, J. J. Zhang, C. J. Song, H. Liu, J. L. Zhang, H. J. Wang, S. Mackinnon, T. Peckham, J. Li, S. McDermid and P. Kozak, *J. Electrochem. Soc.*, 153, A2036 (2006).

348. J. S. Wainright, J. T. Wang, D. Weng, R. F. Savinell and M. Litt, *J. Electrochem. Soc.*, 142, L121 (1995).

349. J. T. Wang, R. F. Savinell, J. Wainright, M. Litt and H. Yu, *Electrochim. Acta*, 41, 193 (1996).

350. S. von Kraemer, M. Puchner, P. Jannasch, A. Lundblad and G. Lindbergh, *J. Electrochem. Soc.*, 153, A2077 (2006).

351. L. J. Bonville, H. R. Kunz, Y. Song, A. Mientek, M. Williams, A. Ching and J. M. Fenton, *J. Power Sources*, 144, 107 (2005).

352. B. S. Pivovar and Y. S. Kim, *J. Electrochem. Soc.*, 154, B739 (2007).

353. H. Xu, Y. Song, H. R. Kunz and J. M. Fenton, *J. Electrochem. Soc.*, 152, A1828 (2005).

354. C. J. Song, Y. H. Tang, J. L. Zhang, J. J. Zhang, H. J. Wang, J. Shen, S. McDermid, J. Li and P. Kozak, *Electrochim. Acta*, 52, 2552 (2007).

355. L. Xiao, H. Zhang, T. Jana, E. Scanlon, R. Chen, E. W. Choe, L. S. Ramanathan, S. Yu and B. C. Benicewicz, *Fuel Cells*, 5, 287 (2005).

356. S. Srinivasan, *Fuel Cells. From Fundamentals to Applications*, Springer, New York (2006).

Captions

Table 1. Summary of time-constant analysis.

Figure 1. 3-D fuel-cell schematic showing the different layers in the PEFC sandwich or through-plane direction.

Figure 2. Schematic of a polarization curve showing the typical losses in a PEFC. The curve demonstrates a severe onset of flooding at high current densities.

Figure 3. Experimental data showing water-management impacts on performance. (a) Neutron image of water thickness at 60°C, 1 A/cm^2, saturated inlet gases. (b) Cell performance and area-specific resistance as a function of humidifier temperature; the cell temperature is 80°C and the humidifier temperatures correspond to inlet relative humidities of 33, 53, 81, and 122 %, respectively. (Figure (a) is courtesy of Dr. Michael Hickner, and figure (b) is adapted from reference [1] with permission of Elsevier)

Figure 4. Schematic showing the different model dimensionalities. 0-D models are simple equations and are not shown, the 1-D models comprise the sandwich (z direction), the 2-D models comprise the 1-D sandwich and either of the two other coordinate directions (x or y), and the 3-D comprise all three coordinate directions.

Figure 5. Simulated net membrane water as a function of current density for an unconstrained and a constrained membrane with a liquid-equilibrated cathode and a vapor-

equilibrated anode. (The figure is adapted from reference [77] with permission of The Electrochemical Society, Inc.)

Figure 6. Liquid- and gas-phase pressure as a function of average liquid saturation and saturated (absolute) permeability for a 0.25 cm cathode GDL, a gas-channel pressure of 1 bar, and conditions of 1 A/cm^2 and 65°C.

Figure 7. Idealized schematic of the cathode catalyst layer (going from $z = 0$ to $z = L$) between the membrane and cathode diffusion medium showing the two main length scales: the agglomerate and the entire porous-electrode. Grey, white, and black indicate membrane, gas, and electrocatalyst, respectively, and the grey region outside of the dotted line in the agglomerate represents an external film of membrane or water on top of the agglomerate.

Figure 8. Simple equivalent-circuit representation of a porous electrode. The total current density, *i*, flows through the membrane and then the electrolyte phase (2) and the solid phase (1) and a contact resistance at each respective end. In between, the current is apportioned based on the resistances in each phase and the charge-transfer resistances and double-layer charging. The charge-transfer resistances can be nonlinear because they are based on kinetic expressions.

Figure 9. Depiction of (a) capillary-tree and (b) channeling mechanisms of water movement through a GDL. (Figure (a) is from reference [86] and (b) is from reference [23] with permission of Elsevier)

Figure 10. Imaging and correlation of penetration events in a mixed-wettability system and corresponding changes in capillary pressure. (The figure is reproduced from reference [174] with permission of the American Institute of Physics)

Figure 11. Simulations of a PEFC with and without a MPL. Also given are the membrane net-water-flux-per-proton-flux results. The various PEFC sandwich layers are noted, and the curves correspond to changes in potential going from 1 to 0.4 V in 50 mV increments. The simulation was at 60°C, saturated feed gases. (The figure is reproduced from reference [196] with permission of The Electrochemical Society, Inc.)

Figure 12. Schematic representation of a heat pipe on the cathode side of a PEFC. Water is evaporated in the CL, moves in the vapor phase, and condenses down the temperature (vapor-pressure) gradient.

Figure 13. 2-D liquid saturation contours near the gas-inlet region for the case where the heat-pipe effect is neglected (a) and considered (b). The inlet gases are fed saturated at 80°C, and the current density is around 1.3 A/cm^2. (The figure is reproduced from reference [203] with permission of The Electrochemical Society, Inc.)

Figure 14. Current-density distribution at 0.65 V with saturated air at the cathode CL / GDL interface as a function of GDL in-plane dimensions using anisotropic (a) gas diffusivities or (b) electronic conductivity. (The figure is adapted from reference [205] with permission of Elsevier)

Figure 15. Liquid saturation profiles at 0.6 V with 80°C, fully humidified feeds for (a) anisotropic and (b) isotropic GDL properties. The dashed lines on the right

correspond to the flow-field rib, and the solid lines correspond to the liquid front. (The figure is reproduced from reference [206] with permission of The Electrochemical Society, Inc.)

Figure 16. Distributions at 0.3 V of (a) oxygen mole fraction and (b) liquid saturation with 0% compression ratio and (c) oxygen mole fraction and (d) liquid saturation with 50% compression ratio. (The figure is reproduced from reference [218] with permission of Elsevier)

Figure 17. Current-density distribution at the cathode CL along the channel as a function of GDL elasticity. The nominal clamping compression is 1.93 MPa. (The figure is reproduced from reference [217] with permission of Elsevier)

Figure 18. Surface contour plots at membrane-cathode interface for (a) temperature and (b) water content. (The figure is reproduced from reference [237] with permission of Elsevier)

Figure 19. Transparent-cell photographs of liquid-water distributions in an operating PEFC showing (a) droplet emergence and flow and (b) film and (c) slug flow. (The figure is reproduced from reference [19] with permission of The Electrochemical Society, Inc.)

Figure 20. Effects of cathode inlet relative humidity on the vapor-liquid interface location in the channel (above the dashed line) and GDL. (The figure is reproduced from reference [241] with permission of Elsevier.)

Figure 21. Water movement through three sets of flow channels at times (a) t=0.0006 s, (b) t=0.003 s, (c) t=0.048 s, and (d) t=0.075 s. (The figure is reproduced from reference [245] with permission of Elsevier)

Figure 22. Critical Reynolds number as a function of droplet aspect ratio for a droplet with a GDL contact length and Teflon amount of (a) 0.23 cm and 5 % and (b) 0.19 cm and 20 %, respectively. (The figure is reproduced from reference [243] with permission of Elsevier)

Figure 23. Comparison of measured (symbols) and calculated (lines) current densities for (a) coflow and (b and c) counterflow cells operated with dry hydrogen and humid air at 0.3 A/cm^2 and 0.5 A/cm^2. The temperature drops along the air path from 75 to 65°C in (a) and (b) while rising along the air path in (c). (The figure is reproduced from reference [236] with permission of The Electrochemical Society, Inc.)

Figure 24. Dynamic response of cell potential to a step change in current density. (The figure is reproduced from reference [297] with permission of Elsevier)

Figure 25. Comparison of simulation and experiment for a change in current density from 0.4 to 0.6 A/cm^2. (The figure is reproduced from reference [283] with permission of Elsevier)

Figure 26. Variation of oxygen mole fraction along the channel width at different times and cell potentials. (The figure is reproduced from reference [309] with permission of Elsevier)

Figure 27. Comparison of predicted transient behavior for a single-phase, isothermal model and a multiphase, nonisothermal model. (The figure is reproduced from reference [309] with permission of Elsevier)

Figure 28. The CL-membrane-CL water content along the length of the stack obtained from the model (continuous line) and experiment (dashed line) at the end of the stack natural cooling process. (The figure is reproduced from reference [312] with permission of The Electrochemical Society, Inc.)

Figure 29. Transient distribution of ice saturation with bipolar plates (a) or open channel (b) boundary conditions. (The figure is reproduced from reference [321] with permission of The Electrochemical Society, Inc.)

Figure 30. Comparison of simulation and experimental results for current density and ohmic membrane/contact resistance during cold sweep at −8 °C. (The figure is reproduced from reference [327] with permission of Wiley-VCH)

Figure 31. Ice-saturation evolution in the cathode CL. (The figure is reproduced from reference [329] with permission of The Electrochemical Society, Inc.)

Figure 32. Polarization and resistance curves at various operating temperatures with a fixed water-vapor feed of 100 % saturation at 80°C with a Nafion® 112 membrane. The curves therefore correspond to inlet RHs of 100, 70, and 35 %, respectively. (The figure is reproduced from reference [346] with permission of The Electrochemical Society, Inc.)

Table 1. Summary of time-constant analysis.

Process	**Governing Equation**	**Typical Value For Time Constant (s)**	**Reference**
Charging or discharging of the electrochemical double layer	$\delta_{CL}^2 aC\left(\frac{1}{\kappa}+\frac{1}{\sigma}\right)$	2.0×10^{-7}	296
Electrochemical reaction rate	N/A	1.0×10^{-3}	30
Species diffusion (gas phase)	$\frac{L_{GDL}^2}{D_{species}}$	0.05	290
Heat transfer	$\frac{L_{cell}^2}{\alpha_{cell}}$	2	N/A
Membrane hydration	$\frac{L_{Membrane}^2}{D_{w,mem}}$	10	290

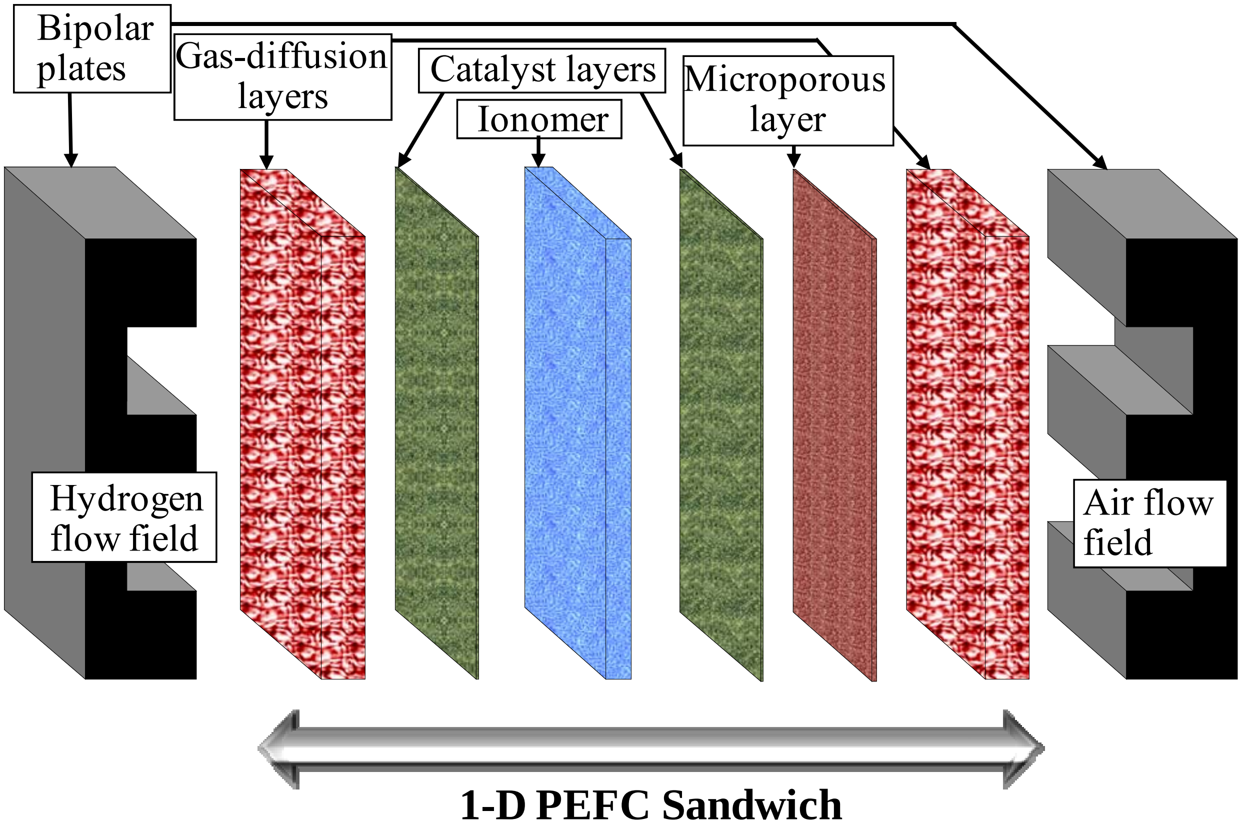

Figure 1. 3-D fuel-cell schematic showing the different layers in the PEFC sandwich or through-plane direction.

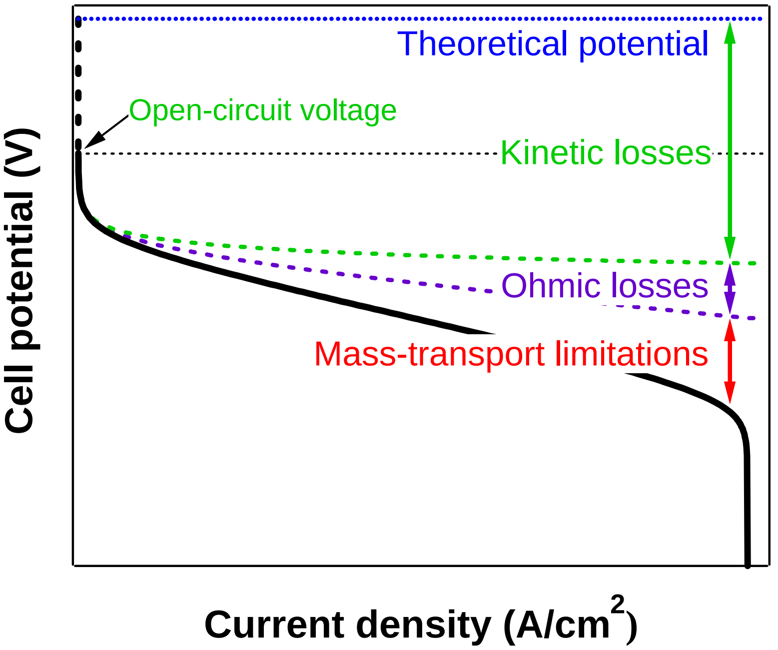

Figure 2. Schematic of a polarization curve showing the typical losses in a PEFC. The curve demonstrates a severe onset of flooding at high current densities.

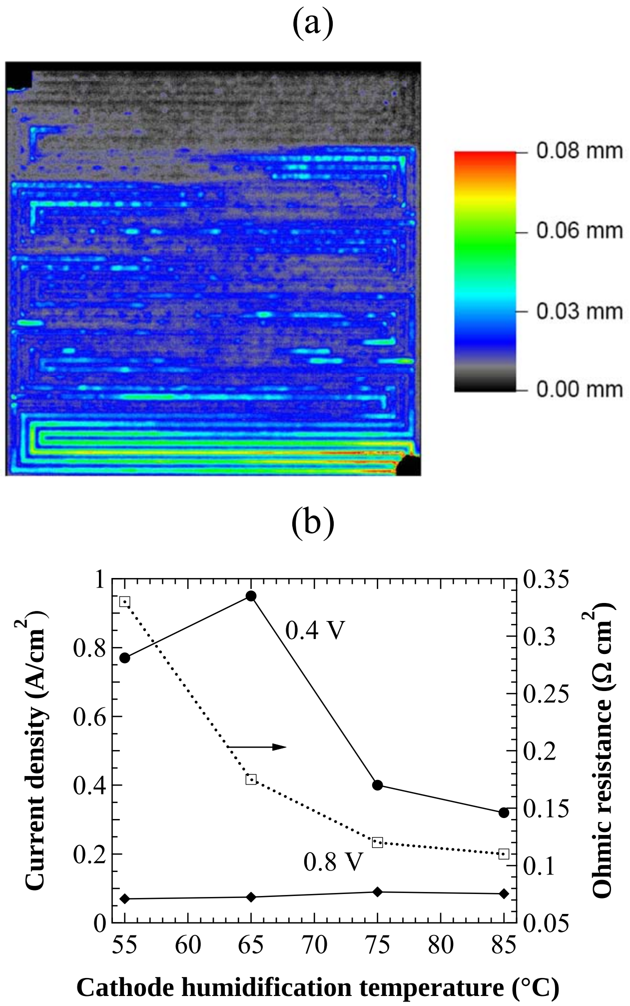

Figure 3. Experimental data showing water-management impacts on performance. (a) Neutron image of water thickness at 60°C, 1 A/cm^2, saturated inlet gases. (b) Cell performance and area-specific resistance as a function of humidifier temperature; the cell temperature is 80°C and the humidifier temperatures correspond to inlet relative humidities of 33, 53, 81, and 122 %, respectively. (Figure (a) is courtesy of Dr. Michael Hickner, and figure (b) is adapted from reference [1] with permission of Elsevier)

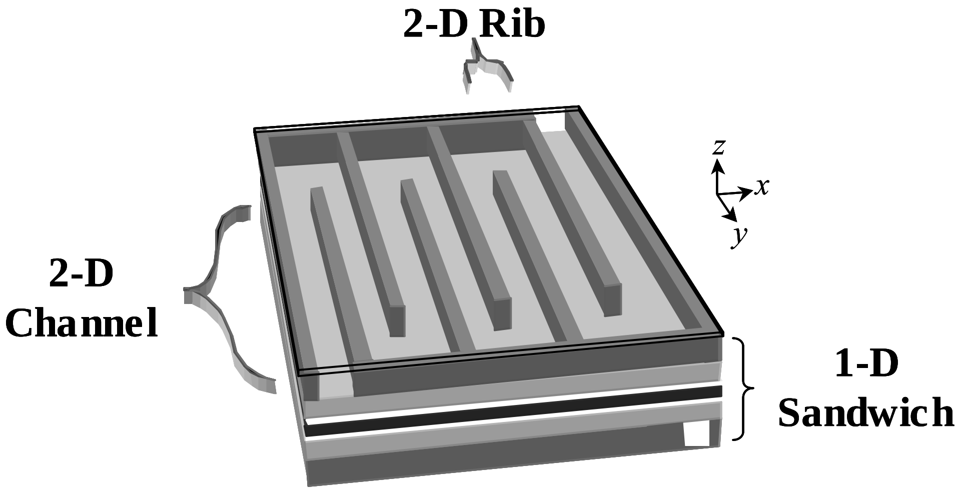

Figure 4. Schematic showing the different model dimensionalities. 0-D models are simple equations and are not shown, the 1-D models comprise the sandwich (*z* direction), the 2-D models comprise the 1-D sandwich and either of the two other coordinate directions (*x* or *y*), and the 3-D comprise all three coordinate directions.

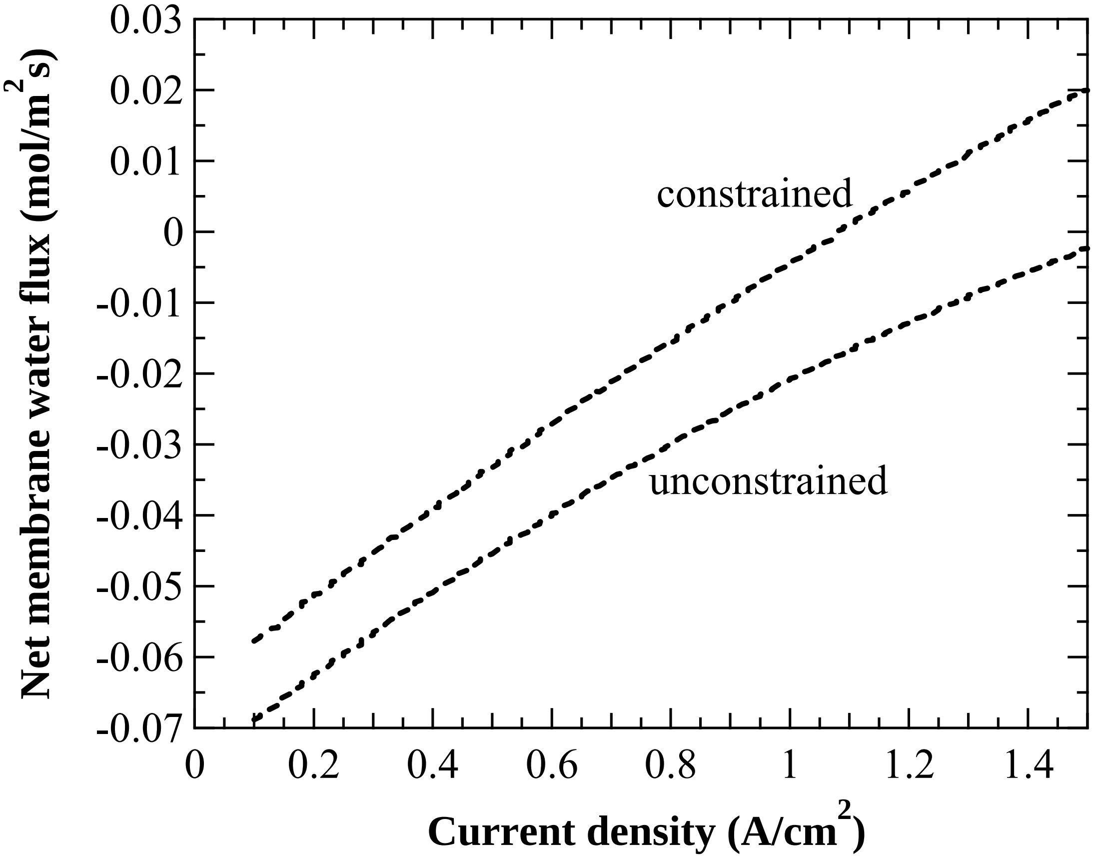

Figure 5. Simulated net membrane water as a function of current density for an unconstrained and a constrained membrane with a liquid-equilibrated cathode and a vapor-equilibrated anode.

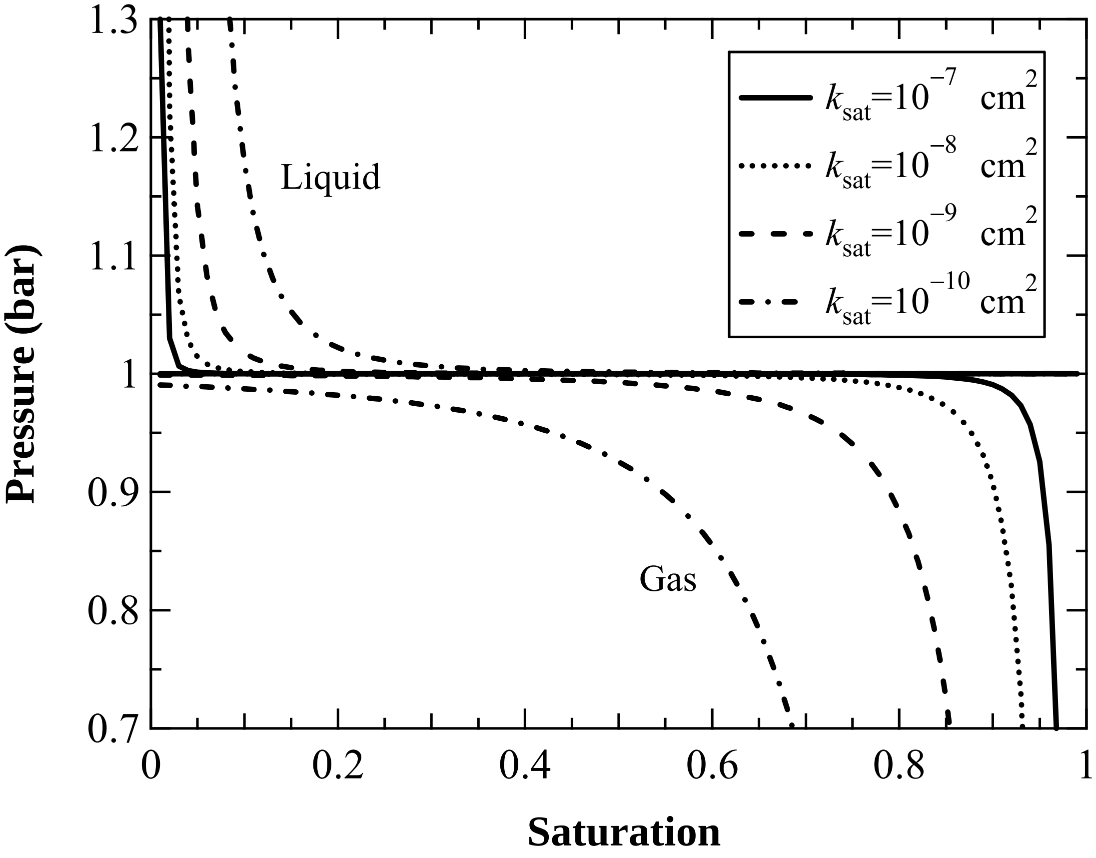

Figure 6. Liquid- and gas-phase pressure as a function of average liquid saturation and saturated (absolute) permeability for a 0.25 cm cathode GDL, a gas-channel pressure of 1 bar, and conditions of 1 A/cm^2 and 65°C.

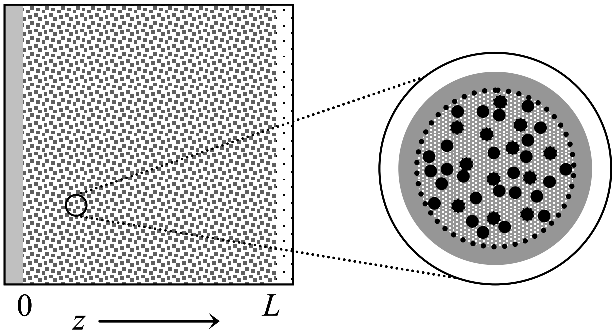

Figure 7. Idealized schematic of the cathode catalyst layer (going from $z = 0$ to $z = L$) between the membrane and cathode diffusion medium showing the two main length scales: the agglomerate and the entire porous-electrode. Grey, white, and black indicate membrane, gas, and electrocatalyst, respectively, and the grey region outside of the dotted line in the agglomerate represents an external film of membrane or water on top of the agglomerate.

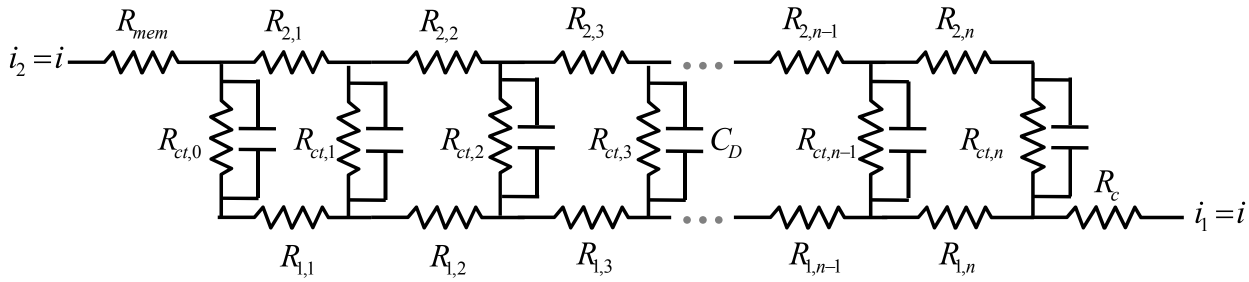

Figure 9. Depiction of (a) capillary-tree and (b) channeling mechanisms of water movement through a GDL. (Figure (a) is from reference [86] and (b) is from reference [23] with permission of Elsevier)

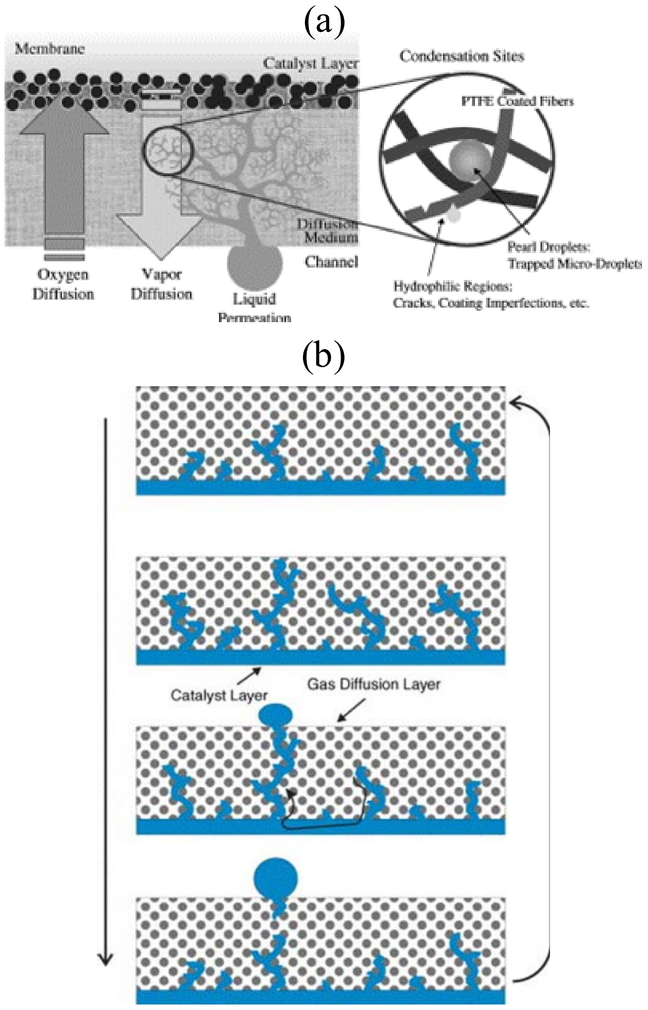

Figure 9. Depiction of (a) capillary-tree and (b) channeling mechanisms of water movement through a GDL. (Figure (a) is from reference [86] and (b) is from reference [23] with permission of Elsevier)

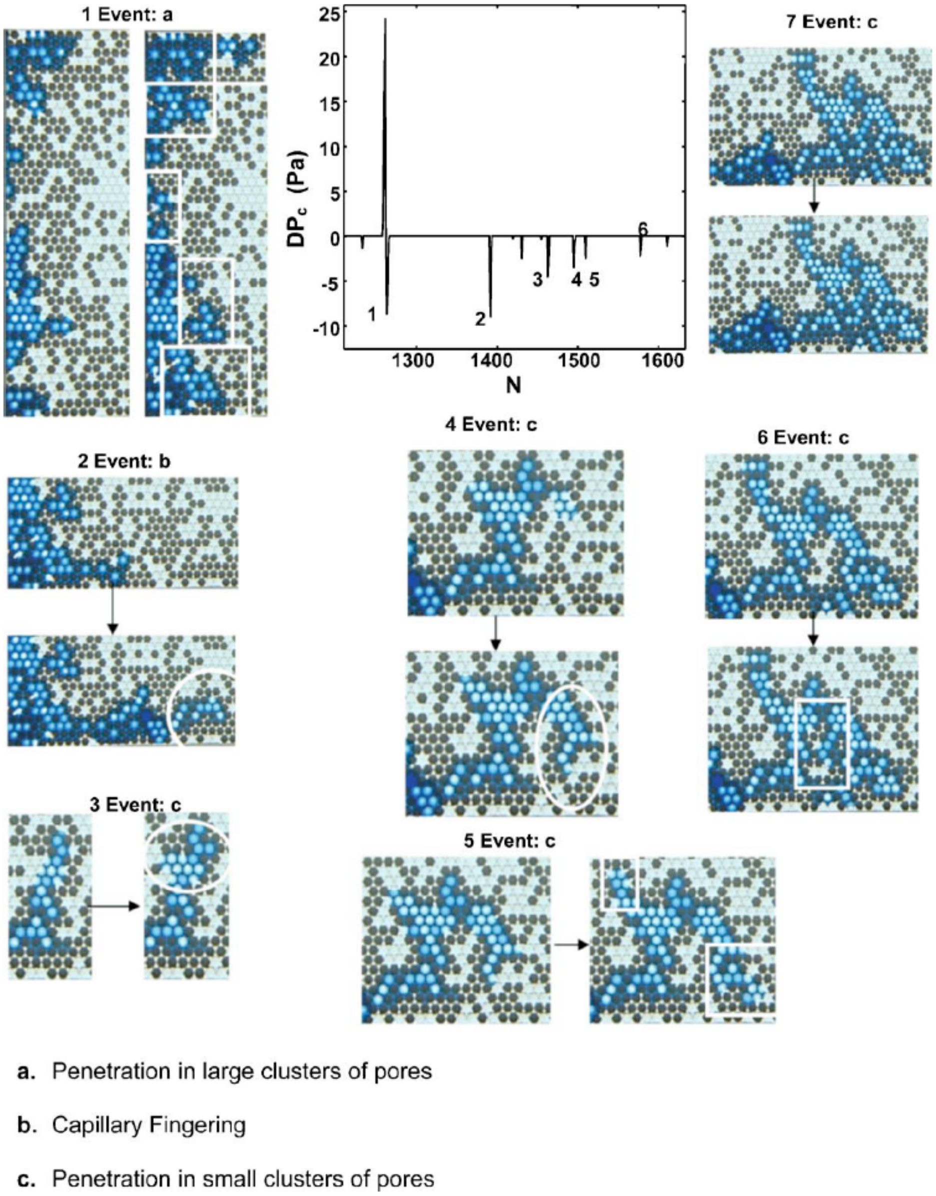

Figure 10. Imaging and correlation of penetration events in a mixed-wettability system and corresponding changes in capillary pressure. (The figure is reproduced from reference [174] with permission of the American Institute of Physics)

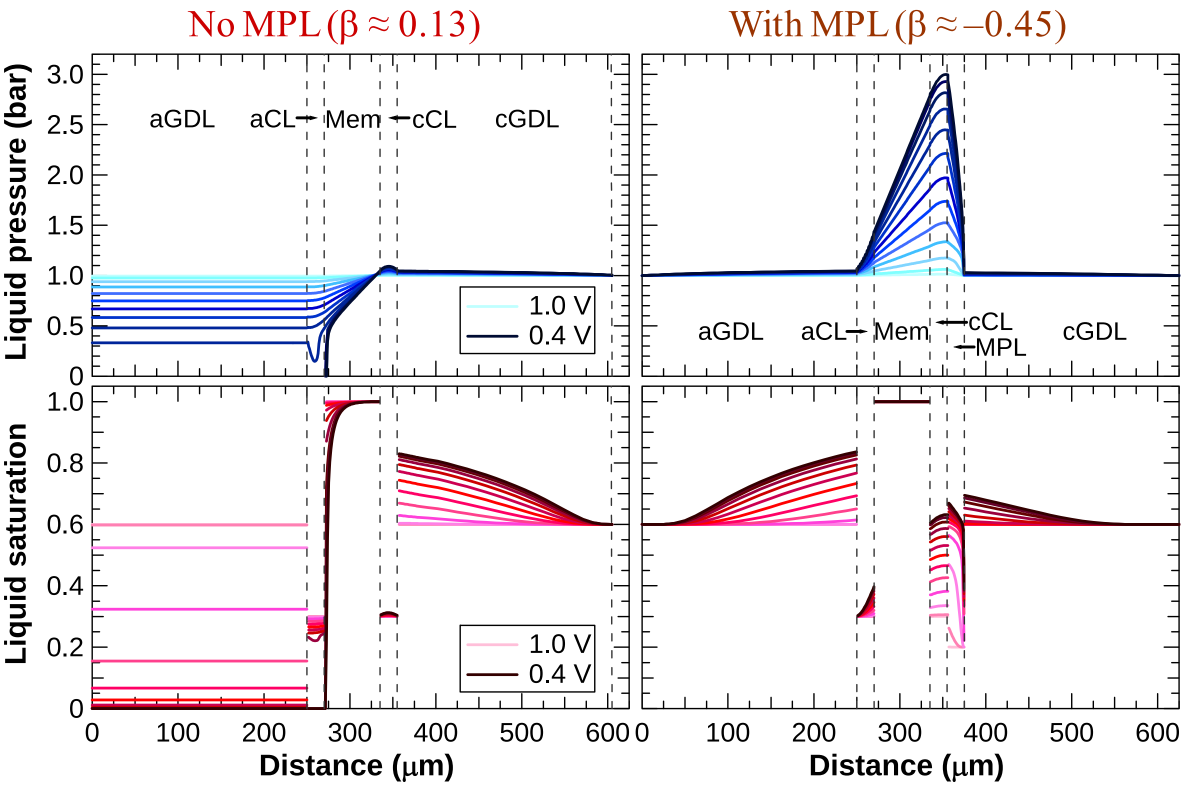

Figure 11. Simulations of a PEFC with and without a MPL. Also given are the membrane net-water-flux-per-proton-flux results. The various PEFC sandwich layers are noted, and the curves correspond to changes in potential going from 1 to 0.4 V in 50 mV increments. The simulation was at 60°C, saturated feed gases. (The figure is reproduced from reference [196] with permission of The Electrochemical Society, Inc

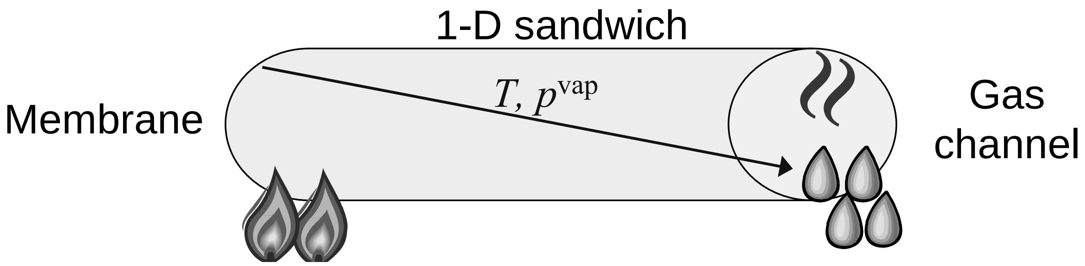

Figure 12. Schematic representation of a heat pipe on the cathode side of a PEFC. Water is evaporated in the CL, moves in the vapor phase, and condenses down the temperature (vapor-pressure) gradient.

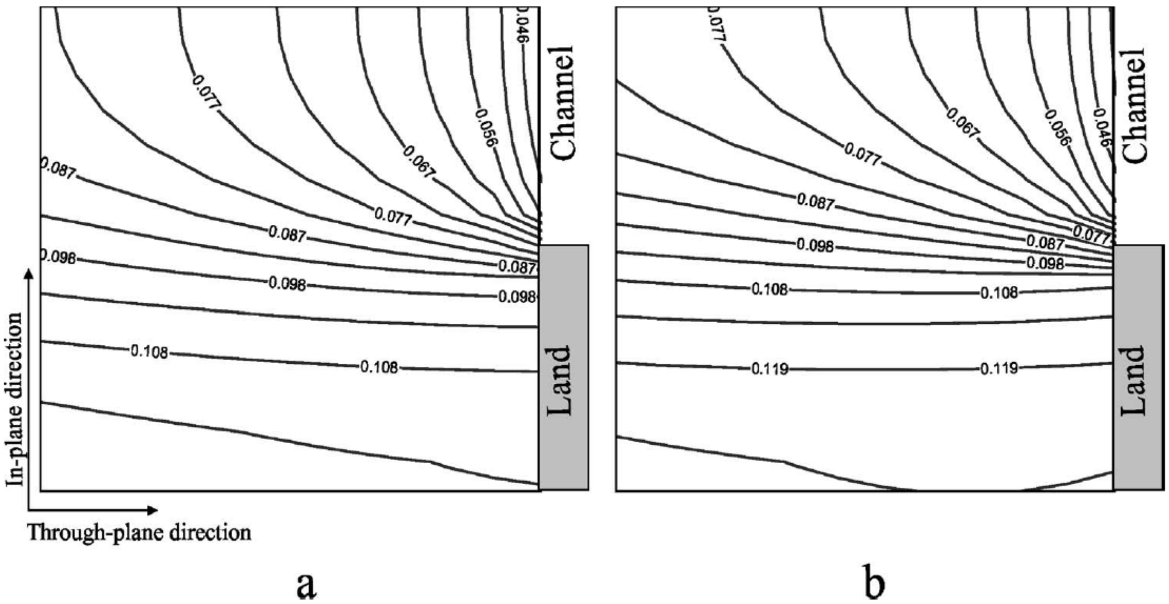

Figure 13. 2-D liquid saturation contours near the gas-inlet region for the case where the heat-pipe effect is neglected (a) and considered (b). The inlet gases are fed saturated at 80°C, and the current density is around 1.3 A/cm^2. (The figure is reproduced from reference [203] with permission of The Electrochemical Society, Inc.)

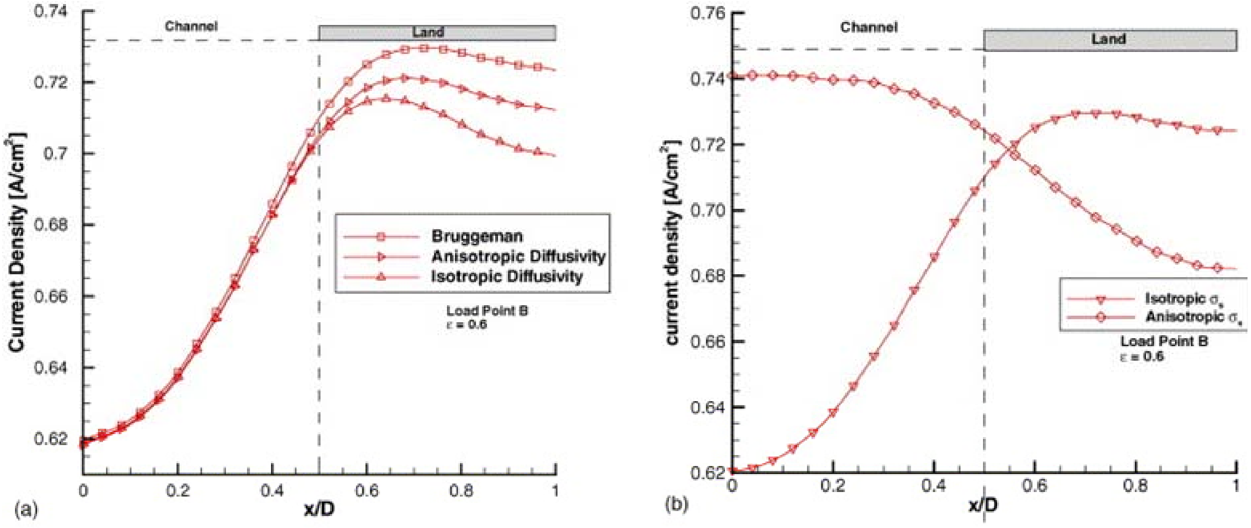

Figure 14. Current-density distribution at 0.65 V with saturated air at the cathode CL / GDL interface as a function of GDL in-plane dimensions using anisotropic (a) gas diffusivities or (b) electronic conductivity. (The figure is adapted from reference [205] with permission of Elsevier)

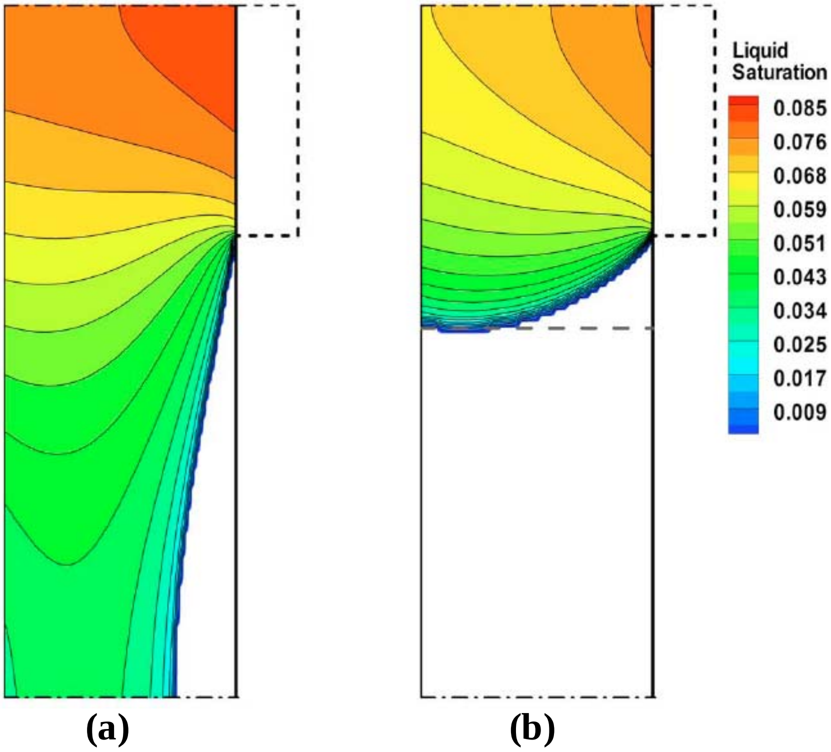

Figure 15. Liquid saturation profiles at 0.6 V with 80°C, fully humidified feeds for (a) anisotropic and (b) isotropic GDL properties. The dashed lines on the right correspond to the flow-field rib, and the solid lines correspond to the liquid front. (The figure is reproduced from reference [206] with permission of The Electrochemical Society, Inc.)

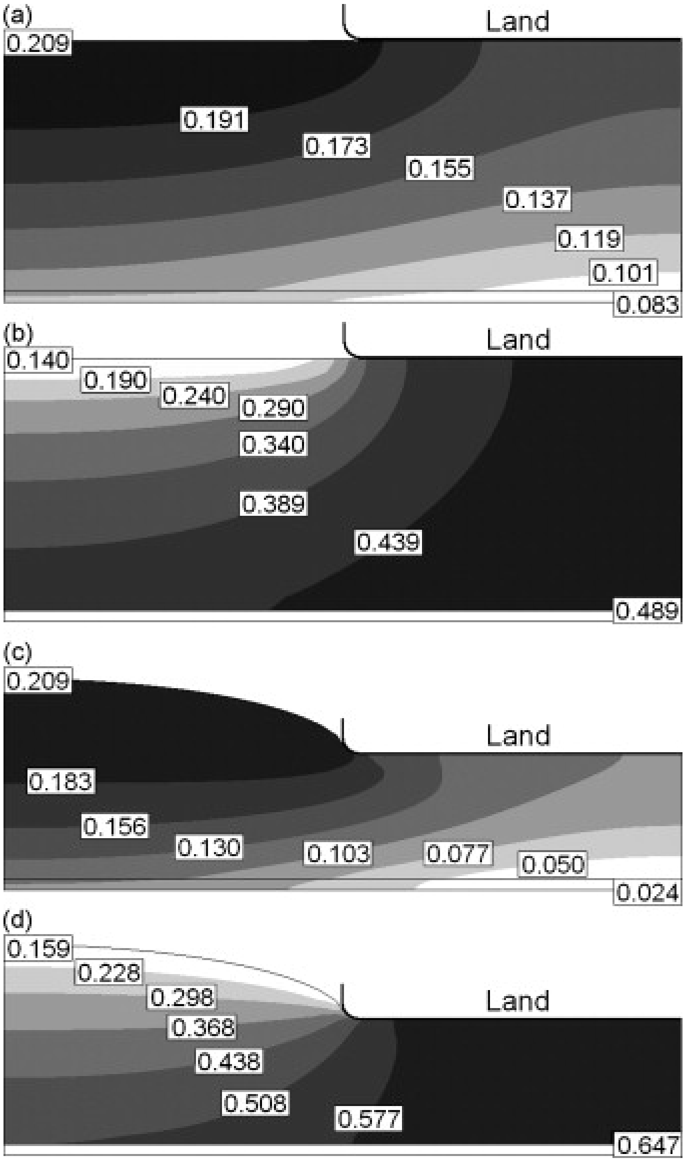

Figure 16. Distributions at 0.3 V of (a) oxygen mole fraction and (b) liquid saturation with 0% compression ratio and (c) oxygen mole fraction and (d) liquid saturation with 50% compression ratio. (The figure is reproduced from reference [218] with permission of Elsevier)

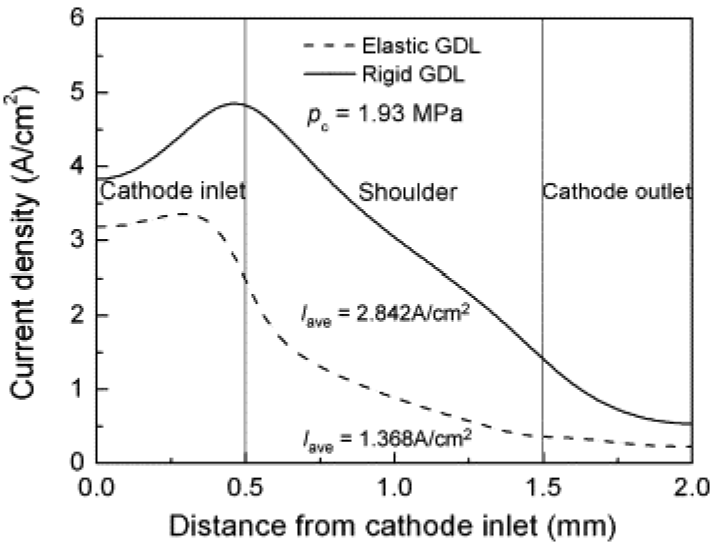

Figure 17. Current-density distribution at the cathode CL along the channel as a function of GDL elasticity. The nominal clamping compression is 1.93 MPa. (The figure is reproduced from reference [217] with permission of Elsevier)

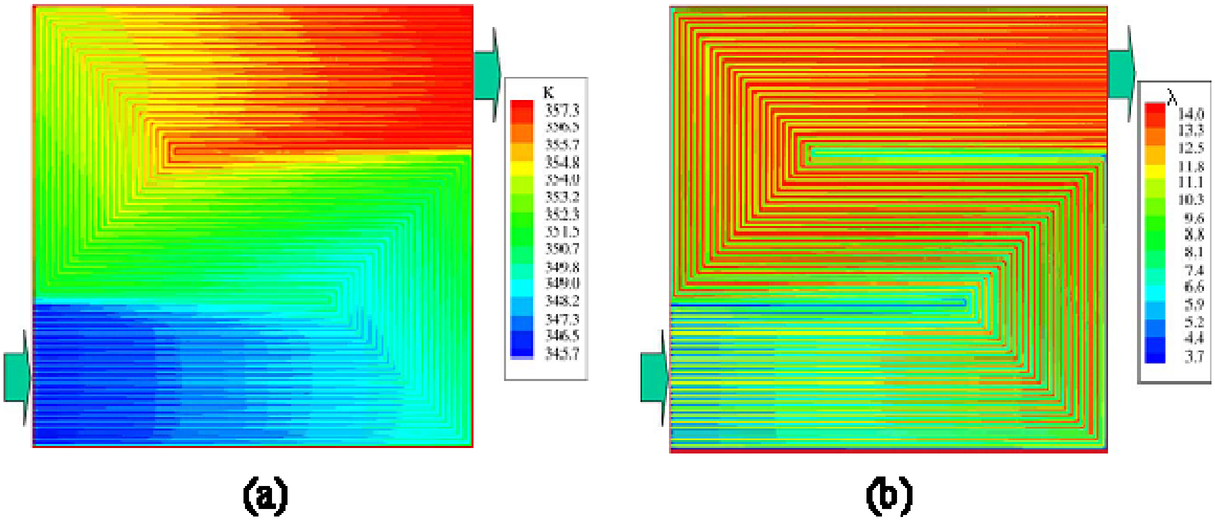

Figure 18. Surface contour plots at membrane-cathode interface for (a) temperature and (b) water content. (The figure is reproduced from reference [237] with permission of Elsevier)

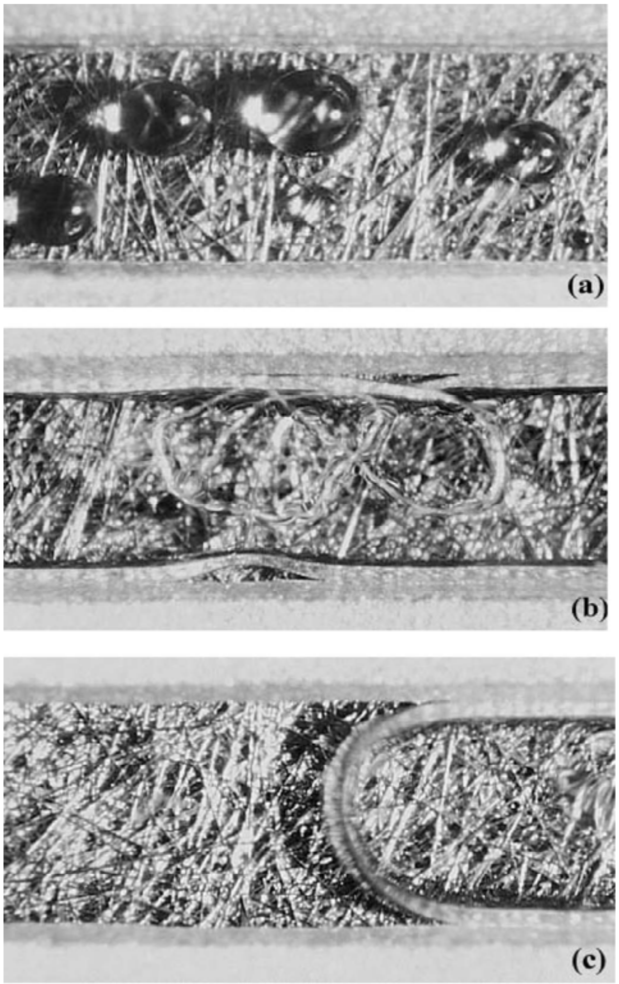

Figure 19. Transparent-cell photographs of liquid-water distributions in an operating PEFC showing (a) droplet emergence and flow and (b) film and (c) slug flow. (The figure is reproduced from reference [19] with permission of The Electrochemical Society, Inc.)

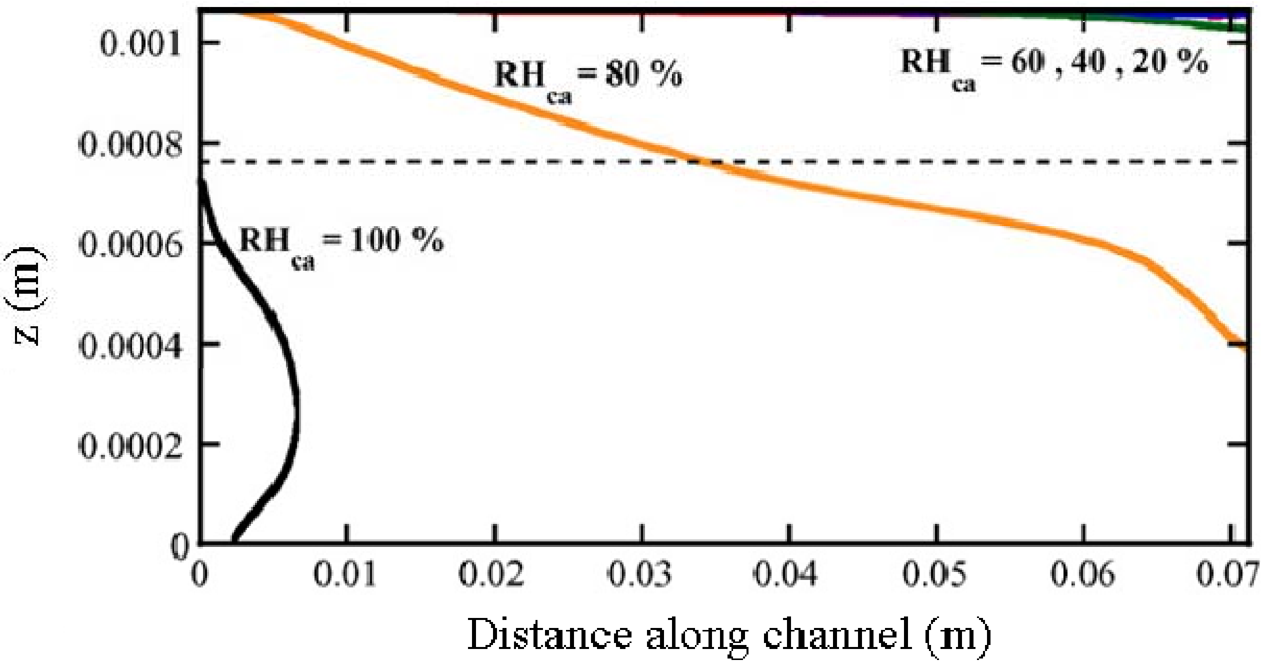

Figure 20. Effects of cathode inlet relative humidity on the vapor-liquid interface location in the channel (above the dashed line) and GDL. (The figure is reproduced from reference [241] with permission of Elsevier.)

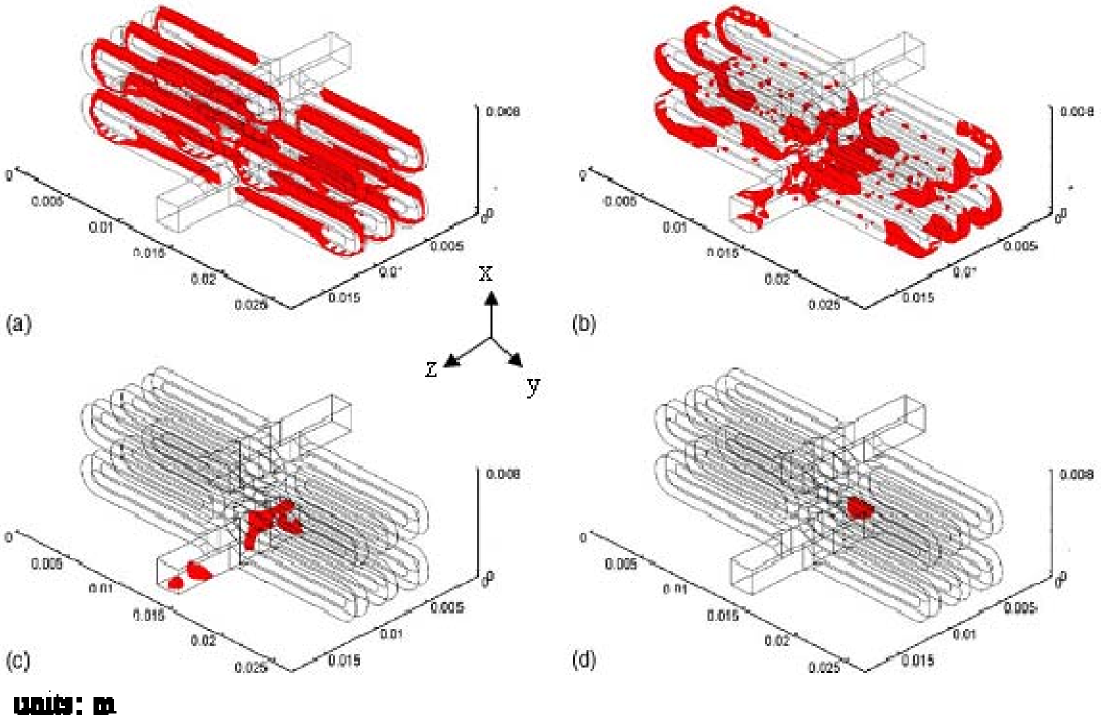

Figure 21. Water movement through three sets of flow channels at times (a) *t*=0.0006 s, (b) *t*=0.003 s, (c) *t*=0.048 s, and (d) *t*=0.075 s. (The figure is reproduced from reference [245] with permission of Elsevier)

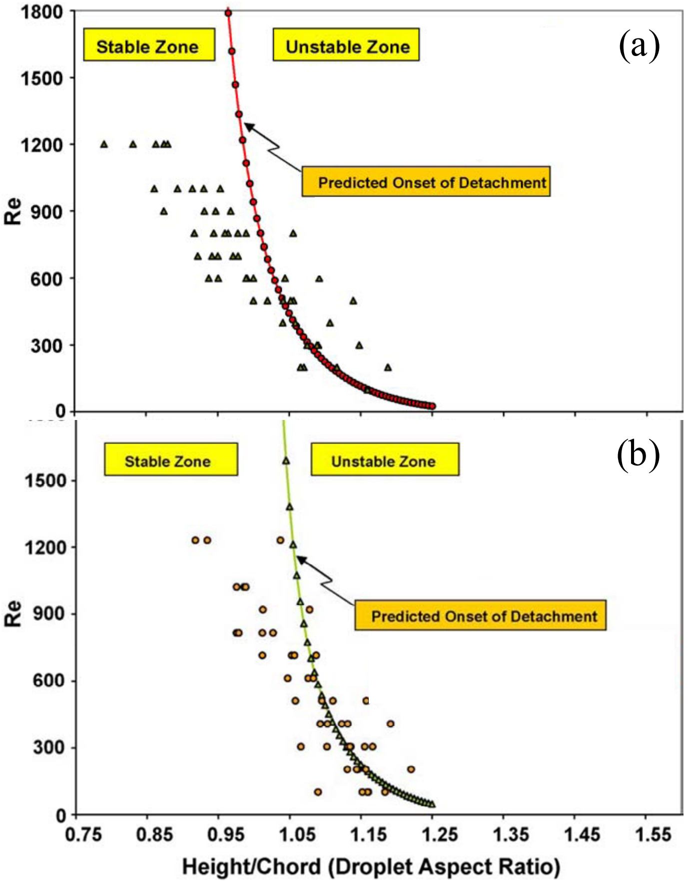

Figure 22. Critical Reynolds number as a function of droplet aspect ratio for a droplet with a GDL contact length and Teflon amount of (a) 0.23 cm and 5 % and (b) 0.19 cm and 20 %, respectively. (The figure is reproduced from reference [243] with permission of Elsevier)

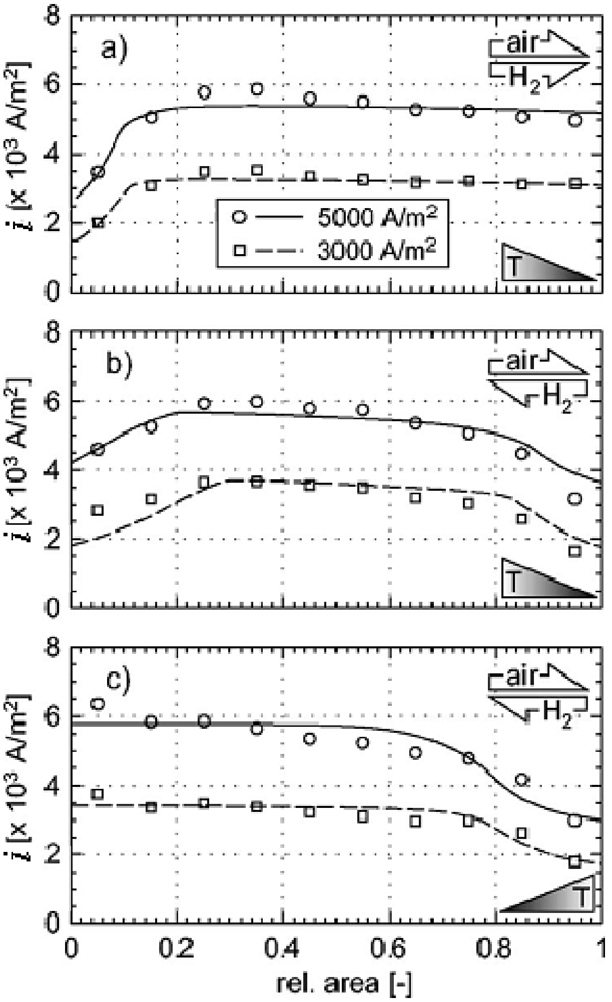

Figure 23. Comparison of measured (symbols) and calculated (lines) current densities for (a) coflow and (b and c) counterflow cells operated with dry hydrogen and humid air at 0.3 A/cm^2 and 0.5 A/cm^2. The temperature drops along the air path from 75 to 65°C in (a) and (b) while rising along the air path in (c). (The figure is reproduced from reference [236] with permission of The Electrochemical Society, Inc.)

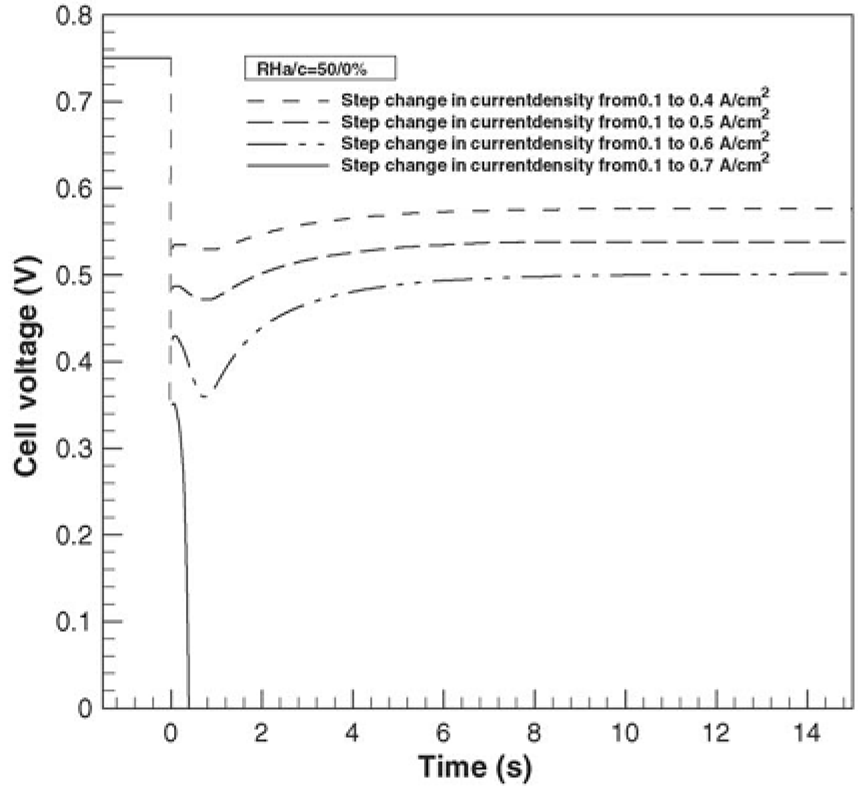

Figure 24. Dynamic response of cell potential to a step change in current density. (The figure is reproduced from reference [297] with permission of Elsevier)

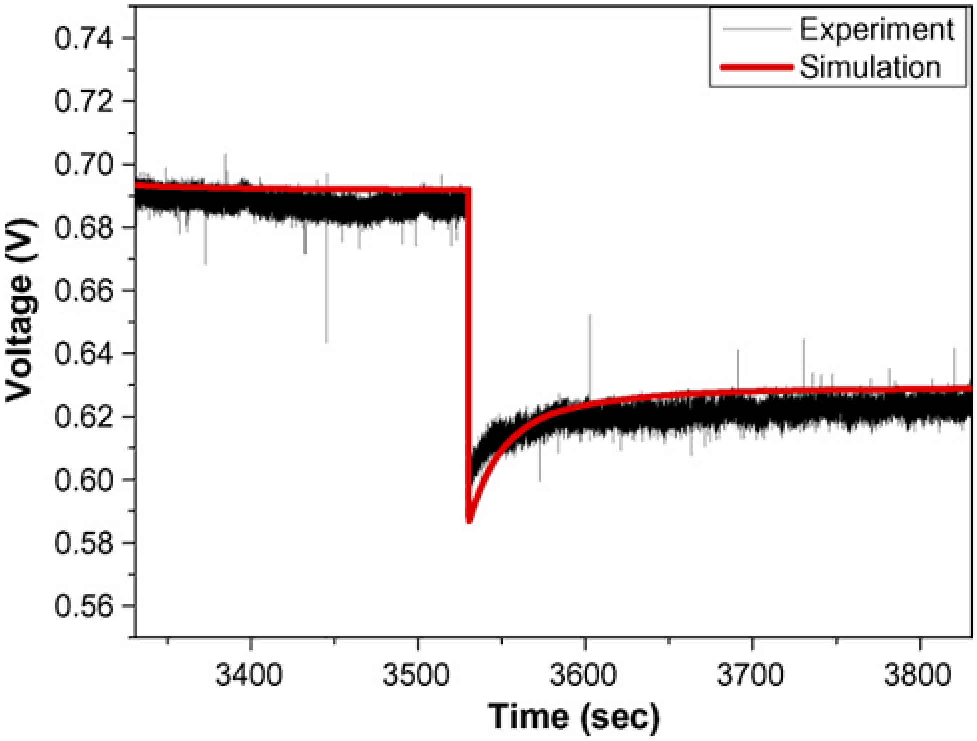

Figure 25. Comparison of simulation and experiment for a change in current density from 0.4 to 0.6 A/cm^2. (The figure is reproduced from reference [283] with permission of Elsevier)

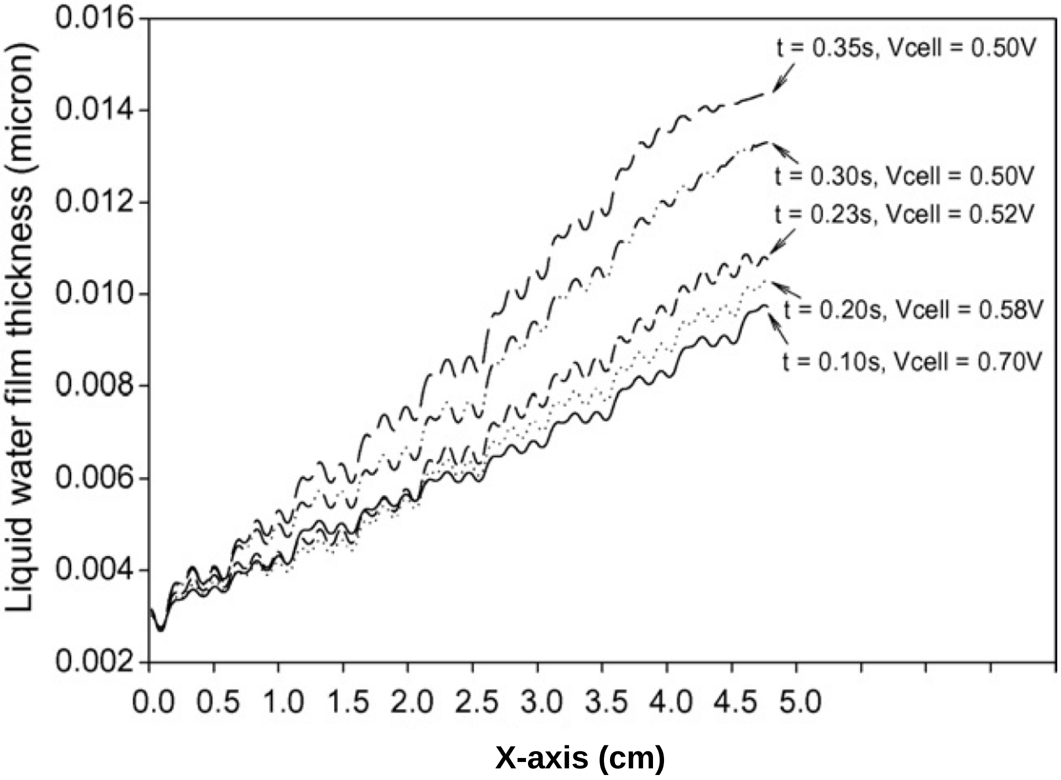

Figure 26. Variation of oxygen mole fraction along the channel width at different times and cell potentials. (The figure is reproduced from reference [309] with permission of Elsevier)

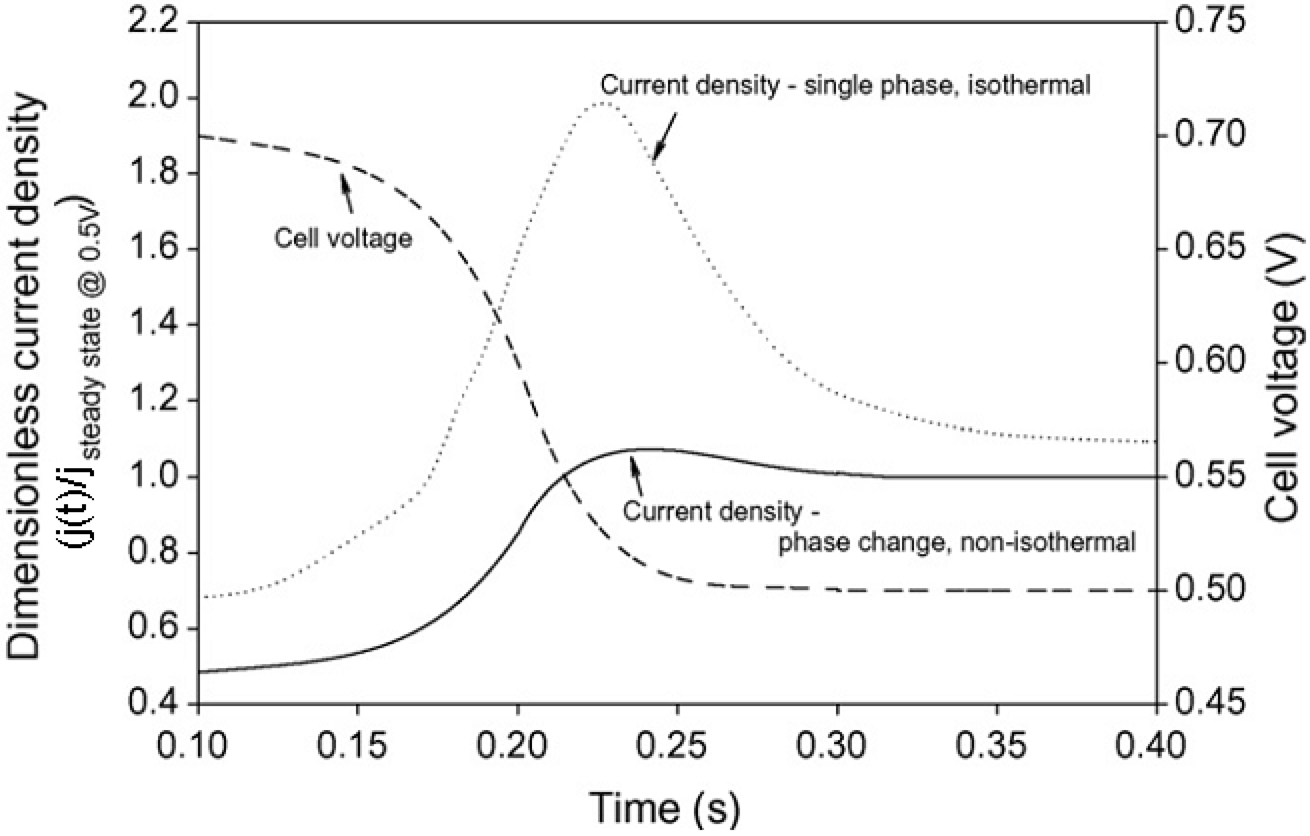

Figure 27. Comparison of predicted transient behavior for a single-phase, isothermal model and a multiphase, nonisothermal model. (The figure is reproduced from reference 309 with permission of Elsevier)

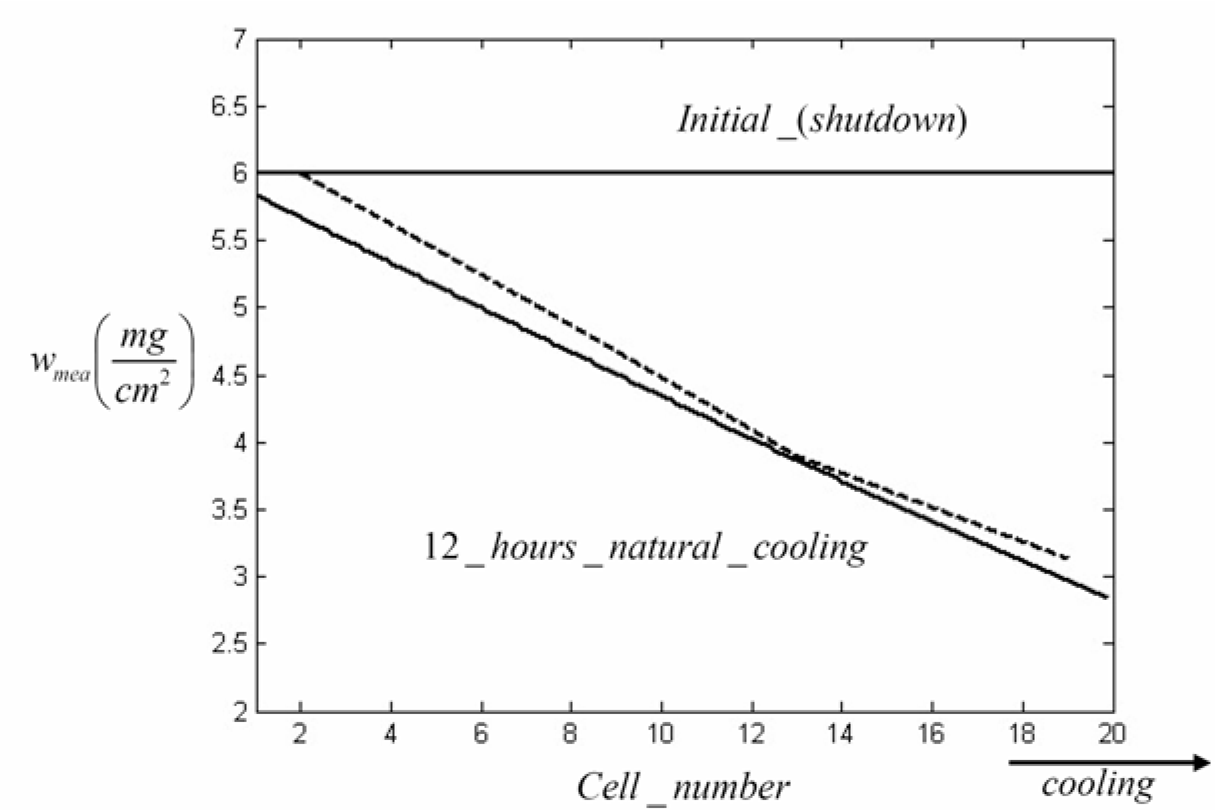

Figure 28. The CL-membrane-CL water content along the length of the stack obtained from the model (continuous line) and experiment (dashed line) at the end of the stack natural cooling process. (The figure is reproduced from reference [312] with permission of The Electrochemical Society, Inc.)

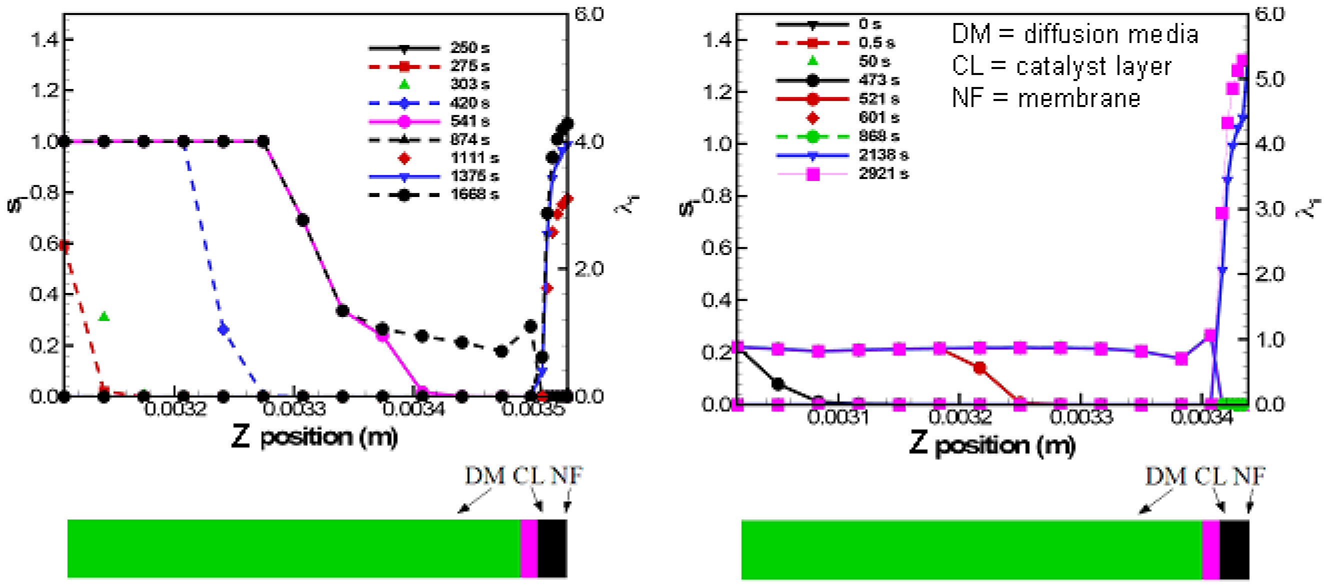

(a) (b)

Figure 29. Transient distribution of ice saturation with bipolar plates (a) or open channel (b) boundary conditions. (The figure is reproduced from reference [321] with permission of The Electrochemical Society, Inc.)

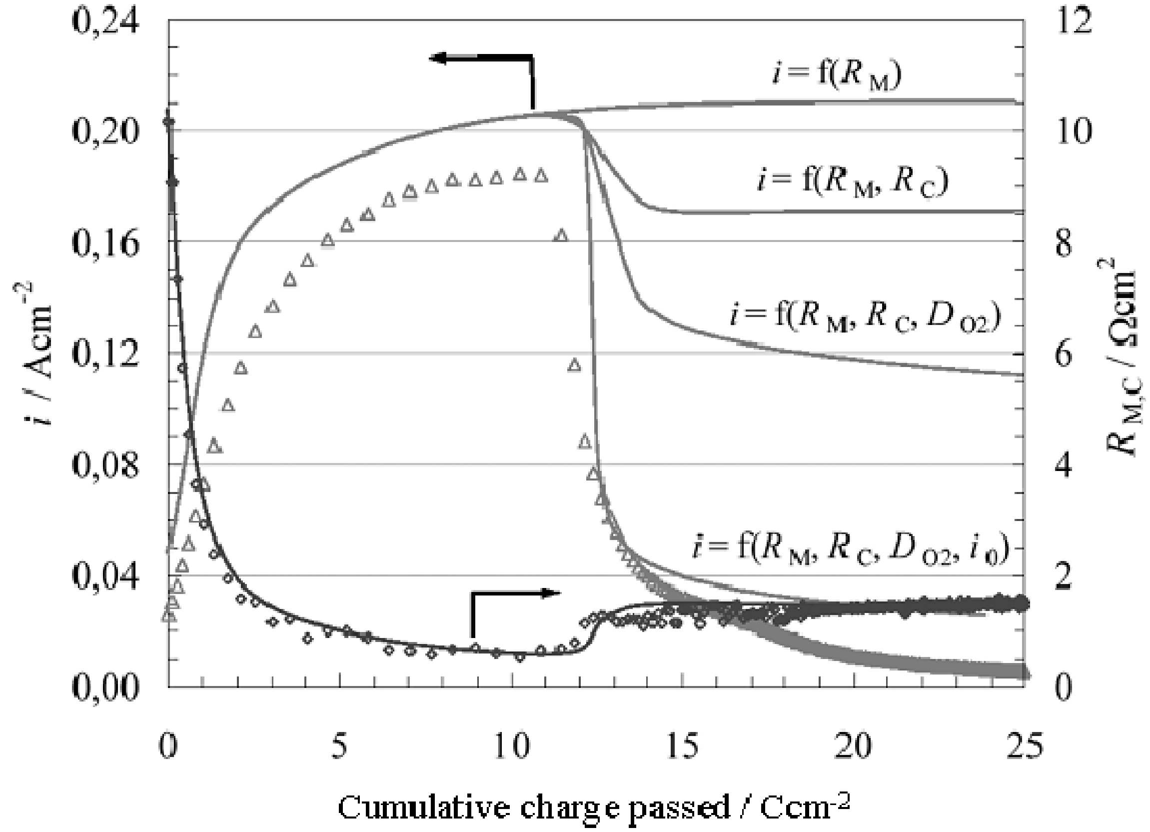

Figure 30. Comparison of simulation and experimental results for current density and ohmic membrane/contact resistance during cold sweep at –8 °C. (The figure is reproduced from reference [327] with permission of Wiley-VCH)

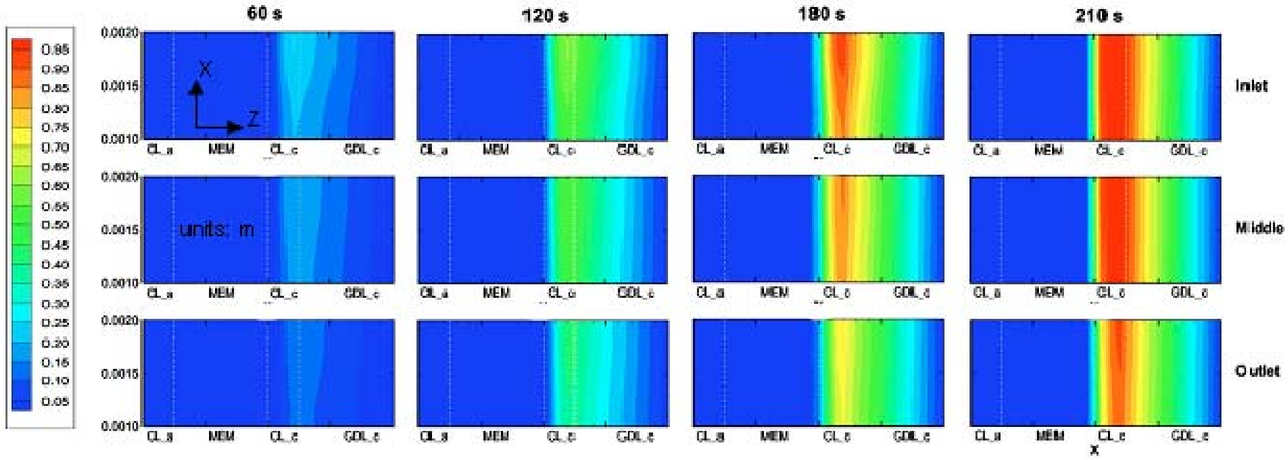

Figure 31. Ice-saturation evolution in the cathode CL. (The figure is reproduced from reference [329] with permission of The Electrochemical Society, Inc.)

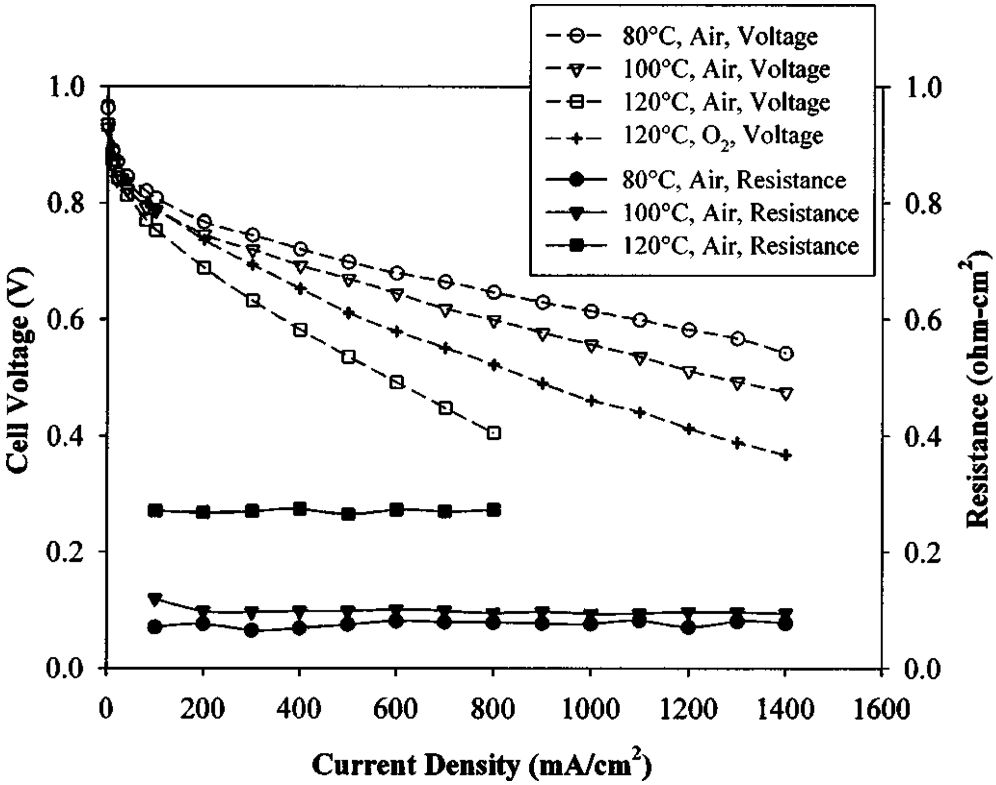

Figure 32. Polarization and resistance curves at various operating temperatures with a fixed water-vapor feed of 100 % saturation at 80°C with a Nafion® 112 membrane. The curves therefore correspond to inlet RHs of 100, 70, and 35 %, respectively. (The figure is reproduced from reference [346] with permission of The Electrochemical Society, Inc.)